SPECTROSCOPIC EXAMINATION OF HOST-GUEST INTERACTIONS IN METALLOPORPHYRIN-BASED METAL-ORGANIC FRAMEWORKS

By

Nicole-Irene Olivia Lahanas

A dissertation submitted to the
Graduate School-Newark
Rutgers, the State University of New Jersey
In partial fulfillment of the requirements
For the degree of
Doctor of Philosophy
Graduate Program in Chemistry
Written under the direction of
Professor Jenny Lockard
And approved by

_____

_____

_____

_____

Newark, New Jersey
October, 2019

ABSTRACT OF THE DISSERTATION

SPECTROSCOPIC EXAINATION OF HOST-GUEST INTERACTIONS IN METALLOPORPHYRIN-BASED METAL-ORGANIC FRAMEWORKS

By NICOLE-IRENE OLIVIA LAHANAS

Dissertation Director:

Dr. Jenny Lockard

At the center of heme-based protein systems, the metalloporphyrin has been extensively studied to yield better understanding of biological systems and their ability to reversibly bind small molecules. When metalloporphyrin units are strategically used as linkers in MOF materials, their associated functionality can be harnessed for potential catalytic processes occurring within the pores of these solid-state networks. The MOF format affords high densities of accessible metal reaction sites while preventing porphyrin dimerization and other undesirable deactivation processes that would normally occur in solution environments, thus promoting a new generation of heterogenous catalytic materials. Despite significant literature precedent for metalloporphyrin-based MOF catalysis, the underlying host-guest chemistry and catalytic reaction mechanisms are often unclear. Thus, a comprehensive understanding of how these frameworks interact with various guest molecules on a molecular level is crucial. Conventional characterization methods of crystalline solid-state materials such as single crystal XRD are helpful for examining local structure but have their limitations. Therefore, in this dissertation, more structurally sensitive characterization methods such as Raman, X-ray

absorption, and X-ray emission spectroscopy techniques are utilized in addition to conventional methods like XRD to obtain electronic and structural information of the host-guest interaction on a molecular level. A brief summary of each chapter is provided below.

Chapter 1 introduces relevant background information for the research topics in this thesis. The overview starts with a general introduction of host-guest systems, followed by an introduction to metal-organic frameworks, porphyrins, and finally porphyrin-based metal-organic frameworks. Lastly, the chapter concludes with a summary of the spectroscopic techniques employed in this research, namely Raman, X-ray absorption and X-ray emission spectroscopy.

Chapter 2 focuses on two isostructural metal-organic frameworks based on cobalt(II) and nickel(II) metalloporphyrin linkers, Co-PCN222 and Ni-PCN222, which are investigated using resonance Raman and X-ray absorption spectroscopy. The spectroscopic consequences of framework formation and host–guest interaction with weakly and strongly coordinating guest molecules (acetone and pyridine) are assessed. Structure sensitive vibrational modes of the resonance Raman spectra provide insights on the electronic and structural changes of the porphyrin linkers upon framework formation. XANES and EXAFS measurements reveal axial binding behavior of the metalloporphyrin units in Co-PCN222, but almost no axial interaction with guest molecules at the Ni porphyrin sites in Ni-PCN222.

Chapter 3 discusses how probing small-molecule interactions at the metalloporphyrin sites within MOF materials on a molecular level under ambient

conditions is crucial for both understanding and ultimately harnessing this functionality for potential catalytic purposes. Co-PCN-222, a metal−organic framework based on cobalt(II) porphyrin linkers, is investigated using in-situ UV−vis diffuse reflectance and X-ray absorption spectroscopy. Spectroscopic evidence for the axial interaction of diatomic oxygen with the framework's open metalloporphyrin sites at room temperature is presented and discussed.

Chapter 4 is a systematic comparison of host−guest interactions in two iron porphyrin-based metal−organic frameworks, FeCl-PCN222 and FeCl-PCN224, with drastically different pore sizes and geometries. Guest molecules (acetone, imidazole, and piperidine) of different sizes, axial binding strengths, and reactivity with the iron porphyrin centers are employed to demonstrate the range of possible interactions that occur at the porphyrin sites inside the pores of the MOF. Binding patterns of these guest species under the constraints of the pore geometries in the two frameworks are established using multiple spectroscopy methods, including UV−vis diffuse reflectance, Raman, X-ray absorption, and X-ray emission spectroscopy. Line shape analysis applied to the latter method provides quantitative information on axial ligation through its spin state sensitivity. The observed coordination behaviors derived from the spectroscopic analyses of the two MOF systems are compared to those predicted using space-filling models and relevant iron porphyrin molecular analogues. While the space-filling models show the ideal axial coordination behavior associated with these systems, the spectroscopic results provide powerful insight into the actual binding interactions that occur in practice. Evidence for potential side reactions occurring within the pores that may be responsible for the observed deviation from model coordination behavior in one

of the MOF/guest molecule combinations is presented and discussed in the context of literature precedent.

Chapter 5 is primarily a crystallographic study. This study was necessary for the evaluation of the coordination environment of manganese-porphyrin MOFs under various guest environments. Studying the axial ligation behavior of metalloporphyrins with nitrogenous bases helps to better understand not only the biological function of heme-based protein systems, but also the catalytic properties of porphyrin-based reaction sites in other biomimetic synthetic support environments, like MOFs. Unlike iron porphyrin complexes, little is known about the axial ligation behavior of Mn porphyrins, particularly in the solid state with Mn in the +3 oxidation state. Here, the syntheses and crystal and molecular structures of three new high-spin manganese (III) porphyrin complexes with the different amine-based axial ligands imidazole (im), piperidine (pip), and 1,4 diazabicyclo[2.2.2]octane(DABCO) is presented. These results, in conjunction with on-going TD-DFT calculations, will be used to explain the coordination of Mn-MOF materials with various guest molecules. XANES data suggests significant deviation from their analogous reference complexes.

Chapter 6 details the current status of research studying the liquid phase diffusion of guest molecules imidazole (Im) and 1-methylimidazole (MeIm) into the iron porphyrin-based MOFs, FeCl-PCN-222 and FeCl-PCN-224. MOF suspensions of varying particle size are measured to evaluate the impact of their porous structures on this process. Taking advantage of its element specificity and bulk penetration properties, in-situ hard X-ray absorption spectroscopy is used to assess the degree of Fe-imidazole (or Fe-MeIm) coordination in real time. Qualitative evaluation of these results shows

surprisingly fast diffusion kinetics in these materials, which have interesting implications for their use as catalysts. The future direction of this project will be discussed with an emphasis on extracting quantitative diffusion rates from XANES data.

Dedicated to my family

For your endless and unwavering support, guidance, and love

ACKNOWLEDGEMENT

First and foremost, I would like to extend my deepest gratitude to my advisor, Dr. Lockard, for her tremendous guidance and support. The five years I've spent in her research group are among my most memorable. I've learnt many lessons through this time, educational ones not least among them, but also ones of persistence, determination, mental strength, and perseverance; it is these I will cherish for a lifetime and for which I am deeply thankful for.

I would like to thank the members of my committee, Dr. Piotrowiak, Dr. Mendelsohn, and Dr. Li for their guidance and support during my study.

I would like to thank my collaborator, Dr. Lalancette for his expertise and guidance, without which chapter 5 of my thesis would not have been done.

I would like to thank all the Chemistry Department faculty members, all of which have provided me with endless help and guidance.

I would like to especially thank Dr. Pavel Kucheryavy who was a tremendous mentor to me. I am profoundly thankful for being able to work so closely with you and learn from you. I would not be here without your guidance and your genuine kindness.

I would like to thank my dear friend and groupmate, Lauren Hanna, for her endless support, laughs, cries, and challenges. I am a better person and student because of our friendship, and I will always treasure it. I could not have done this without you.

I would like to thank my fellow doctoral students and post-doctorals, most of whom helped me along the way and provided me with a sense of community while at Rutgers.

I would like to thank all the staff members who made every effort to help me through the years and made this journey a smooth one.

Chapter 2 of this dissertation is a version of the manuscript as it appears in *Journal of Coordination Chemistry*, 2016, **69**, 1780.

Chapter 3 of this dissertation is a version of the manuscript as it appears in *Inorganic Chemistry*, 2016, **55**, 10110.

Chapter 4 of this dissertation is a version of the manuscript as it appears in *Inorganic Chemistry*, 2018, **57**, 3339.

Chapter 5 of this dissertation is a modified version of the manuscript as it appears in *Acta Cryst. C,* 2019, **75**, 304.

TABLE OF CONTENTS

LIST OF ABBREVIATIONS

DABCO	1,4-diazabicyclo[2.2.2]octane
DR	Diffuse Reflectance
EXAFS	Extended X-ray Absorption Fine Strcuture
HS	High Spin
IADs	Integrated Area of the Absolute Difference Spectra
Im	Imidazole
LS	Low Spin
MOF	Metal-Organic Framework
MS	Mixed-Spin
PCN	Porous Coordination Network
Pip	Piperidine
Py	Pyridine
SBU	Secondary Building Units
TCPP	Tetracarboxyphenylporphyrin
TPP	Tetraphenylporphyrin
TGA	Thermal Gravimetric Analysis
UV-vis	Ultraviolet-visible
XAS	X-ray Absorption Spectroscopy
XANES	X-ray Absorption Near Edge Structure
XES	X-ray Emission Spectroscopy
XRD	X-ray Diffraction

LIST OF TABLES

LIST OF FIGURES

LIST OF SCHEMES

Chapter 1: Introduction

One of the major driving-forces in chemistry, material science and engineering, is the host-guest relationship in porous materials (i.e zeolites, biological tissues, ceramics, etc) and supramolecular structures. These interactions dictate their functionality for applications in molecular separation and storage, among others. A "host" is characterized as a larger molecule with a measurable cavity or molecular framework with permanent porosity. A smaller "guest" molecule or ion interacts with the host and produces a more complex system. The interactions between host and guest can range in strength from weak hydrogen bonding, to van-der-Waals forces and π-π interactions, to strong coordination bonds. The sum of these interactions forges a complicated system which makes them interesting for spectroscopic study.

One class of materials for which host-guest interactions play an important role in their functionality is metal-organic frameworks. The properties of these materials are governed not only by the underlying crystalline structure but the interaction of the framework components with guest species contained within their pores. Therefore, for intelligent design of new MOF materials intended for a desired application, it is necessary to understand not only their initial structure, but their interaction with guest species on the molecular level as well. Common techniques of characterization such as X-ray diffraction or thermal gravimetric analysis (TGA) can help to elucidate long-range order or bulk structure information, however they do not provide comprehensive details about the host-guest interaction. This thesis emphasizes the use of vibrational and X-ray

spectroscopy techniques, along with traditional characterization methods, to provide a more complete assessment of the host-guest interactions in some MOF systems.

The focus of this dissertation is investigating host-guest interactions in porphyrin-based metal-organic frameworks (MOFs) by spectroscopy methods. Basic concepts and properties of MOFs and more specifically porphyrin-based MOFs will be introduced below, followed by a brief introduction to the various spectroscopy methods employed throughout the research. In the remaining chapters five different porphyrin MOF-related projects will be covered detailing how these spectroscopy methods allowed us to track changes associated with a range of incorporated guest molecules from gases (Chapter 3) to weakly-interacting ligands (Chapter 2) to strongly coordinating species (Chapter 4-6).

1.1 Metal-Organic Frameworks

Metal-Organic Frameworks (MOFs) (sometimes referred to in literature as porous coordination polymers) are porous, self-assembled, 3D-solid state networks composed of metal ions/clusters (SBU; node) and organic/organometallic linker groups shown in Figure 1.1. The resulting highly stable crystalline architectures have permanent microporosity and controlled functionality, with an abundance of possible reaction centers. These attributes make MOFs desirable for applications in clean energy such as for small molecule/gas separation and storage,[60-64] delivery, as well as catalysis[65-67] and sensors.[68,69] This thesis will focus on the spectroscopic studies of host-guest interactions in Metal-Organic Framework materials.

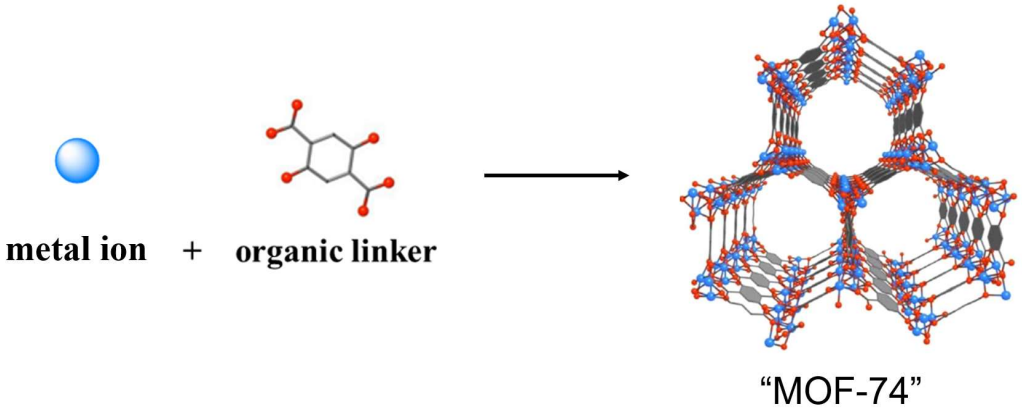

Figure 1.1 Illustration of a metal-organic framework and its components.[1]

The first example of a highly porous and robust MOF was reported by Yaghi and co-workers in 1999 called "MOF-5."[2] This framework is crafted by joining $Zn_4O(CO_2)_6$ octahedral nodes with six 1,4-benzenedicarboxylate linker units yielding a cubic MOF shown in Figure 1.2.

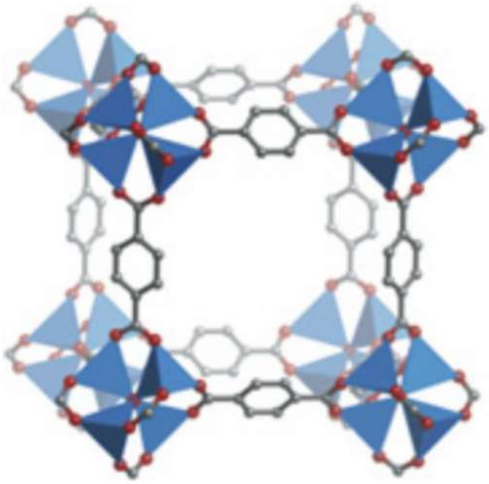

Figure 1.2 MOF-5 framework. Zn4(O) subunits are represented as blue tetrahedron. Zn(blue), oxygen (red), carbon (grey).

Gas sorption measurements yielded an approximate 61% porosity and a BET surface area of 2320 m^2/g. What was exceptional about this first MOF is that these porosity and BET parameters were much larger than those reported for other porous materials such as zeolites[3], activated carbon[4], and MOPs (metal-organic polyhedra)[5].

In order to prepare MOFs with even higher porosity and thus extend the storage space in a given material, longer organic linkers were incorporated. In 2004, Yaghi and co-workers successfully made MOF-177[6], which boasted a surface area of 3780 m^2/g and a porosity of 83%. Continuing in their work, Yaghi and co-workers synthesized MOF-200[7,8] and MOF-210[8] in 2010, which doubled the surface area and provided porosities of 90% and 89%, respectively.

By isoreticular expansion, MOFs with the same underlying topology but different functionalized linkers afforded these materials the possibility for use in applications of gas storage[9-11] and separations[12-16]. This new set of frameworks showcased the degree of tunability, both structurally and chemically, afforded by these materials. Because it was proven that MOFs can be designed to exhibit desired functionality by varying the metal clusters and organic linker groups with the desired attributes, they can be harnessed for their use in a myriad of applications across a broad range of scientific and technological arenas, with tens of thousands of different frameworks already reported in the last 20 years. For example, HKUST-1 (Basolite C 300) is commercially available and used for the separation of olefins.

Key structural features of the MOF determine their potential for various applications. These features, including pore size and shape, open metal sites and functional groups, not only govern the topology of the framework, but the host-guest interactions that can be

exploited within them. The role of pore size and shape in dictating what guest species can be stored or separated within the framework is undoubtedly one of the essential factors when considering potential MOF applications. This is especially important when considering adsorption and catalytic applications. The typical pore openings (≤ 2nm) are generally large enough for small molecule or ion encapsulation but restrict access for larger, bulky guest molecules. Separations of molecules can be achieved through small pore openings which allow smaller molecules to pass through but block diffusion of larger guest molecules.[7]

The high surface area attributed to MOFs allows for considerable packing of a range of small guest molecules, particularly gases such as H_2, N_2, CH_4, and CO_2. Increasing the surface area and pore volume decidedly enhances the gravimetric hydrogen and methane uptake making these materials prime candidates for storage and/or separation of these fuels for energy applications.[7]

The diversity of pore size and shape allows for the design of MOFs that elevate their ability to act as catalytic hosts over other competing solid-state porous materials. By integrating larger pores and varying pore-shape, the diffusion of incoming reagents or outgoing products in a catalytic cycle becomes much more facile.[17] Zeolites offer only limited cavity sizes and mesoporous silicates have the opposite problem in that they have too large void space making encapsulation problematic. Intentional design of MOF materials to yield specific structures that can then be functionally tuned and manipulated distinguishes these materials over others.

The reactivity of MOFs can be modified by tailoring the organic/inorganic linkers and by covalent/coordinatively functionalizing the SBU. This type of modification is

usually done post-synthetically as opposed to during framework formation. This allows for the precise control of the resulting functionalized framework. There are generally two types of postsynthetic modification of MOFs: covalent alteration of the nodes and through the coordination of ligands to coordinatively unsaturated metal centers on the SBU or inorganic linkers[18]. Both these post-synthetic modifications are applicable to the porphyrin-based MOFs on which this thesis is based.

The strong coordination bonds that hold MOFs together make them stable to reasonably high temperatures (250˚C-500˚C) and can provide high chemical stability[18]. The higher stability in these materials generally stems from their SBUs (polynuclear clusters) which provides an "anchor" in the MOF and creates enough rigidity to ensure the local geometry of the framework. This feature provides the robustness of the architecture needed for further application and/or modification and optimization. Framework stability is utilized to enhance their performance in CO_2 capture and other small molecule activation[7].

1.2 Porphyrins

Porphyrins are heterocyclic, macrocyclic compounds (Figure 1.3) that are comprised of four modified pyrrole units connected through methine bridges at their α-carbon atoms and contain 26 π-electrons, 18 of which makeup a planar, conjugated system. Metal ions coordinated within the porphyrin ring form metal complexes. These metallated structures are intimately linked to many biological systems and serve as active sites for many proteins. Furthermore, porphyrin peripheral sites are easily manipulated making

them functionally diverse. For these reasons, porphyrins serve as exciting building blocks for the design of new catalysts where the properties of porphyrins are exploited to create model systems with desired functionality. In the following sections I will discuss the evolution of porphyrins from their place in nature to their role as model systems for heterogeneous catalysts.

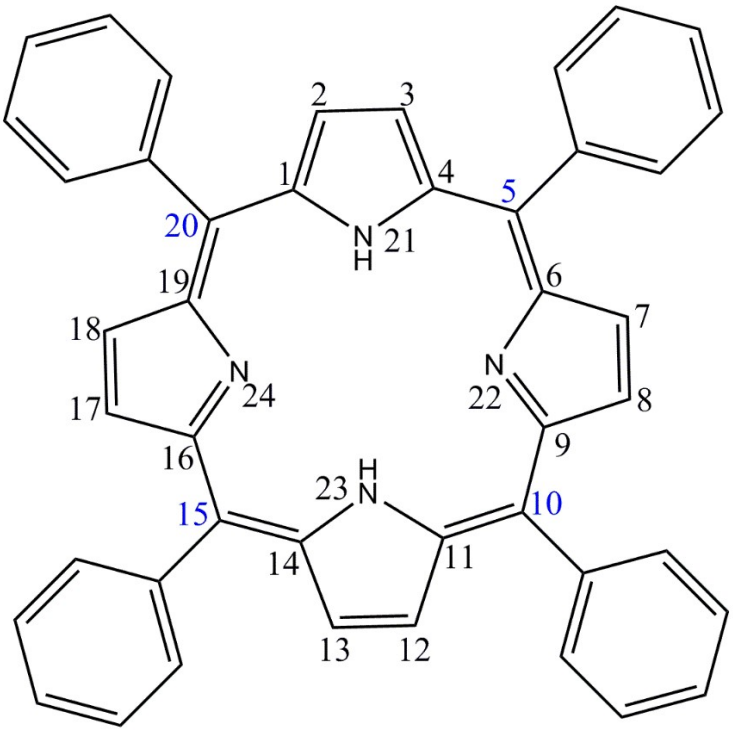

Figure 1.3 Illustration of a porphyrin with relevant numbering and nomenclature.[19]

1.2.1 Biological Relevance

Porphyrins and their derivatives serve as active sites for many proteins, whose functions of oxygen transfer and storage (ex: hemoglobin and myoglobin) to electron transfer (ex: cytochrome c) and energy conversion (ex: chlorophyll) make up the basis of all aspects of life. Through attempts to replicate natural porphyrins' functionality using synthetic systems, we hope to learn how they behave in nature. For example, both hemoglobin and myoglobin reversibly bind oxygen to a ferrous iron without causing autooxidation of the iron center. The mode of oxygen binding to ferrous iron and how irreversible oxidation does not occur has caused much speculation.[20] Furthermore, other ferrihemoproteins such as hydroperoxidase and peroxidase, are believed to involve an initial two-electron oxidation of ferrihemoprotein; a one electron oxidation of the iron to Fe (IV) and a one-electron oxidation of the porphyrin ring through removal of an electron from the π-electron cloud forming a porphyrin π-cation radical.[27] These examples illustrate the versatility of the porphyrin macrocycle which can stabilize unusual oxidation states of metals and additionally act as both an electron source and sink. These traits make porphyrins ideal for their implementation in catalysis.

1.2.2 Porphyrin Coordination Complexes in Solution

Naturally occurring porphyrins contain peripheral groups that are chemically reactive (i.e. vinyl groups) making them unstable outside their protein environments.

Synthetic porphyrins have been designed as model systems for natural systems to side-step this problem and gain better insight to their electronic structure which governs their biological function. One of the most actively studied application of synthetic porphyrins is in oxidative catalysis. The first report of the use of a synthetic metalloporphyrin for catalytic oxidation was by Groves et al. in 1979.[22] They used iodosylbenzene as an oxygen atom donor in olefin epoxidations and alkane hydroxylations catalyzed by iron tetraphenylporphyrin chloride (Fe(TPP)Cl). Their results showed that Fe(TPP)Cl serves as a suitable model for cytochrome P-450, in that the high-valent metal-oxo porphyrin complex displays oxygenase character when the alkane is present in excess. They were able to extend their results using other metal-TPP complexes as catalysts, such as manganese and chromium.[23-24] These metal derivatives of H_2TPP are known as "first generation metalloporphyrin catalysts" and they are useful for a few reasons: they can be used with a variety of oxidants, they are stable in a wide-range of reaction conditions, and they can be designed to be selective in both epoxide shape and symmetry. Despite these advantages, several catalytic deactivation pathways exist when porphyrins are in solution: aggregation, demetallation, metal ion exchange reactions, and ligation & electron transfer reactions. To overcome these obstacles the use of solid-state or supported porphyrin catalysts become interesting alternatives.

1.3 Porphyrin Solids

Because of the success metalloporphyrins have seen as homogeneous catalysts, chiefly in oxidative reactions, researchers wanted to extend their functionality to heterogeneous catalysis by implementing metalloporphyrins as molecular solids and

extended networks. The next few sections discuss how solid-state metalloporphyrins are useful for selective separations, chemical sensing, and catalysis and introduces the concept of porphyrin-based MOFs.

1.3.1 Non-Porous to Microporous Porphyrin Solids

One of the earliest attempts to obtain truly porous solid-state metalloporphyrins were the picket-fence porphyrins, shown in Figure 1.4, which are held together by weak van-der-Waals forces[25-27]. Interestingly, these porphyrins showed reversible O_2-binding in the solid-state. However, due to the nature of the forces that hold these solids together, their stability after solvent removal is problematic. Suslick et al. synthesized and studied more robust frameworks linking porphyrin molecules held together through multiple hydrogen-bond interactions[28]. Hydrogen-bond interactions provided the advantage of having directionality and selectivity incorporated to the framework, key features in controlled catalysis. One such porphyrin solid is based on symmetrically substituted octahydroxyporphyrins, shown in Figure 1.5, which can be easily controlled due to the 3D nature of the hydroxyl groups on both faces of the porphyrin. Greater stability was achieved through the eight hydrogen bonds created per porphyrin, generating a layered motif where the porphyrins were arranged in a "slipped stack" orientation of flat porphyrin planes held together through hydrogen bonds creating inter-planar separations of 6.81Å and an adjacent layer which is offset by a vertical distance of 4.98Å from the plane of the porphyrin. Although promising, these porphyrin solids still have limited stability without their solvates, and upon vacuum-assisted removal of solvates, the porous solid collapses, leaving rendering the material non-porous. With networks held together

with both wan-der-Waals and hydrogen bonding not strong enough to withstand solvent evacuation, researchers looked to synthesize more robust frameworks held together through coordination bonding.

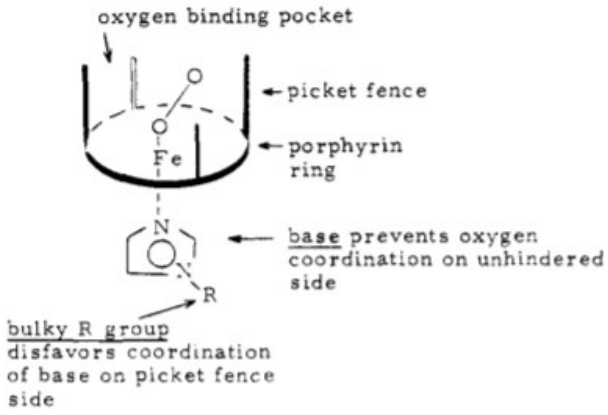

Figure 1.4 Illustration of a picket-fence porphyrin.[25]

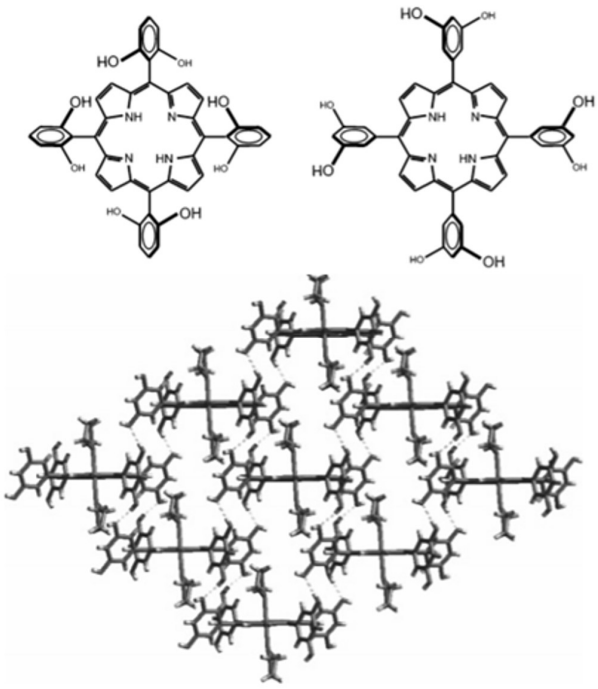

Figure 1.5 Symmetrically substituted octahydroxyporphyrins (top), Hydrogen-bonding between the planes of the network depicted by dashed lines (bottom)[28]

1.3.2 Porphyrin-based MOFs

The first porphyrin-based MOF structure was reported by Suslick et al. who solvothermally synthesized 3D framework PIZA-1 (Porphyrinic Illinois zeolite analogue-1), shown in Figure 1.6. This framework contains ruffled cobalt(III) tetra(p-carboxyphenyl)porphyrin (TpCPP) linkers coordinated to linear trinuclear cobalt (II) clusters[28]. They found porosity to be thermally robust through the use of XRD, TGA, and nitrogen sorption studies. Furthermore, PIZA-1 displays desiccant properties, with selective sorption of water. In fact, when compared to zeolite 4A (molecular sieves), PIZA-1 shows a greater affinity, higher capacity, and faster response for selective water sorption. In addition to selective sorption patterns, PIZA-1 demonstrates shape and size selectivity of guest species, preferring hydrophilic, polar, and short-chained guests. Taking their studies a step further, PIZA-2 (cobalt(III) tetra(p-carboxyphenyl)porphyrin) and PIZA-3 (manganese(III) tetra(p-carboxyphenyl)porphyrin) coordinated to a bent trinuclear cobalt cluster were synthesized[28]. Both frameworks showed a strong preference for small, hydrophilic guests with the added addition of PIZA-3 having the added ability to catalyze hydroxylation and epoxidation reactions at a similar rate as other homogeneous systems. Together, these attributes form a promising platform for similar porphyrin-based frameworks.

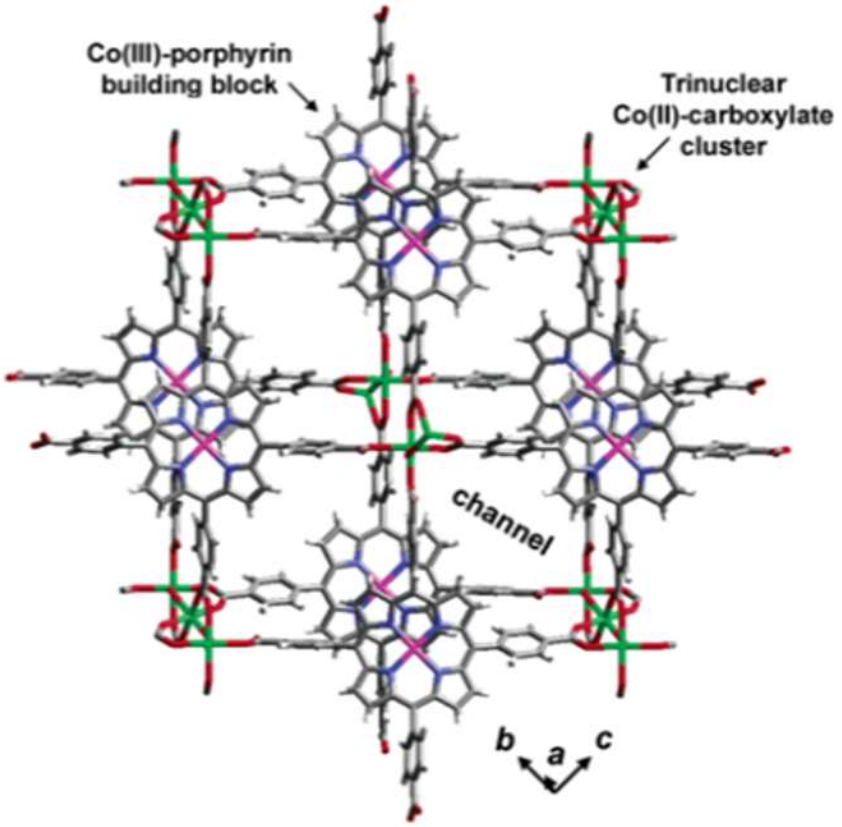

Figure 1.6 PIZA-1 Framework[28]

In 2012, Farha & Hupp published a report of an active-site-accessible porphyrinic MOF containing a tetracarboxylated porphyrin ligand pillars (L^1) combined with bulky dipyridyl porphyrin struts (L^2) to paddlewheel-coordinated zinc nodes[29]. The bulky L^2 ligand prevents pillar coordination at the metalloporphyrin sites, leaving coordination accessible only to the more favorable paddlewheel sites. The metals associated with L^1 and L^2 can be varied, with L^1 having M^1= 2H, Pd, Al(OH) or Fe(Cl) and L^2 having M^2= 2H or Mn(Cl), forming materials with a final designation of M^1M^2-RPMs (RPM=robust porphyrinic materials), shown below in Figure 1.7.

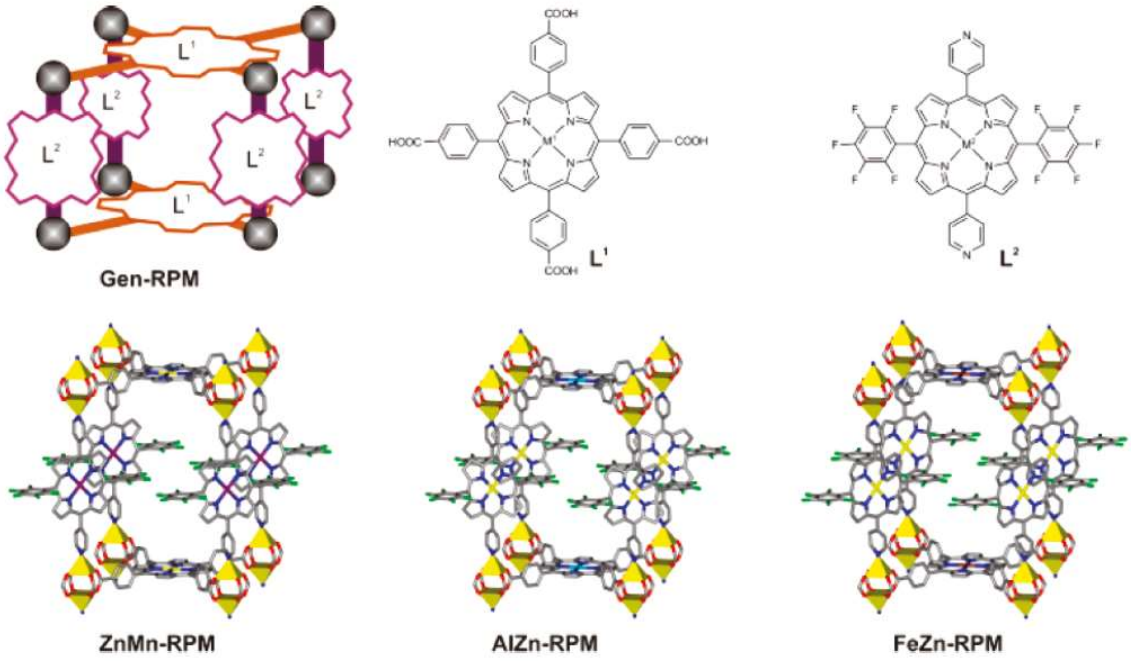

Figure 1.7 RMP Structure and porphyrin building blocks (top), and three representative RPMs (yellow polyhedra = Zn, yellow = Zn, brown = Fe, purple = Mn, teal = Al, red = O, green = F, blue = N, gray = C).[29]

The authors concluded that a variety of metalloporphyrins can be incorporated into MOFs, while retaining their catalytically active open metal-coordination sites. For example, the Mn-porphyrin RPM was successfully used for alkene epoxidation and alkane hydroxylation reactions, albeit with limited selectivity.

Another series of 3D coordination polymers named MIL-141(A), A = Li, Na, K, Rb, Cs (Figure 1.8) were solvothermally synthesized using iron (III) and nickel (III) tetracarboxylate porphyrin (NiTCPP) and contained the aforementioned alkali metals within the pores[30]. These MOFs are extremely stable upon solvent removal, and framework flexibility is dependent on which alkali metals are present in the pores (an

increase in cation size also increases framework rigidity). Of the three cationic species present in the MOF (the node [Fe^{3+}], the porphyrin central metal [Ni^{2+}], and the extra framework entrapped cation [A^{+}]) two may act as coordinatively unsaturated metal sites (Ni^{2+} and A^{+}). Furthermore, unlike their cation-containing zeolite analogues, which prefer N_2 adsorption, this MOF series showed an increase in O_2 preferential adsorption.

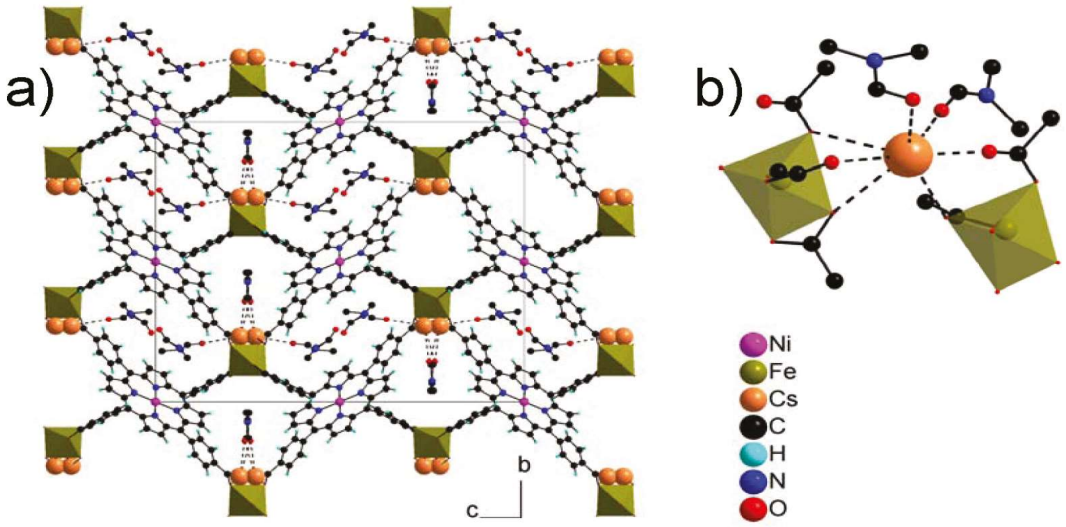

Figure 1.8 MIL-141A Framework[30]

These examples of porphyrin-based MOFs display elevated opportunity for the wide range of porphyrins that can be implemented for the purpose of harnessing their catalytic properties, and more specifically, in their ability to perform selective chemical separations. In the next section, a series of porphyrin-based MOFs with ultra-stable zirconium nodes will be introduced. These porphyrin-based frameworks will be the MOFs in which this thesis focuses on.

Realizing the need for MOFs with larger pores that can accommodate large substrate molecules, Zhou and coworkers set out to synthesize a MOF that had

mesopores, accessible redox sites, and ultrahigh stability was compatible to an aqueous environment. The authors utilized the porphyrin M-TCPP (M=Fe, Co, Ni, Zn, Mn) as a linker to highly stable Zr-oxo cluster nodes, forming a series of ultra-stable 3D heme-like zirconium MOFs: PCN-221(M), PCN-222(M), PCN-223(M), PCN-224(M) and PCN-225(M) (PCN=porous coordination network).[31-35] Concurrently, the Ma and Yaghi groups each synthesized the same overall framework as PCN-222(M), designating it as MMPF-6[36] and MOF 545[37], respectively. The Yaghi group also simultaneously synthesized an equivalent PCN-221(M) MOF structure, naming it MOF-525.[37] These frameworks have demonstrated the ability to catalyze various oxidation reactions, specifically peroxidase reactions, while having high substrate binding affinity and catalytic activity in aqueous media. This thesis will focus primarily on frameworks PCN-222(M) and PCN-224(M) and their interactions with various guest molecules. These results will be discussed further in chapters 2-6, however, Figure 1.9 details the synthetic steps necessary in obtaining the final guest-soaked frameworks. After the MOFs have been synthesized according to literature procedures,[31,33] they are soaked in acetone to remove any DEF/DMF and salts left behind. Thermal activation is then required to remove any unbound or weakly bound solvents from the MOF. Lastly, the desired guest species is introduced to the activated framework.

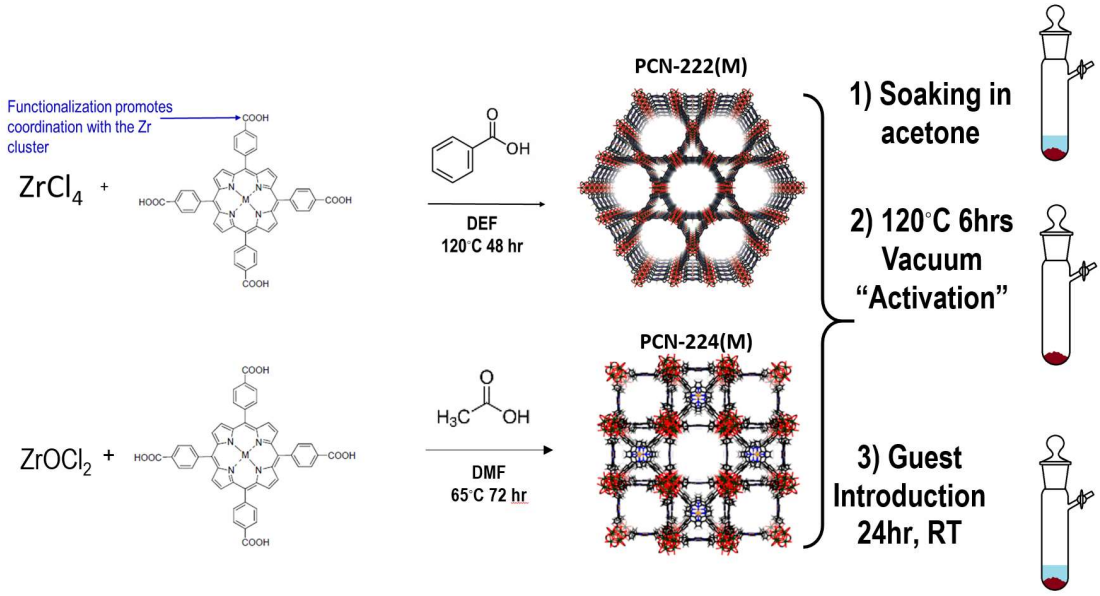

Figure 1.9 Synthetic steps to achieve final guest-soaked PCN-222(M)[31] and PCN-224(M).[33]

As mentioned above, PCN-222(M) (Figure 1.10 left) was designed by utilizing square planar M-TCPP as a heme-like linker and Zr_6 cluster nodes resulting in the 3D heme-like MOF, parenting two different pore sizes, large hexagonal 3.7nm 1D open channels and 1.3nm trigonal pores. In 2012, both Zhou and Yaghi published the crystal structure for PCN-222(M) and MOF-545(M), respectively. Single-crystal x-ray diffraction revealed that each $Zr_6(OH)_8$ cluster core is connected to eight TCPP ligands and capped with μ_3-OH groups at the triangular faces of the Zr_6-octrahedron producing D_{4h} symmetry. The ultra-high stability of this framework is attributed to the Zr_6 cluster, which remains intact even after treatment with concentrated HCl[31]. The heme-like properties of this framework make it an attractive candidate for enzyme-mimic. To this end, the authors proved that an activated sample of PCN-222(Fe) showed elevated peroxidase-like catalytic activity when compared to other catalysts under the same

conditions.[31] Isostructural MOFs with uncoordinated porphyrin and other metalloporphyrins such as Mn, Co, Ni, Cu, and Zn have been generated as well,[31] and this thesis will discuss a few of them in the context of their ability to interact with specific guest species which are monitored through spectroscopy. Like PCN-222(M), PCN-224(M) (Figure 1.10 right) was designed by joining square planar TCPP ligands and Zr_6 clusters. In this framework however, only six edges of the Zr_6 octahedron are bridged by carboxylates from the TCPP ligand, reducing the overall symmetry to D_{3d}. The remaining positions at the top and bottom of the Zr_6 octahedron are occupied by terminal hydroxy groups. The PCN-224(M)[33] MOF has 3D 19Å channels and elevated chemical stability, which is attributed its elevated performance as a heterogeneous catalyst.

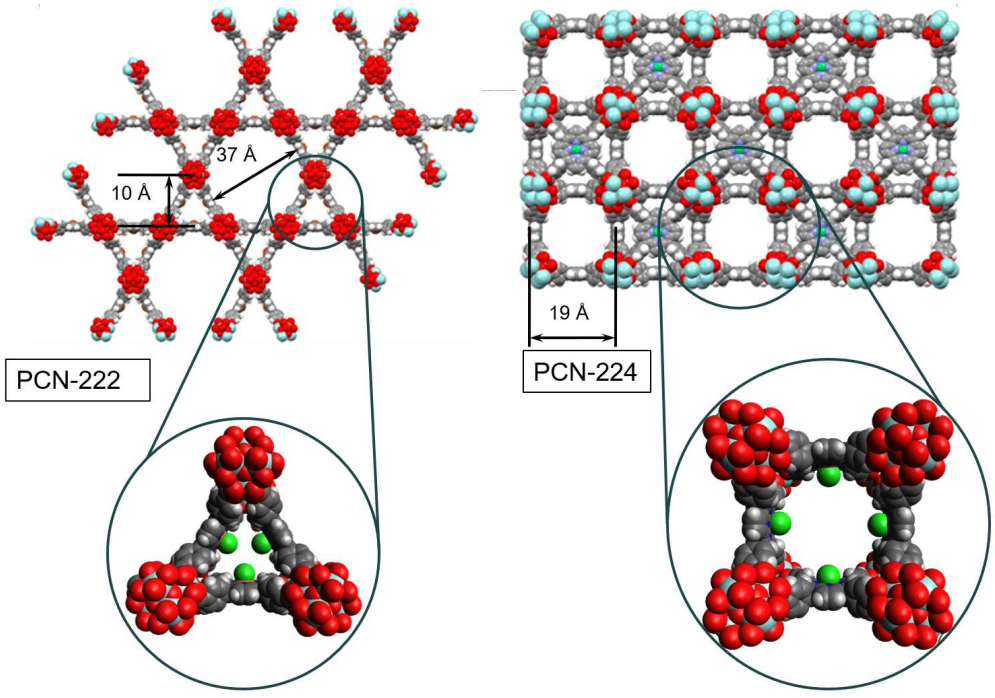

Figure 1.10 Illustration of PCN-222 and PCN-224.

1.4 MOF Characterization: Conventional Techniques

Conventional methods of MOF characterization probe bulk properties such as long-range order, surface area, and pore size. Single crystal XRD (SXRD) is the most informative way of procuring structural information on MOFs. This is done through structure refinement of the diffraction data which provides information such as crystallization space group, connectivity, void space, and symmetry. It can also be utilized to determine framework activation (elimination of solvent molecules) and extent of gas adsorption.[38-40] Unfortunately, SXRD is not always possible due to the difficulty in preparing single crystals of good enough quality to diffract. This is especially true after treatments such as thermal activation or guest treatment, which can easily affect the single crystals long-range order. An alternative to SXRD is powder XRD (PXRD) which provides likewise valuable information of a framework's structural features, only indirectly through crystal lattice parameters.

Thermogravimetric analysis can be utilized to measure framework stability and openness by measuring the weight loss between the temperatures of guest desorption and framework decomposition. Following gravimetric analysis to ensure porosity, using evacuated MOF samples, gas-uptake (H_2, CO_2, CH_4) can be measured to determine accessible open-space. Gas-sorption isotherms can then be used to calculate the pore volume and surface area of the evacuated framework.[41]

These characterization methods are useful in determining framework stability however they do not provide the local electronic structure information needed to evaluate host-guest interaction. The next section in this chapter describes a multi-faceted spectroscopy approach that will reveal these host-guest interactions on a molecular level.

1.5 Electronically and Structurally Sensitive Spectroscopy Techniques

Traditional means of solid-state characterization such as XRD, provides structural information on long-range order but does not provide local structure information on specific binding sites or regions of guest interaction. Conventional FTIR, which can provide structural information but has many experimental limitations, such as heavily congested spectra with severely overlapped, poorly resolved peaks making subtle changes associated with guest interaction difficult to identify. Solid-state NMR can be useful for obtaining molecular level insights for some MOF materials[42-43] however this technique is limited because certain nuclei are incompatible, particularly for some metalloporphyrin-based MOFs. Other spectroscopy methods, such as resonance Raman spectroscopy, X-ray absorption spectroscopy, and X-ray emission spectroscopy are used in this thesis work to probe the structural and electronic changes of host-guest interactions of the porphyrin-based MOF systems on a molecular level.

1.5.1 Raman Spectroscopy

Raman spectroscopy is a method used to measure the vibrational modes of a given material. Complimentary to IR spectroscopy, which directly probes the energy difference between vibrational energy levels through the absorption of light with the same energy, Raman spectroscopy indirectly provides this energy difference by measuring the inelastically scattered (Raman scattered) monochromatic laser light typically with energy much higher than those of the vibrational transitions. IR and Raman spectroscopy are complimentary techniques; where Raman is typically more

sensitive to symmetric vibrational modes and IR is more sensitive to asymmetric modes as a result of the different selection rules associated with each process. Vibrational modes are IR active when a change in dipole moment is involved, whereas Raman activity follows when the mode results in a change in polarizability. The laser light interacts with the molecular vibrations in the system, resulting in the energy of the laser photons (incident photons) being shifted. These energy shifts are a consequence of the laser light interacting with molecules with polarizability α, resulting in an induced electric dipole moment P=αE which is caused by the distortion of the molecules when interacting with the laser light. The intensity of the Raman scattering is proportional to the polarizability change of the electrons in the molecule. If the energy difference between the incident photons and the scattered photons lose energy, it is known as a "Stokes shift." An "anti-Stokes shift" therefore implies a gain in energy of the scattered photons. These details are illustrated in Figure 1.11. The frequency of a vibration, ν, which is expressed in equation (1) is equal to:

$$\frac{1}{2\pi}\sqrt{\frac{k}{\mu}} \tag{1}$$

where k is the force constant and μ is the reduced mass. Because of this relationship, structural changes can be extrapolated. With higher force constants signifying stronger bonds, changes in bond strength are revealed through frequency shifts in a vibrational mode. Therefore, Raman spectroscopy can be used to ascertain host-guest interactions on a more localized structural level by tracking changes associated with both the host and guest through frequency shifts in the vibrational spectra.

Furthermore, using resonance Raman (RR), the intensity of specific modes can be enhanced. RR describes the measurement when the laser excitation frequency coincides with the energy of electronic excitation in a molecule or material leading to an observed enhancement of vibrational mode intensities and in effect simplifies the observed Raman spectrum. This thesis employs RR to enhance specific ligand-based (i.e. porphyrin) vibrational modes in the studied MOFs.

Raman spectroscopy can establish the presence and interaction of guest species with the host framework by tracking changes associated with the metal-porphyrin units which serve as the linkers in the MOFs of study. Characteristic mode frequencies of the porphyrin ring system with different metal centers help identify the interacting species and the frequency shifts of these peaks reveal changes in bond strength and polarization. There are several important skeletal porphyrin modes that are sensitive to the metal ion size and, therefore, the oxidation and spin state of the metal center. For example the core breathing mode, ν_8, which occurs in the range of 380 cm^{-1} and is known as an oxidation state marker mode in metalloporphyrin systems.[45] ν_4, another porphyrin marker mode assigned to a pyrrole deformation mode,[44,46] which is sensitive to metal oxidation and spin state even within the MOF environment, and porphyrin core C-C stretching modes, ν_2 and ν_{20}, which are spin state sensitive even in MOF environments. Table 1.1 lists the structurally relevant porphyrin-based modes and their assignments using the numbering scheme established by Kitagwa *et al.*.[47] Additionally, utilizing incident laser excitation that is in resonance with any porphyrin-localized electronic transitions, we will have enhancement of these porphyrin-based modes in the Raman spectrum. Thus, Raman and RR are widely used methods when probing the interaction of guest molecules with host

materials such as the PCN series. Additionally, changes in framework-based vibrational modes due to the various manipulations (i.e thermal activation, guest introduction) can demonstrate how the MOF themselves are transformed in the process. Although at times these changes are subtle, particularly when examining the MOF-related vibrational modes, Raman spectroscopy reveals powerful information on the interaction between the host and guest and provides further validation for our various other spectroscopy methods.

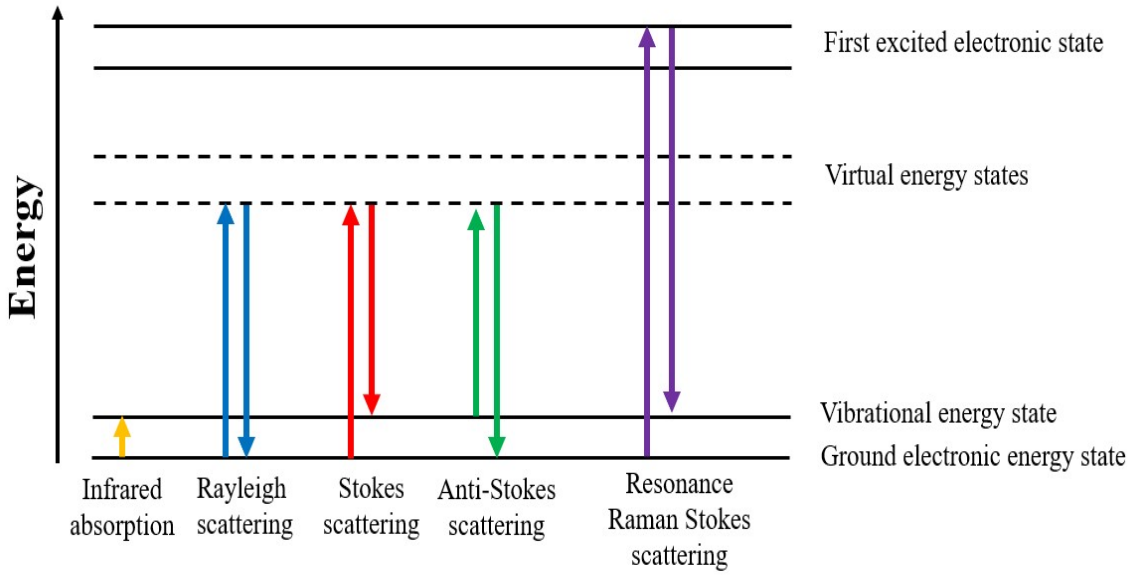

Figure 1.11 Illustration of Raman scattering

Table 1.1 Structure sensitive Raman modes and assignments[a]

ν_2	ν (C_β-C_β) + ν_{sym}(C_α-C_m) + δ_{sym}(C_β-H)
ν_{19}	ν_{asym}(C_α-C_m) + ν_{asym}(C_α-C_β)+δ_{asym}(C_β-H)
ν_{11}	δ (C-C-H) + ν_{asym}(C-C) + ν_{sym}(C_α-C_m)
ν_3	ν_{sym}(C_α-C_m) + ν(C_β-C_β)
ν_4	ν_{asym}(Pyr. Half ring)
ν_{20}	ν(Pyr. Quarter ring)+ δ_{sym}(C_β-H) + δ (C-C-H)+ ν_2 (C-C)
ν_{27}	ν_{sym}(Pyr. Halfring) + ν(C_m-Ph) + ν_1(C-C)
ν_1	ν(Pyr. Breathing) + ν(C_m-Ph)
ν_9	δ_{sym}(C_β-H)
φ_8	δ (C-C-C)+ν_{asym}(Pyr. Breathing)
φ_8'	δ (C-C-C)+ν_{asym}(Pyr. Half ring)
ν_8	$\nu_{breathing}$(M-N)

[a]Numbering scheme and assignment follows that of normal coordinate analysis reported[47]

1.5.2 UV-visible Diffuse Reflectance

Diffuse reflectance (DR) methods are employed to measure ground state absorption spectra of MOF systems. In relation to optical transmission methods, where the transmittance, or ratio of intensities of transmitted to incident light, is measured, DR involves the measurement of remittance, R_∞, or the ratio of reflected to incident light. (the ∞ subscript here denotes effectively "infinite" sample thickness.) Plotting $\log(1/R_\infty)$ versus incident photon energy yields "apparent" absorption spectra. Like Beer's law in transmission spectroscopy, the Kubelka-Munk function linearly relates concentration with the reflectance values of a diffusely reflecting sample:

$$F(R_\infty) = \frac{(1-R_\infty)^2}{2R_\infty} = \frac{2.303\varepsilon C}{S} \quad (2)$$

where ε is the absorptivity, C is the concentration and S is two times the scattering coefficient. Since S is not always known or easily measured and analyte concentration is

difficult to define for extended solid state materials, DR spectra are usually expressed in terms of the remittance using so called Kubelka-Munk units $[(1 - R_\infty)^2/2R_\infty]$.

Many MOFs contain linkers with optical spectroscopic signatures that have been well-established for their molecular counterparts. Metalloporphyrin-based MOFs are a prime example of this category.[48-49]The absorption spectra of porphyrins is best explained using the four-orbital Gouterman model[50] depicted in Figure 1.12. This model dictates that the absorption bands in porphyrin systems arise from transitions between the two HOMOs (a_{1u} and a_{2u} orbitals) and two LUMOs (degenerate e_g orbitals). Transitions between these orbitals produce two excited states of ^1E_u character. Through orbital mixing of these two excited states, a higher energy ^1E_u state, which produces the Soret band in the absorption spectrum, and a lower energy ^1E_u state, which give rise to the Q-bands in the absorption spectrum, are generated. Factors such as the metal ion identity and ring substituents affect the relative energies of these transitions, therefore changes in porphyrin Soret and Q-band regions with metal oxidation and spin state and axial ligation can be measured by optical DR. Following well-established precedent from metalloporphyrin molecular analogues, changes in the Soret band for the porphyrin-based MOF indicate axial interaction to the porphyrin metal sites with the adsorbed molecular guest species.

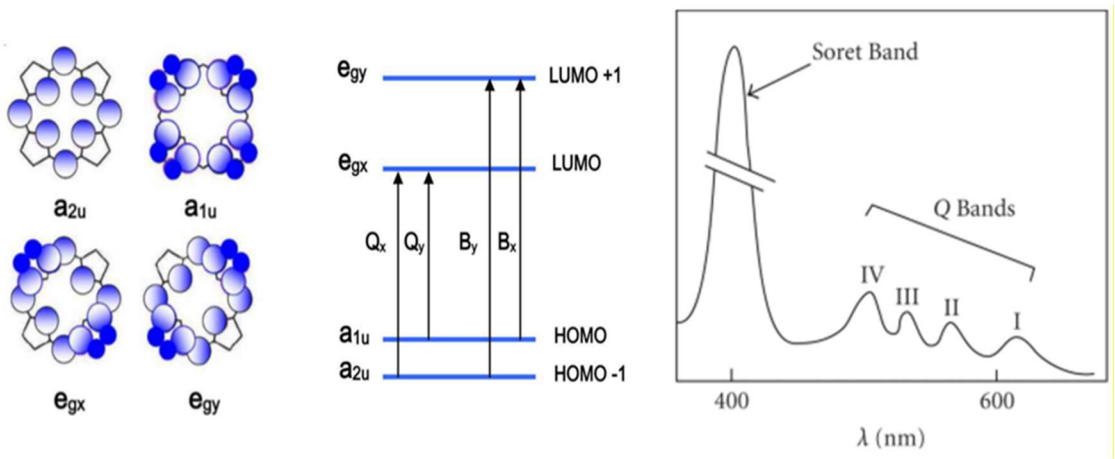

Figure 1.12 Depiction of Gouterman Model (left and middle) and representative spectrum (right) depicting the Soret and Q-bands associated with the described transitions.

1.5.3 X-ray Absorption Spectroscopy

X-ray absorption spectroscopy involves photoexcitation or ejection of core-level electrons, shown in Figure 1.13a. A core electron can be excited when the energy of the X-ray photon is equal or greater than its binding energy. This spectroscopy technique is therefore element-specific since each element has distinct core-level binding energies. A typical X-ray absorption spectrum is divided into two main regions; the X-ray absorption Near Edge Spectrum (XANES) and the Extended X-ray Absorption Fine Structure (EXAFS) regions. A general picture of an XAS spectrum is depicted in Figure 1.13b. The XANES region is comprised of what is known as the "pre-edge" and edge and provides information on the absorbing element's oxidation state and coordination geometry. The EXAFS region, interference between the ejected core electron (photoelectron) from the absorbing atom and the electrons of neighboring atoms. This region provides information on the type and distance of the nearest neighboring atoms, which can be used to understand the local structure of the absorbing atom. The EXAFS oscillations which are found well

above the absorption edge, are defined as $\mu(E)$, and can be extracted by removing the background and normalizing to the edge jump, shown in Figure 1.13, according to:

$$\chi(E) = \frac{\mu(E) - \mu_0(E)}{\Delta\mu_0(E)} \tag{1}$$

where $\mu(E)$ is the measured absorption coefficient, $\mu_0(E)$ is the smooth background function associated with adsorption by an isolated atom and $\Delta\mu_0(E)$ is the measured absorption edge jump. The X-ray energy of the photoelectron is usually converted to wavenumber, k with units of 1/distance according to:

$$k = \sqrt{\frac{2m_e(E - E_0)}{\hbar^2}} \tag{2}$$

where m_e is the electron mass and E_0 is the absorption edge energy. The set of frequencies contributing to the oscillations in $\chi(k)$ arise from the different neighboring coordination shells and can be extracted by fitting the EXAFS equation (3).

$$\chi(k) = \sum_j \frac{N_j f_j(k) e^{-2k^2\sigma_j^2}}{kR_j{}^2} \, sin[2kR_j + \delta_j(k)] \tag{3}$$

Where $f(k)$ and $\delta(k)$ are scattering properties of the atoms neighboring the excited atom, N is the number of neighboring atoms, R is the distance to the neighboring atoms, and σ^2 is the disorder in the neighbor distance. Analysis of both the XANES and EXAFS regions provide a comprehensive view of the element-specific local environment of the absorbing atom. X-ray absorption spectroscopy (XAS) has proved to be an extremely useful

technique in the characterization of biological protein systems and their analogues. More recently, XAS has been used to gather structural information in MOFs[56-59] in an effort to understand their catalytic, separation, and sensing applications.

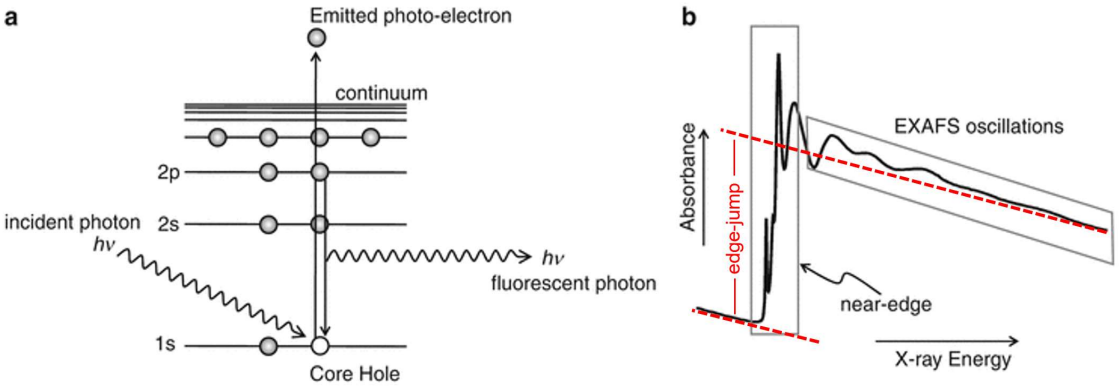

Figure 1.13 A) Illustration of X-ray absorption process. B) Illustration of regions of the X-ray absorption spectrum.[51]

1.5.4 X-ray Emission Spectroscopy

X-ray emission spectroscopy (XES) is directly related to XAS, in that it is a consequence of the absorption of a photon by a core electron. In XES the core hole that is created during the X-ray absorption process is subsequently filled by an electron from a higher level, which can result in the emission of a photon. Like XAS, XES is element specific since the elements of the sample emit X-rays at characteristic energies. This technique probes the occupied valence orbitals of a given material (complimentary to XAS which probes unoccupied orbitals), which provides valuable information on the electronic structure (local charge and spin density) as well as the nature of the bound

ligands and bonding interactions of a material. Because this thesis focuses on 3rd row transition metal complexes and MOFs, the relevant emission lines are the Kα and Kβ emission lines, shown in Figure 1.14. The lower energy Kα emission line involves 2p→1s transitions while Kβ main line XES involves 3p→1s. The resulting two main features, $K\beta_{1,3}$ and Kβ' arise from the exchange interaction between the 3p core hole and the partially filled 3d orbitals in the final state. The energy splitting and intensity ratio of the two features are sensitive to the number of unpaired electrons and therefore the spin state of the absorbing metal and is the primary XES emission line discussed in this thesis. The higher energy (lower intensity) Kβ so-called valence-to-core (VtC) features ($K\beta_{2,5}$/Kβ") arise from transitions from filled ligand np/ns orbitals to the metal 1s core-hole, which gain intensity through metal np mixing into filled valence orbitals. This is a powerful method of characterizing the ligand environment at the metal center.

Mainline Kβ XES is used in this thesis as a quantitative measure of determining local spin-state percentage in a metalloporphyrin-based MOF by utilizing a line shape analysis method known as the integrated area of the absolute values of difference spectra (IAD)[52-54]. This line shape analysis method takes advantage of the finding that IAD values scale linearly with the difference in number of unpaired electrons (ΔS) associated with the spectra used to generate the difference spectra. The effective average spin state of an unknown mixed-spin system can therefore be compared to a known spin state system. The relevant equations used for the IAD analysis are shown below:

$$\Delta S_{ML} = \frac{IAD_{ML}\Delta S_{HL}}{IAD_{HL}} \quad (4)$$

$$IAD_{HL} = \int |[HS(E) - LS(E)]|dE \quad (5)$$

$$IAD_{ML} = \int |[MS(E) - LS(E)]|dE \quad (6)$$

where IAD_{HL} is the absolute area of high spin – low spin difference spectrum, IAD_{ML} is the absolute area of unknown spin – low spin difference spectrum, ΔS_{HL} is the difference between spin state values for high and low spin reference compounds, and ΔS_{ML} is the difference between spin state values of unknown compound and the low spin reference. Using the IAD analysis, effective spin state of species with unknown spin can be determined by plotting the obtained IAD values vs. the spin state of the reference complexes used to generate the IAD.

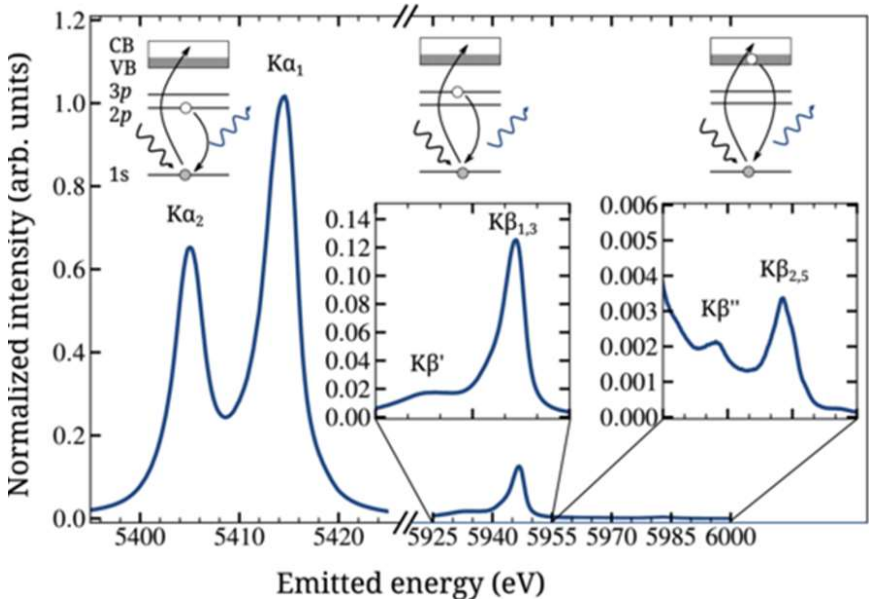

Figure 1.14 Illustration of the X-ray emission process and resulting spectra.[55]

1.6 References

[1] Britt, D.; Furukawa, H.; Wang, B.; Glover, T. G.; Yaghi, O., *PNAS* **2009,** *106* (49), 20637-20640.

[2] Li, H.; Eddaoudi, M.; O'Keeffe, M.; Yaghi, M., *Nature (London)* **1999,** *402* (6759), 276-279.

[3] Furukawa, H.; Yaghi, O. M., *J. Am. Chem. Soc.*, 2009, **131**, 8875-8883.

[4] Li, J.-R.; Kuppler, R. J.; Zhou, H.-C., *Chem. Soc. Rev.* **2009,** *38* (5), 1477-1504.

[5] Lu, Z.; Knobler, C. B.; Furukawa, H.; Wang, B.; Liu, G.; Yaghi, O. M., *J. Am. Chem. Soc.* **2009,** *131* (35), 12532-12533.

[6] Chae, H. K.; Siberio-Perez, D. Y.; Kim, J.; Go, Y. B.; Eddaoudi, M.; Matzger, A. J.; O'Keeffe, M.; Yaghi, O. M., *Nature (London, U. K.)* **2004,** *427* (6974), 523-527.

[7] Furukawa, H.; Cordova, K. E.; O'Keeffe, M.; Yaghi, O. M., *Science (Washington, DC, U. S.)* **2013,** *341* (6149), 974.

[8] Furukawa, H.; Ko, N.; Go, Y. B.; Aratani, N. Choi, S. B.; Chi, E.; Yazaydin, A. Q.; Snurr, R. Q.; O'Keefe, M.; Kim, J.; Yaghi, O. M., *Science*, 2010, **329**, 424-428.

[9] Rowsell, J. L. C.; Millward, A. R.; Park, K. S.; Yaghi, O. M., *J. Am. Chem. Soc.,* 2004, **126**, 5666-5667.

[10] Samsonenko, D. G.; Kim, H.; Sun, Y.; Kim, G. -H.; Lee, H. -S.; Kim, K., *Chem. Asian J.*, 2007, **2**, 484 – 488.

[11] Matsuda, R.; Kitaura, R.; Kitagawa, S.; Kubota, Y.; Belosludov, R. V.; Kobayashi, T. C.; Sakamoto, H.; Chiba, T.; Takata, M.; Kawazoe, Y.; Mita,Y., *Nature*, 2005, **436**, 238-241.

[12] Li, R.J.; Kuppler, R. J.; Zhou, H. C., *Chem. Soc. Rev.*, 2009, **38**, 1477–1504.

[13] D'Alessandro, D. M.; Smit, B.; Long, J. R., *Angew. Chem. Int. Ed.*, 2010, **49**, 6058–6082.

[14] Ma, S.; Wang, X. S.; Yuan, D.; Zhou, H. C., *Angew. Chem. Int. Ed.*, 2008, **47**, 4130-4133.

[15] Carboni, M.; Abney, C. W.; Liu, S.; Lin, W., *Chem. Sci.*, 2013, **4**, 2396-2402.

[16] Sumida, K.; Rogow, D. L.; Mason, J. A.; McDonald, T. M.; Bloch, E. D.; Herm, Z. R.; Bae, T. -H.; Long, J. R., *Chem. Rev.,* 2012, **112**, 724–781.

[17] Valvekens, P.; Vermoortele, F.; De Vos, D., *Catal. Sci. Technol.* **2013,** *3* (6), 1435-1445.

[18] Diercks, C. S.; Kalmutzki, M. J.; Diercks, N. J.; Yaghi, O. M., *ACS Cent. Sci.* **2018,** *4* (11), 1457-1464.

[19] Bhyrappa, P., *Tetrahedron Letters*, **2016**, *57* (47), 5150-5167.

[20] Shelnutt, J. A.; Song, X. -Z.; Ma, J. -G.; Jia, S. -L, Jentzen, W.; Medforth, C. J., *Chem. Soc. Rev*. **1998**, *27*, 31-41.

[21] Makarska, M.; Radzki, S., *Annales Universitatis Mariae Curie-Skodowska. Sectio AA, Chemia.* **1980**, *57*, 332-363

[22] J. T. Groves, T. E. Nemo and R. S. Myers, *J. Am. Chem. Soc*., **1979**, *101*, 1032.

[23] Gunter, M. J.; Turner, P., *Coord. Chem. Rev.* **1991**, *108*, 115-161.

[24] J.T. Groves and T.J. McMurray, in P.R. Ortiz de Montallano (Ed.), Cytochrome P-450: Structure, Mechanism and Biochemistry, Plenum Press, New York, 1986.

[25] Collman, J. P.; Halbert, T. R.; Suslick, K. S. In Metal Ion Activation Of Dioxygen; Spiro,T. G., ed.; Prentice Hall: New York, 1980; pp 1-72.

[26] Collman, J. P.; Brauman, J. I.; Suslick, K. S., *J. Am. Chem. Soc*. **1975**, 97, 7185-7186.

[27] Collman, J. P.; Brauman, J. I.; Doxsee, K. M.; Halbert, T. R.; Hayes, S. E.; Suslick, K. S. *J. Am. Chem. Soc.* **1978**, 100, 2761-2766.

[28] Suslick, K. S.; Bhyrappa, P.; Chou, J. -H.; Kosal, M. E.; Nakagaki, S.; Smithenry, D. W.; Wilson, S. R., *Acc. Chem. Res.* **2005**, *38*, 283-291.

[29] Farha, O. K.; Shultz, A. M.; Sarjeant, A. A.; Nguyen, S. T.; Hupp, J. T., *J. Am. Chem. Soc.* **2011,** *133* (15), 5652-5655.

[30] Fateeva, A.; Devautour-Vinot, S.; Heymans, N.; Devic, T.; Greneche, J.-M.; Wuttke, S.; Miller, S.; Lago, A.; Serre, C.; De Weireld, G.; Maurin, G.; Vimont, A.; Ferey, G., *Chem. Mater.* **2011,** *23* (20), 4641-4651.

[31] Feng, D.; Jiang, H. -J.; Chen, Y. -P.; Gu, Z. -Y.; Wei, Z.; Zhou, H. -C., *Inorg. Chem*. 2013, *52*, 12661−12667.

[32] D. Feng, Z.-Y. Gu, J.-R. Li, H.-L. Jiang, Z. Wei, H.-C. Zhou, *Angew. Chem. Int. Ed.*, **51**, 10307-10310 (2012).

[33] Feng, D.; Gu, Z. -Y.; Chen, Y. -P.; Park, J.; Wei, Z.; Sun, Y.; Bosch, M.; Yuan, S.; Zhou, H. -C., *J. Am. Chem. Soc.* **2014**, *136*, 17714−17717.

[34] Feng, D.; Chung, W. -C.; Wei, Z.; Gu, Z. -Y.; Jiang, H. -L.; Chen, Y. -P.; Darensbourg, D. J.; Zhou, H. -C., *J. Am. Chem. Soc*. **2013**, *135*, 17105−17110.

[35] Jiang, H. -L.; Feng, D.; Wang, K.; Gu, Z. -Y.; Wei, Z.; Chen, Y. -P.; Zhou, H. -C., *J. Am. Chem. Soc*. **2013**, *135*, 13934−13938.

[36] Chen, Y.; Hoang, T.; Ma, S., *Inorg. Chem.* **2012,** *51* (23), 12600-12602.

[37] Morris, W.; Volosskiy, B.; Demir, S.; Gandara, F.; McGrier, P. L.; Furukawa, H.; Cascio, D.; Stoddart, J. F.; Yaghi, O. M., *Inorg. Chem.* **2012,** *51* (12), 6443-6445.

[38] Dietzel, P. D. C.; Morita, Y.; Blom, R.; Fjellvaag, H., *Angew. Chem., Int. Ed.* **2005,** *44* (39), 6354-6358.

[39] Dietzel, P. D. C.; Panella, B.; Hirscher, M.; Blom, R.; Fjellvag, H., *Chem. Commun. (Cambridge, U. K.)* **2006,** (9), 959-961.

[40] Dietzel, P. D. C.; Johnsen, R. E.; Fjellvaag, H.; Bordiga, S.; Groppo, E.; Chavan, S.; Blom, R., *Chem. Commun. (Cambridge, U. K.)* **2008,** (41), 5125-5127.

[41] Li, J. -R.; Kuppler, R. J. Zhou, H. -C., *Chem. Soc. Rev.* **2009**, (38), 1477-1504.

[42] Lucier, B. E. G.; Chen, S.; H, Y., *Acc. Chem. Res.* **2018,** (51), 2319-330.

[43] Hoffmann, H. C.; Debowski, M.; Müller, P.; Paasch, S.; Senkovska, I., Kaskel, S.; & Brunner, E., **2012**, *Materials*, *5*(12), 2537–2572.

[44] M. Kozuka, K. Nakamoto, *J. Am. Chem. Soc.*, **1981**, *103*, 2162-2168.

[45] H. Oshio, T. Ama, T. Watanabe, J. Kincaid, K. Nakamoto, *Spectrochim. Acta A*, **1984**, *40*, 863-870.

[46] A. Bianconi, A. Congiu-Castellano, M. Dell'Ariccia, A. Giovannelli, P. J. Durham, E. Burattini, M. Barteri, FEBS Lett., **1984**, *178*, 165-170.

[47] T. Kitagawa, M. Abe, H. Ogoshi, *J. Chem. Phys.*, **1978**, *69*, 4516-4525.

[48] Gallagher, A T; Lee, J Y; Kathiresan, V; Anderson, J S; Hoffman, B M; Harris, T D, **2018**, *Chemical Science*, **9**, 1596.

[49] Shaikh, S; Chakraborty, A; Alatis, J; Cai, M; Danilov, E O; Morris, A J, **2018**, *Faraday Discussions.*

[50] Spellane, P. J.; Gouterman, M.; Antipas, A.; Kim, S.; Liu, Y. C., *Inorg. Chem.* **1980**, *19*, 386-391.

[51] George, G. N.; Pickering, I. J., X-Ray Absorption Spectroscopy of Metals in Biology. In *Encyclopedia of Biophysics*, Roberts, G. C. K., Ed. Springer Berlin Heidelberg: Berlin, Heidelberg, 2013; pp 2762-2767.

[52] Vanko, G.; Neisius, T.; Molnaŕ , G.; Renz, F.; Kaŕ paťi, S.; Shukla, A.; de Groot, F. M. F., *J. Phys. Chem. B*, **2006**, *110*, 11647−11653.

[53] Glatzel, P.; Bergmann, U., *Coord. Chem. Rev.* **2005**, *249*, 65−95.

[54] Vanko, G.; Rueff, J.-P.; Mattila, A.; Neḿ eth, Z.; Shukla, A. *Phys. Rev. B: Condens. Matter Mater. Phys*. **2006**, *73*, 024424.

[55] Rovezzi, M.; Glatzel, P., *Semiconductor Science and Technology*. **2014**, *29* (2), 023002.

[56] de Combarieu, G.; Hamelet, S.; Millange, F.; Morcrette, M.; Tarascon, J.-M.; Ferey, G.; Walton, R. I., *Electrochem. Commun.* **2009,** *11* (10), 1881-1884.

[57] Chavan, S.; Bonino, F.; Vitillo, J. G.; Groppo, E.; Lamberti, C.; Dietzel, P. D. C.; Zecchina, A.; Bordiga, S., *Phys. Chem. Chem. Phys.* **2009,** *11* (42), 9811-9822.

[58] Bonino, F.; Chavan, S.; Vitillo, J. G.; Groppo, E.; Agostini, G.; Lamberti, C.; Dietzel, P. D. C.; Prestipino, C.; Bordiga, S., *Chem. Mater.* **2008,** *20* (15), 4957-4968.

[59] Drisdell, W. S.; Poloni, R.; McDonald, T. M.; Long, J. R.; Smit, B.; Neaton, J. B.; Prendergast, D.; Kortright, J. B., *J. Am. Chem. Soc.* **2013,** *135* (48), 18183-18190.

[60] Yang, X; Xu, Q, *Crystal Growth & Design.* **2017**, *17*, 1450.

[61] Sumida, K; Rogow, D L; Mason, J A; McDonald, T M; Bloch, E D; Herm, Z R; Bae, T-H; Long, J R, *Chemical Reviews*. **2012**, *112*, 724.

[62] Li, J-R; Ma, Y; McCarthy, M C; Sculley, J; Yu, J; Jeong, H-K; Balbuena, P B; Zhou, H-C, *Coordination Chemistry Reviews*. **2011**, *255*, 1791.

[63] Murray, L J; Dinca, M; Long, J R, *Chemical Society Reviews*. **2009**, *38,* 1294.

[64] Li, J-R; Kuppler, R J; Zhou, H-C, *Chemical Society Reviews*. **2009**, *38,* 1477.

[65] Drake, T; Ji, P; Lin, W, *Accounts of Chemical Research*. **2018**, *51,* 2129.

[66] Wu, C-D; Zhao, M, *Advanced Materials*. **2017**, *29,* 1605446.

[67] Dhakshinamoorthy, A; Asiri Abdullah, M; Garcia, H, *Chemistry – A European Journal*. **2016**, *22,* 8012.

[68] Cui, Y; Yue, Y; Qian, G; Chen, B, *Chemical Reviews*. **2012**, *112*, 1126.

[69] Hu, Z; Deibert, B J; Li, J, *Chemical Society Reviews*. **2014**, *43,* 5815.

Chapter 2. Spectroscopic interrogations of isostructural metalloporphyrin-based metal-organic frameworks with strongly and weakly coordinating guest molecules

2.1 Introduction

To promote the availability of the metal axial binding sites through host-guest interactions, much effort has been dedicated to the incorporation of these metal complexes in porous solid state networks.[1,2] Early strategies based on crystallization of various meso-substituted metalloporphyrin complexes successfully produced cavities for small molecule access to the metal centers.[3-6] However, the relatively weak interactions that hold these porphyrin solids together often lead to porous structure instabilities, particularly after solvent removal.

A more promising approach involves incorporating porphyrins or metalloporphyrins as linkers in metal-organic frameworks (MOFs).[7-11] MOFs are self-assembled 3D networks of metal ions or clusters connected through coordination bonds with organic linker molecules. Upon solvent removal, these crystalline architectures retain their structure and exhibit microporosity, which makes them appealing for adsorption-based applications.[12,13] Moreover, the tunablity of the MOF structures affords potential reactivity controls through pore size and shape selectivity. In many porphyrin-based MOFs, high-valency metals that form stable metal-linker coordination bonds, such as Al(III) and Zr(IV), occupy the framework node positions with full coordination, while metals prone to accommodate coordination and oxidation state changes can be incorporated (pre- or post-synthetically) in the porphyrin linkers that connect these nodes.[7,8,14] With this motif, pore-wall accessible metals can be included for guest molecule binding or reaction without compromising the overall structural integrity or chemical/thermal stability of the

framework. Many porphyrin-based MOFs have been reported using this strategy, yet despite great progress in building these architectures and in showing their propensity for catalytic and small molecule binding behavior,[7,15-10] surprisingly few studies have been carried out to probe the local interactions and structural consequences of the metalloporphyrin units within the framework. These molecular level insights, however, are undoubtedly important for understanding and ultimately controlling catalytic behavior in these materials.

This chapter focuses on molecular level host-guest interactions in the metalloporphyrin MOF structure shown in Figure 2.1. The framework, reported as PCN222,[7] MOF-545,[8] or MMPF-6[20] is comprised of Zr_6 nodes connected by carboxyphenyl meso-substituted metalloporphyrins to produce two types of 1D channels along the c-axis (diameters of ~37Å and ~10Å).

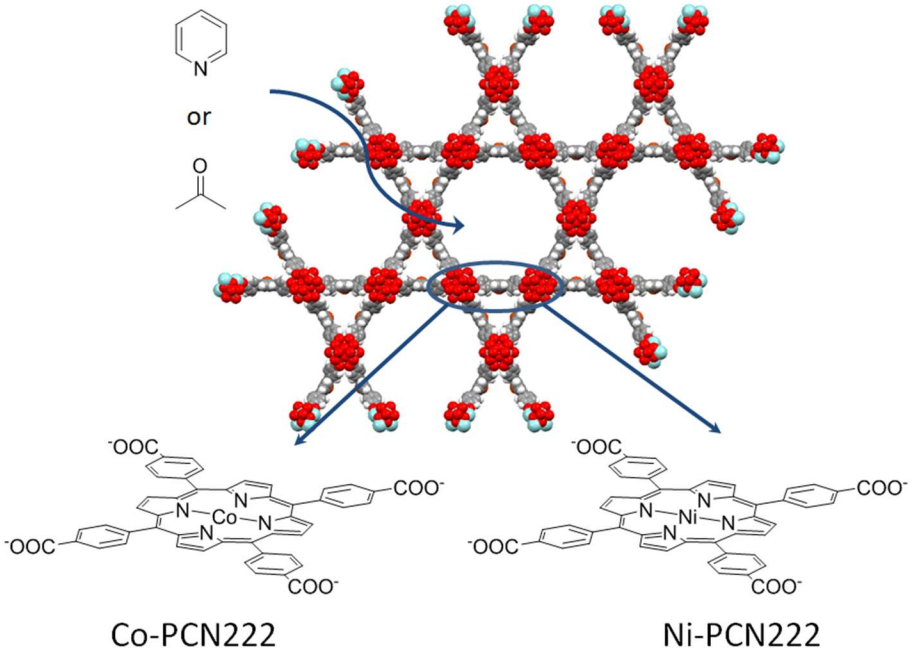

Figure 2.1 PCN222 architecture, linker structure, and interaction of PCN222 with guest molecules: acetone and pyridine.

Presented in this chapter is a systematic study of isostructural versions of this framework with different porphyrin linker metal centers (Co and Ni) in both weakly and strongly coordinating guest molecule environments using both X-ray absorption (XAS) and resonance Raman spectroscopy. These spectroscopy methods have been used extensively to probe the electronic and geometric structures of metalloporphyrin complexes in various solution, protein, and other environments.[22-38] Moreover, having been well established in the study of other solid state porous materials such as zeolites,[39-44] XAS and Raman spectroscopy are now often incorporated in the arsenal of characterization methods for MOF materials in general to provide new insights on potentially important metal electron distribution and framework and/or guest molecule structural changes that occur upon host-guest adsorption events.[45-50] In this study, these spectroscopy techniques are used to provide new insights on the metalloporphyrin local structure and coordination environment under the structural constraints of the framework and under coordinating and non-coordinating guest molecule conditions.

2.2 Results

2.2.1 Characterization Methods

The crystal structures of the synthesized MOFs were verified using powder XRD. Peak patterns of the as-synthesized frameworks shown in Figure 2.2 match those reported in the literature for this MOF series.[7] Consistent patterns are obtained for these MOF samples after activation and post-synthetic guest molecule inclusion, indicating that the crystal structure is maintained in each case upon these treatments.

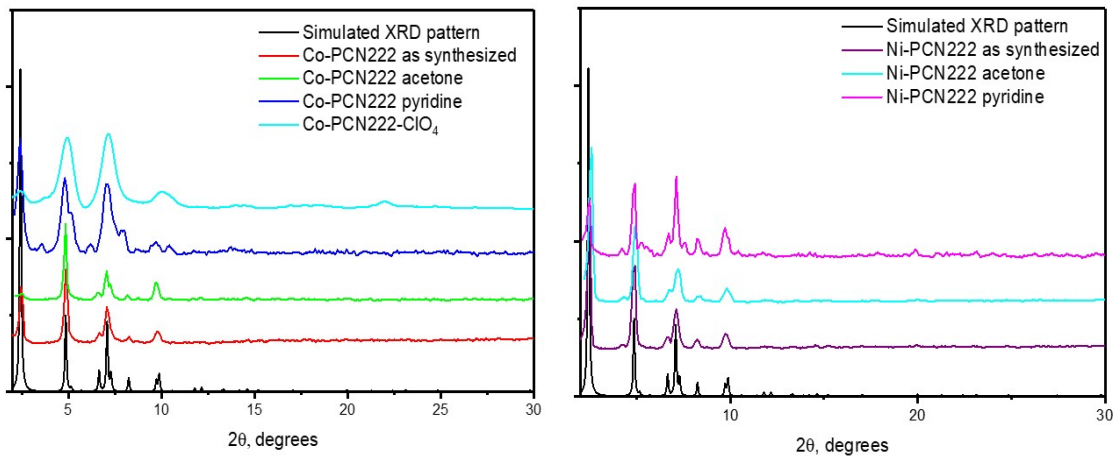

Figure 2.2 Simulated and experimental PXRD patterns of Co-PCN222 and Ni-PCN222 samples.

Diffuse reflectance UV-vis spectra of the reference TCPP metalloporphyrin complexes in the solid state were compared with the corresponding M-PCN-222 MOF samples upon exposure to different guest environments, as shown in Figure 2.3. For the Co and Ni porphyrin MOF spectra, both Soret and Q bands appear at the same peak wavelengths with similar spectra shape as those of the corresponding MTCPP (M=Co or Ni; TCPP=tetracarboxyphenyl porphyrin) reference complexes.

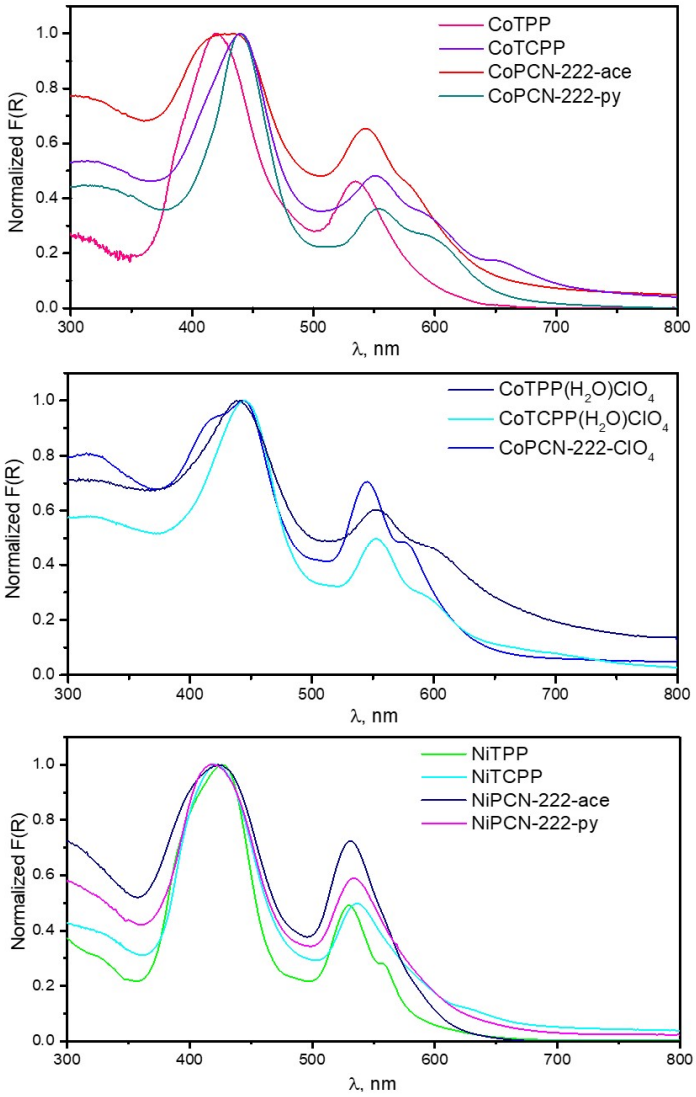

Figure 2.3 Diffuse reflectance spectra of reference Co(II) (top), Co(III) (middle) and Ni(II) complexes and MOFs exposed to different guest environments

Infrared spectra of the metalloporphyrin MOFs are presented and compared to those of the relevant reference complexes in Figures 2.4. These data were used mainly to characterize the vibrational modes and to confirm the presence of the guest molecules inside the pores of the MOF.

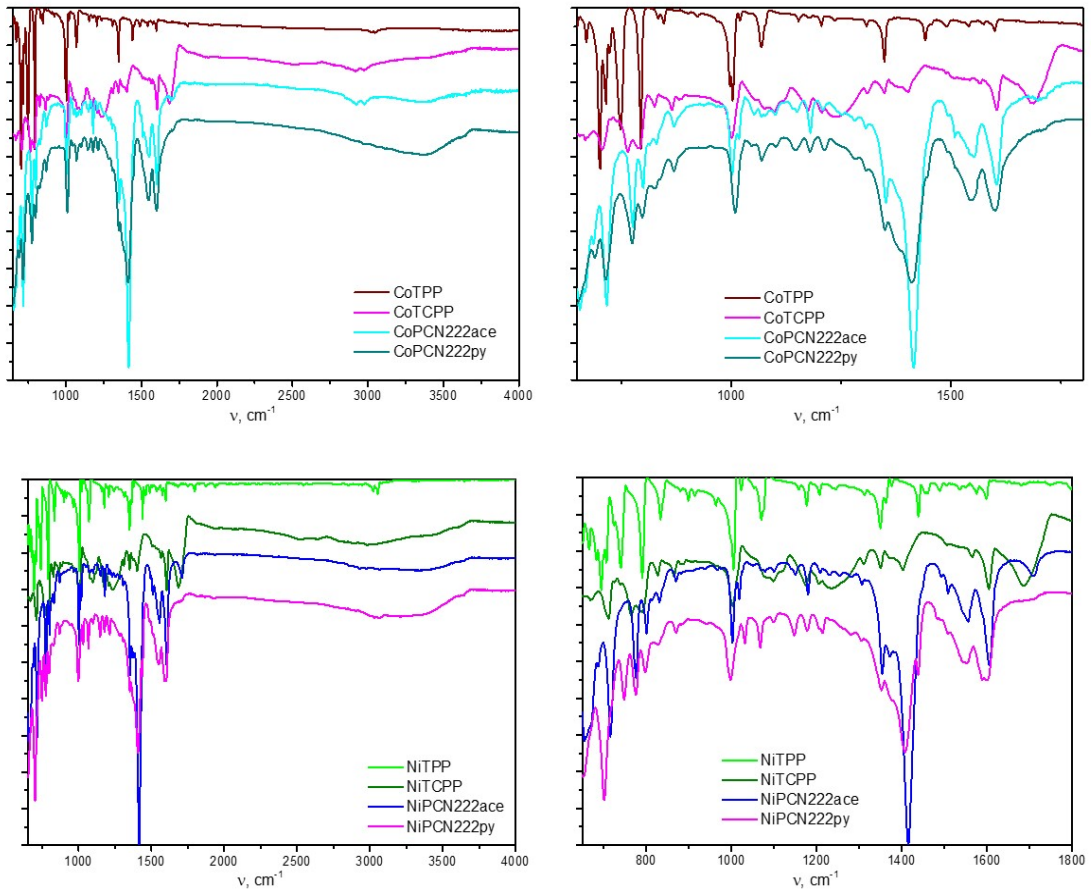

Figure 2.4 IR spectra of model metalloporphyrin complexes and MOFs with different guest molecules.

In the CoTCPP, and NiTCPP complexes, the carboxylic acid stretching mode appears in the IR spectra as a strong feature in the range 1685-1691 cm^{-1}. In the MOF systems, the resulting asymmetric carboxylate modes appear at 1554-1556 $cm^{-1}$and a strong broad band around 1405 cm^{-1} is assigned to overlapping C-C aromatic stretch and symmetric -COO^- stretch peaks.[52] These carboxylate mode frequencies, which are consistent with the bridging type coordination with Zr in the MOF,[53] are observed at slightly higher frequencies for the MOFs treated with acetone compared to pyridine. These frequency differences, however, are nearly identical for both the Co and Ni versions of the MOF, which most likely reflects the different electrostatic environments created by the two

solvents around the pore-exposed carboxylate bonds rather than indicates any differences in axial interaction of these guest molecules with the metalloporphyrin sites. Moreover, these carboxylate bands partially overlap with the porphyrin modes in this frequency range. The resulting congested fingerprint region prevents further analysis of the structure sensitive porphyrin modes to establish the more subtle electronic and structural consequences of incorporating these metalloporphyrins in MOF structures and under guest molecule environments. Vibrational signature of the guest species are clearly observed and confirm their presence in the treated MOF samples. For M-PCN222-ace, aliphatic ν(C-H) appears at 2920 – 2927 cm^{-1} and ν(C=O) at 1706 – 1710 cm^{-1}. Pyridine has a strong band at 1438 cm^{-1} ν(C=C) which is clearly seen in the spectra of the MOFs treated with this solvent.

2.2.2 Resonance Raman Spectroscopy

Selected spectral regions highlighting the structure sensitive modes of the metalloporphyrin complexes and MOFs are presented in Figures 2.5 and 2.6. A summary of these vibrational mode frequencies is provided in Table 2.1. Full Raman spectra for the isostructural MOF series and corresponding metalloporphyrin reference complexes are presented in Figure 2.7. 420 nm excitation is resonant with the Soret band region of the porphyrin electronic absorption spectra and leads to significant enhancement of the porphyrin skeletal vibrational modes. This selective enhancement allows clear assessment of the porphyrin localized modes, providing a distinct advantage over IR spectroscopy, which frequently yields poorly resolved congested fingerprint regions. Raman spectra of model complexes are consistent with those reported in the literature.[25,26,54-57] Most modes

are assigned as in-plane skeletal modes that involve either a combination of C-C stretches, for example ν_2, and ν_3, or pyrrole ring deformation: ν_1, and ν_4. These modes appear in the region of the spectrum from around 1000 to 1600 cm^{-1}. C-C stretch modes localized on the peripheral phenyl groups, labeled φ_4 and φ_5, are also observed in this fingerprint region. Another important mode is ν_8, which is assigned to M-N breathing with porphyrin ring deformation. This low frequency mode appears in the range ~380-400 cm^{-1} for the porphyrin systems measured in this study. (Mode assignment and notation follows that of the normal coordinate analysis reported in reference[56] and summarized in chapter 1.)

Table 2.1 Structure sensitive Raman modes for reference M-TPP complexes, their TCPP analogues, and M-PCN222 MOFs in the presence of acetone or pyridine

Porphyrin system	ν_8	ν_1	ν_4	ν_3	φ_5	ν_2	φ_4
CoTPP	393	1237	1371	-	1504	1565	1600
CoTCPP	378	1239	1370	1486	1511	1569	1608
CoPCN222ace	384	1238	1371	1486	1510	1570	1607
CoPCN222py	385	1239	1372	1485	1510	1570	1608
NiTPP	402	1234	1374	1470	1502	1572	1595
NiTCPP	383	1238	1373	1472	1511	1573	1608
NiPCN222ace	389	1236	1373	1473	1509	1573	1608
NiPCN222py	389	1237	1373	1473	1509	1573	1608

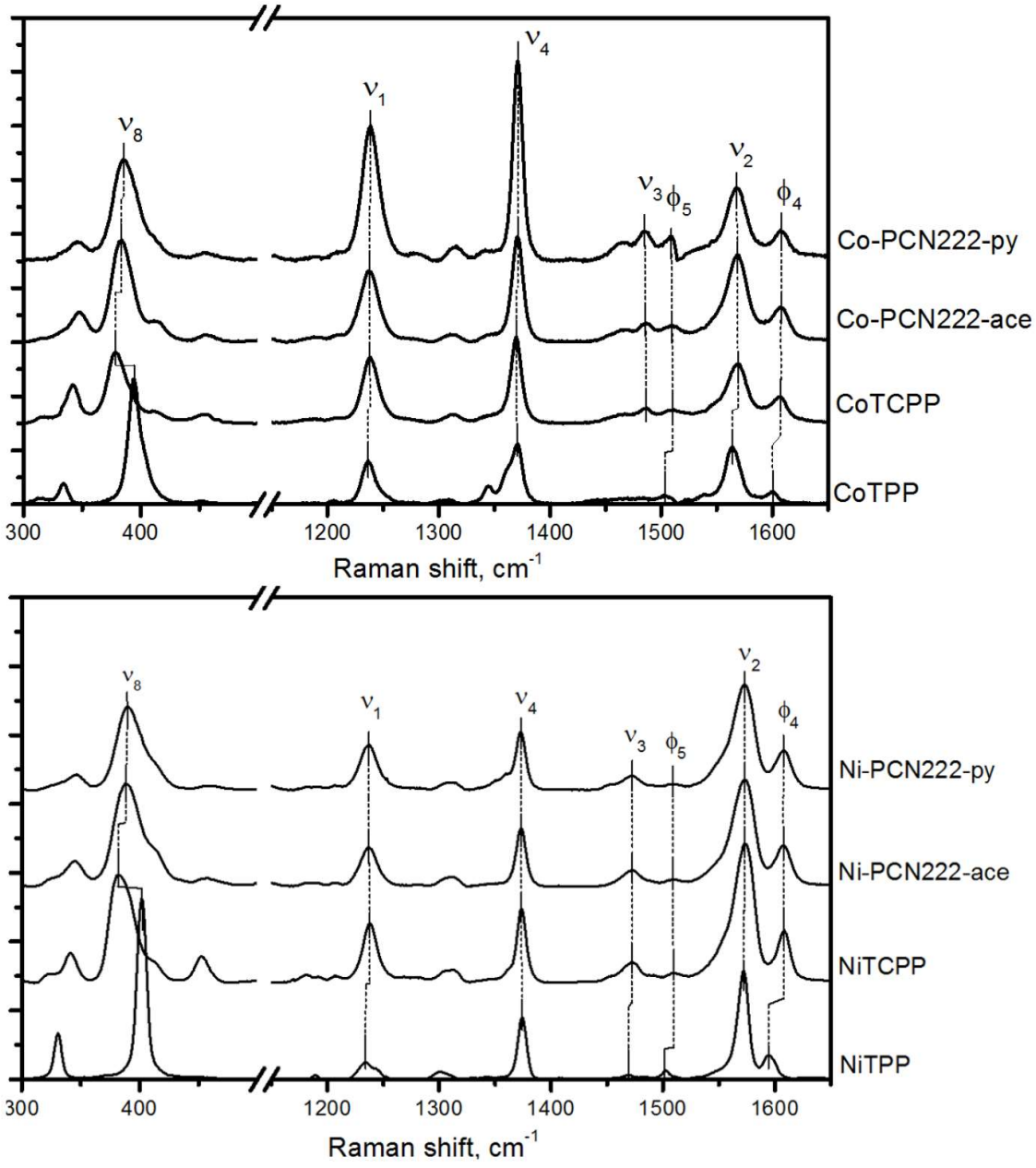

Figure 2.5 Comparison of resonance Raman spectra of: (top) CoTPP, CoTCPP, and Co-PCN-222 in the presence acetone or pyridine guest molecules; (bottom) NiTPP, NiTCPP, and Ni-PCN-222 in the presence acetone or pyridine.

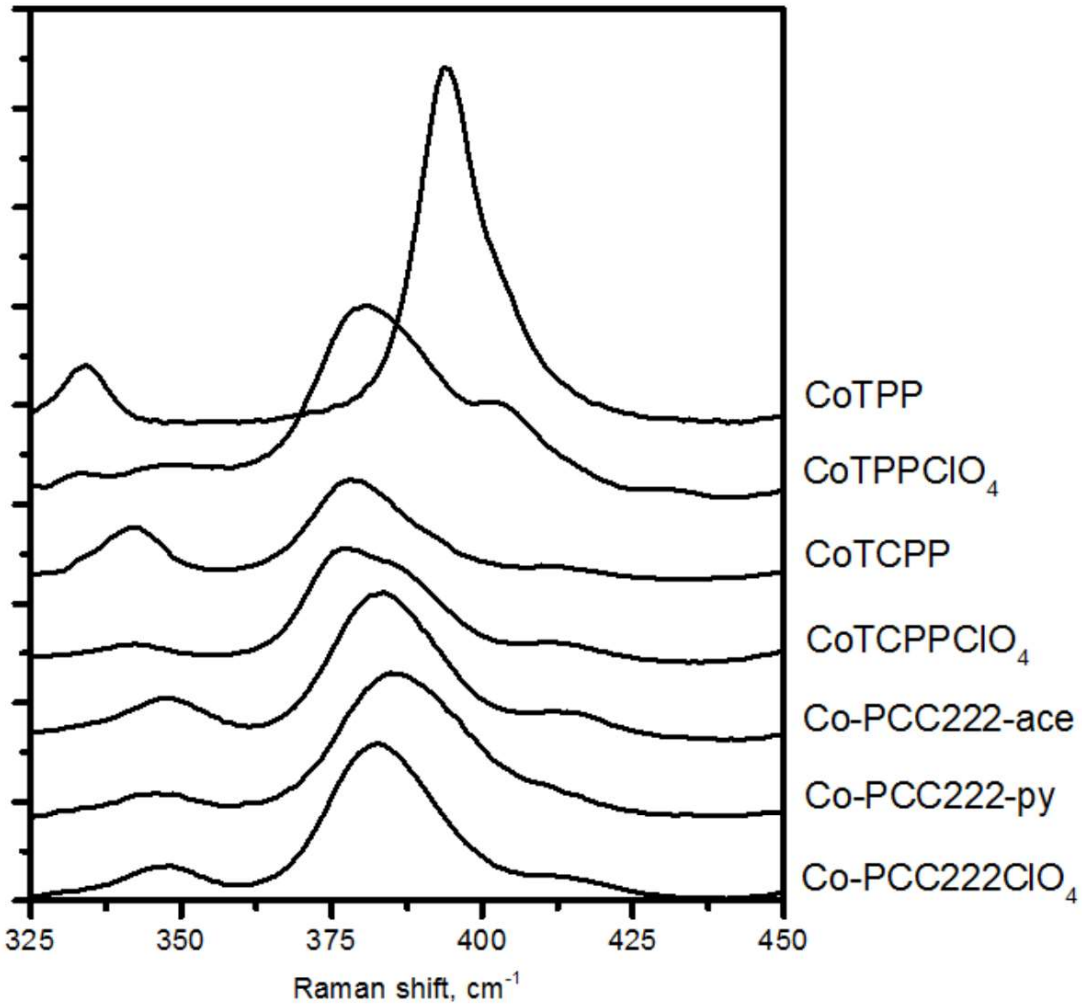

Figure 2.6 Resonance Raman spectral region highlighting ν_8 mode: comparison of Co(II) and Co(III) complexes and MOFs.

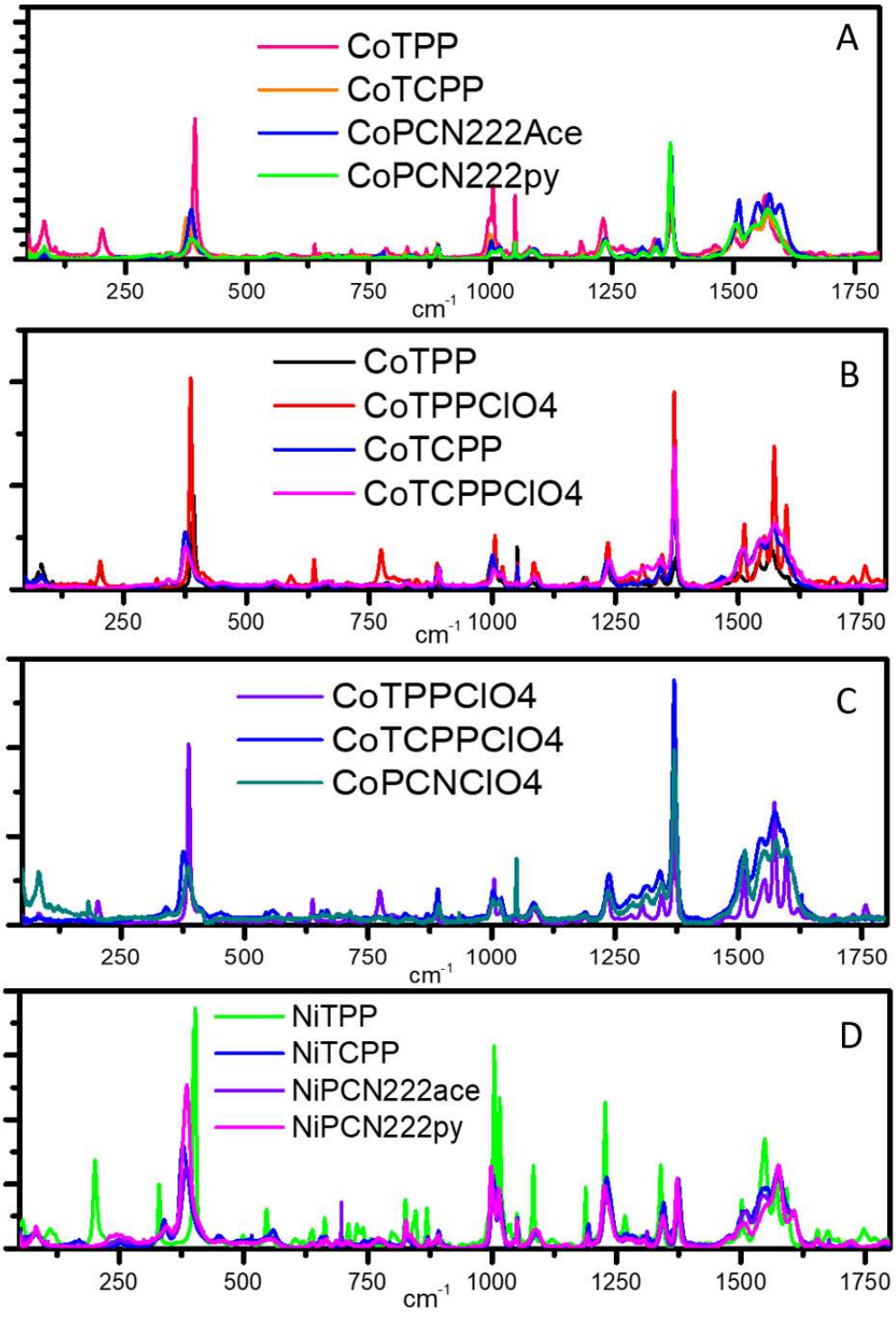

Figure 2.7 Full Raman spectra for the isostructural MOF series and corresponding metalloporphyrin reference complexes. A) Co(II) species B) comparison of Co(II) and Co(III) species with and without carboxylate functionality C) Co(III) species D) Ni(II) species

2.2.3 X-ray absorption spectroscopy

The XAS data for the metalloporphyrin complexes and MOFs are presented in Figures 2.8 and 2.9. The XANES spectra for the Co-porphyrin systems contain both pre-edge and edge features at around 7710 and 7715 eV respectively, which are consistent with the values reported for Co(II) porphyrin XANES spectra.[58] The intensity of the edge feature varies significantly among the set, with the square planar CoTPP and (guest free) activated Co-PCN222 spectra having the highest intensity and Co-PCN222-py spectrum having minimal intensity for this edge feature. The spectra are overlaid with those of the oxidized Co-PCN222 MOF and Co(III) reference complex, $CoTPP(H_2O)_2ClO_4$ for comparison. NiTCPP, Ni-PCN222-ace and Ni-PCN222-py produce nearly the same XANES spectra consisting of a very weak pre-edge feature at around 8333 eV and a more intense edge feature at 8337.5 eV. These results are consistent with the reported XANES spectrum of NiTPP.[59]

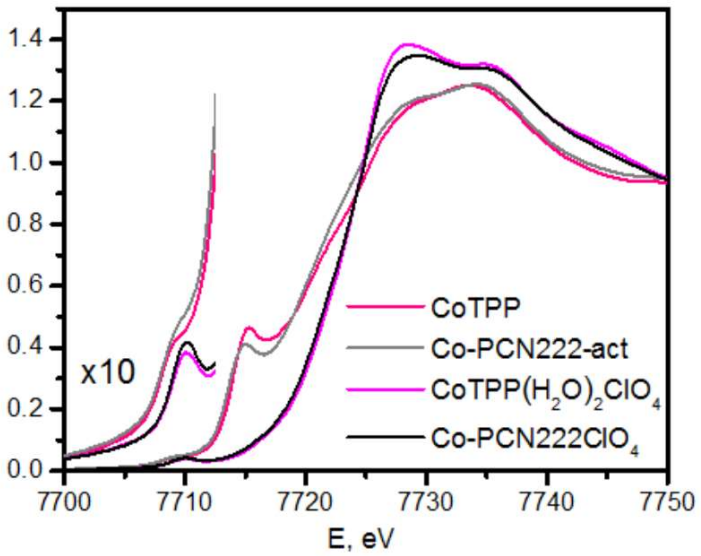

Figure 2.8 XANES spectra of CoTPP, Co-PCN222-act, $CoTPP(H_2O)_2ClO_4$, , and Co-PCN222-ClO_4

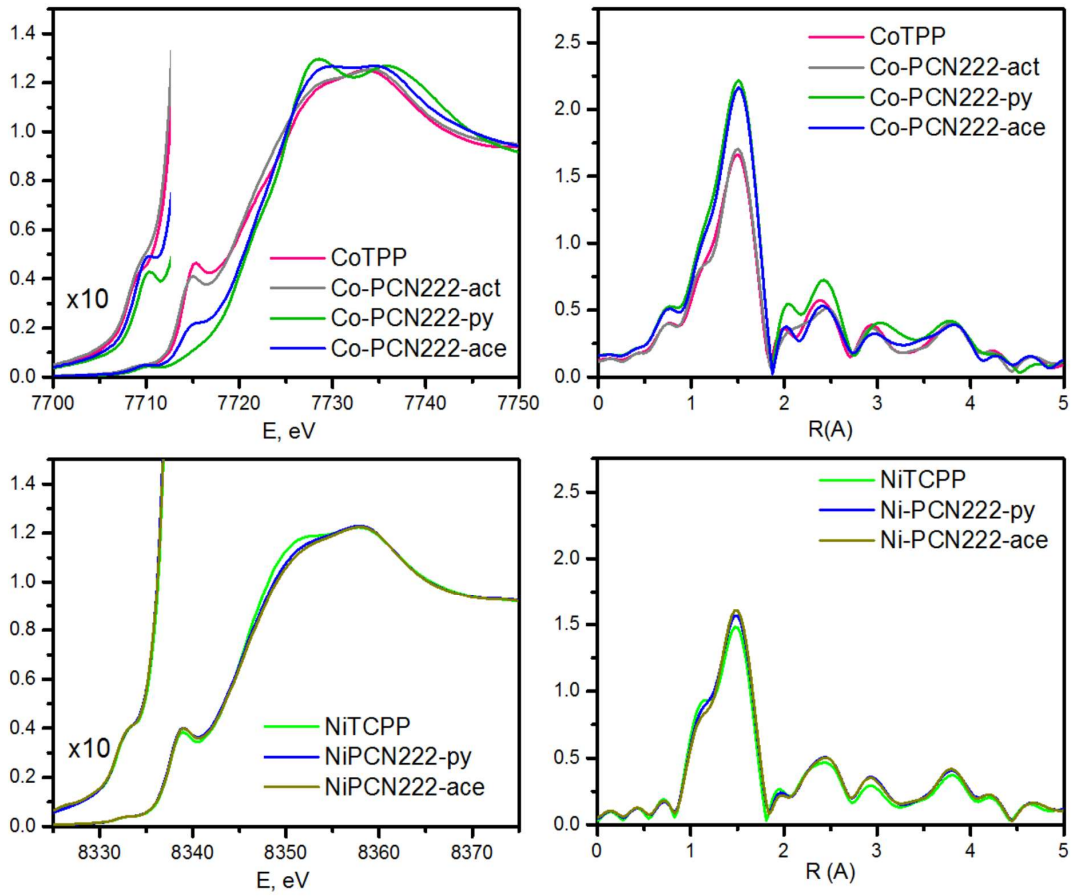

Figure 2.9 XANES and EXAFS spectra of: (top) CoTPP and Co-PCN-222 activated and in the presence acetone or pyridine guest molecules; (bottom) NiTCPP and Ni-PCN222 in the presence acetone or pyridine.

2.3 Discussion

2.3.1 Electronic and structural changes upon porphyrin carboxylate functionalization and framework integration.

Several metalloporphyrin ring vibrational modes observed in the resonance Raman spectra (Figure 2.5) can provide useful insights on the electronic and structural consequences of framework integration of this macrocycle due to their sensitivity to

porphyrin ring functionalization and distortion. For example, the frequency of the mode containing prominent M-N stretching displacement, ν_8 is shown to be quite sensitive to the TPP ring phenyl group functionalization and incorporation in the MOF environment. For the CoTPP complex, ν_8 occurs at 393 cm^{-1}, yet is shifted 17 cm^{-1} to lower energy in CoTCPP. A similar frequency trend is also observed for the Ni complexes when comparing the TPP and TCPP versions. The drastic change in the frequency for ν_8 in these systems is attributed to the addition of the electron-withdrawing carboxylic acid groups to the TPP ring, which effectively weakens the metal porphyrin coordination bonds and decreases the force constant of the M-N stretch. Placing the carboxylate functionalized complexes in the MOF environment has the opposite effect on this mode which also includes a substantial ring distortion component. The increased rigidity of the framework yields upshifted frequencies of ν_8 for both M-PCN222 MOFs by +6 to +9 cm^{-1} depending on the metal, compared to that of the corresponding TCPP complexes. In most other metalloporphyrin systems, this mode exhibits primary sensitivity to the metal oxidation state since the metal ion size and charge strongly affect the porphyrin core size and therefore the force constant of this mode.[25] To evaluate the relative influence of the peripheral functionality and framework incorporation on this mode frequency compared to the influence of the metal oxidation state, Raman spectra of the oxidized Co(III) porphyrin complexes and MOF were compared with those of the Co(II) system analogues. Only different oxidation states of the Co systems were investigated due to the instability of other Ni-porpohyrin oxidation states besides Ni(II). The oxidation state for all systems was first confirmed by XAS. The XANES edge energies for the Co reference complexes match those found in the literature for similar compounds.[58] The edge energy of the as-synthesized Co MOF sample is nearly

identical to those of the corresponding Co(II) metalloporphyrin reference complexes as shown in Figure 2.9, and are unaltered by the inclusion of the weakly and strongly coordinating solvent molecules. This observation confirms that no change in oxidation state of the metal sites occurs under these guest environment conditions as expected. Only the inclusion of the oxidizing agent in the case of Co-PCN222 induces edge shifts of +5 eV (Figure 2.8), indicating the change to the Co(III) valence. With oxidation states confirmed, comparison of the Raman spectra of the Co-porphryrin systems (as illustrated in Figure 2.6) reveals that with the presence of the carboxylate functionality, in either the complex or MOF, the frequency of ν_8 becomes much less sensitive to the oxidation state of the metal. The dominance of this factor on dictating the frequency of this traditional "oxidation state marker" mode is important to note given the prevalence of carboxylate functionalized porphyrins used in MOF architectures.

Not surprisingly, the modes in the high frequency region highlighted in Figure 2.5 and Table 2.1, that undergo the biggest frequency change upon the addition of the carboxylate functionality are those localized on the phenyl groups. These modes, φ_4 and φ_5 exhibit a large increase in frequency between the TPP and TCPP versions of these complexes owing to the resonance effect of the –COOH groups. The porphyrin-localized modes in this fingerprint region traditionally demonstrate some correlation with porphyrin core size, which can be influenced by the metal ion size and strongly coupled peripheral ring functionality. The pyrrole deformation mode, ν_1 demonstrates modest sensitivity to the phenyl functionalization of both the Co and Ni porphyrin complexes, with +2 and +4 cm^{-1} frequency shift in each case respectively, upon the inclusion of the –COOH groups. This is most likely attributed to the substantial phenyl ring vibration component of this

mode. Incorporation in the MOF environment however does not appear to further influence its frequency. The other pyrrole deformation mode ν_4, which is considered a spin state marker band, does not appear to be sensitive to either the peripheral carboxylate functionalization or framework formation. While the structure sensitive mode, ν_2 is not affected by the presence of the carboxylate in NiTCPP, this mode does exhibit increased frequency between CoTPP and CoTCPP. The reason for this shift is not entirely clear. The mode frequency however, is not further altered for either of the metalloporphyrin systems upon framework formation.

2.3.2 Guest molecule interaction in metalloporphyrin MOF environments.

Analysis of the XAS results for the MOFs in comparison with those of the corresponding complexes reveals the influence of the framework on the axial interaction of the metalloporphyrin metal sites with guest species contained within the pores. With particular sensitivity to the presence and nature of axial metal ligation, the pre-edge and edge features in the XANES spectra (Figure 2.9) provide useful insights regarding the axial interaction in the metalloporphyrin MOFs compared to their respective reference complexes. For the Co porphyrin systems, the XANES spectra contain weak pre-edge features at approximately 7709 eV, attributed to the 1s→3d quadrupole allowed transitions. The relative intensity of this feature indicates the degree of centrosymmetry of the absorbing metal, with higher intensities indicating lower symmetry coordination environments of the absorbing metal. The CoTPP reference complex and activated Co-PCN222 MOF produce poorly resolved low intensity pre-edge features, reflecting their 4-coordinate metalloporphyrin environments with relatively high symmetry. Both the

pyridine and acetone-treated MOFs, Co-PCN222-py and Co-PCN222-ace yield substantially more resolved pre-edge features. This may reflect the less centrosymmetric environments of the Co sites due to mono axial ligation of the guest species (a mixture of 5 and 6 coordinate species is likely due to the pore size restrictions of the MOF) however, intensity differences are difficult to extract accurately since the pre-edge bands are partially obscured by the more intense edge feature at slightly higher energy (~7715 eV). This feature on the rising absorption edge is assigned to a metal localized 1s to 4p transition with "shakedown" contribution arising from a coupled LMCT transition.[60,61] It is commonly observed in the K-edge XANES spectra of square planar first row transition metal complexes. The feature arises from transitions with metal $4p_z$ final state character.[62] In the absence of axial coordination, the metal $4p_z$ orbital has primarly σ-nonbonding character and therefore is highly localized. Axial ligation delocalizes the orbital and the resulting changes in the valence electron shielding lead to decreased intensity of this edge feature. The square planar environments in the CoTPP reference complex and in the activated form of the Co-PCN222 MOF therefore yield prominent 1s→4p edge features. The presence of both weakly and strongly coordinating solvent guest molecules in the MOF however significantly reduce the intensity. The edge feature in the XANES spectrum of the acetone treated MOF is still resolved, but the band is almost completely absent from the pyridine treated MOF spectrum. These intensities correlate with the relative strength of the axial binding interactions with these guest molecules in the Co-porphyrin MOF environment.

Interestingly, the Ni porphryin MOF does not yield lower shakedown feature intensities (nor changes in the pre-edge) upon exposure to either acetone or pyridine. The

unchanged edge feature intensity under these conditions indicates that, in the MOF environment, these Ni-porphryrin sites are not undergoing any substantial axial interaction with weakly or strongly coordinating guests. Instead, the Ni sites retain a similar 4-coordinate geometry as the NiTPP reference molecule. This conclusion is further supported by analysis of the EXAFS spectra for the Ni porphyrin complexes and MOFs compared to those of the Co porphyrin systems (Figure 2.9). Significantly higher amplitude of the first shell peak is observed for the guest treated Co-PCN222 MOFs compared to the CoTPP reference. The analogous comparison among the Ni porphyrin MOFs and complex on the other hand does not reveal these substantial amplitude differences. While a direct correlation with coordination number is complicated by the fact that other factors such as σ^2, the mean squared disorder term, influence scattering amplitude, these results indicate that the Co porphyrin MOF under coordinating solvent environments has a higher first shell coordination number (i.e. axially interacting with guest species) than the CoTPP reference but the same axial interaction is not occurring in the Ni-PCN222 MOF.

The observed evidence for axial interaction in the Co-PCN222 is consistent with the known ligation behavior of CoTPP complexes in coordinating solvent solutions.[63] The lack of axial interaction in Ni-PCN222 however, is in stark contrast with the well-established behavior of most Ni porphyrin complexes in solution.[64,65] Double axial ligation of NiTPP occurs in strongly coordinating solvents such as pyridine.[66] Upon consideration of the lower axial binding affinity and the d-electron reorganization required to accommodate the axial ligands in Ni versus Co porphyrins, however, this contrasting behavior in the MOF environments is not that surprising. In solution, the overall binding constants of hexa-coordinate Ni(II)TPP complexes with pyridine are two orders of

magnitude lower than those for the analogous Co(II)TPP species.[63,66] Moreover, axial ligation with diamagnetic d^8 Ni(II) porphyrin systems requires electron promotion from the filled d_{z^2} to the $d_{x^2-y^2}$ orbital, which is accompanied by increased Ni-N bond lengths of the porphyrin core.[67-69] In solution this can occur readily but when the Ni-porphyrin linkers are incorporated within a MOF structure, the rigidity of the framework may severely restrict this core expansion and discourage axial ligation. On the other hand, the partially filled d_{z^2} orbital of Co(II) low spin d^7 configurations can accommodate one or two axial ligands without any d electron rearrangement (and therefore porphyrin core expansion),[69] so the rigidity imposed by the MOF structure in this case would not hinder this ligation. Additionally, a substantial distortion from planarity of the Ni-porphryin ring when in the framework structure may also be involved in preventing axial interaction behavior in the Ni-PCN222. Previous studies on substituted Ni-porphyrin complexes that remain non-planar in solution have shown extremely low axial binding affinity for bases such as pyridine or piperidine.[70] The contracted core of the ruffled porphyrin is thought to destabilize the $d_{x^2-y^2}$ orbital, making the electron promotion to this orbital needed for the σ-donating axial bond energetically unfavorable. Combined with the small triangular pore size dimension in the PCN222 structure, a rigid non-planar porphyrin geometry in the MOF structure may create a framework environment that severely hinders axial interaction with guest molecules.

Although limited in scope, some further insights on the guest molecule axial interaction (or lack thereof) in these MOF systems are afforded through analysis of the resonance Raman spectra. While direct observation of metal-axial ligand or internal axial ligand modes is precluded by the lack of resonant enhancement, some structure sensitive

modes of the porphyrin macrocycle can be altered by the presence of axial ligands, particularly when this is accompanied by a metal spin state change. For example axial ligation of Ni-porphryin complexes with nitrogeneous bases is known to alter the vibrational frequency of the spin state marker bands, ν_4 and ν_2 due to the accompanying low to high spin state change of the metal center.[64] The Raman spectra of the Ni-PCN222 systems under coordinating guest environment however show no frequency differences in these modes. This observation, while not definitive on its own, further supports the conclusion that the Ni-porphryin sites in the MOF are not participating in axial coordination under the guest environment conditions tested. The Co-PCN222 also shows no changes in these spin state sensitive vibrational modes upon inclusion of pyridine (or acetone) but this is not surprising however since a metal spin state change is not anticipated for these metalloporphyrin centers upon axial ligation.

2.4 Conclusion

In conclusion, this combined resonance Raman and X-ray absorption spectroscopy study serves to illustrate how metalloporphyrin electronic and geometric structures can be altered by incorporation as linkers in metal-organic framework architectures. The investigation of strongly and weakly coordinating guest molecule environments revealed the changes in axial binding behavior imposed by the structural constraints of the framework compared to the known behavior of similar metalloporphyrin complexes in solution. These studies provided a foundation for a subsequent project on related iron porphyrin-based MOFs by establishing spectral trends associated with porphyrin peripheral substitution and framework rigidification. Some of these findings will be detailed in Chapter 4 of this thesis.

2.5 Materials and Methods

2.5.1 Materials

Chemicals for synthesis were purchased from TCI America or Alfa Aesar. Reference porphyrin complexes CoTPP, and NiTPP (TPP = tetraphenylporphyrin) were obtained from Frontier Scientific. All chemicals were used as received unless otherwise noted. Pyridine and acetone solvents were dried over molecular sieves prior to use. The reference complexes, $CoTPP(H_2O)_2ClO_4$,[51] CoTCPP,[7] and NiTCPP[7] (where TCPP = tetrakis(4-carboxypheny)porphyrin), were synthesized according to published procedures. The precursor MeTCPP (Me=methoxy) and MOFs, M-PCN222 (where M = Co or Ni), were also made according to literature procedures.[7] $[CoTCPP(H_2O)_2]ClO_4$ was prepared by a modified procedure for $CoTPP(H_2O)_2ClO_4$.[51] The product was recrystallyzed from acetone-dichloromethane mixture. Yield: 52.7 mg, 90.8% Analysis: ESI-MS $[M^+-2(H_2O)]$ = 847.129, IR: 3469 (w), 3073 (w), 3002 (w), 1682 (s), 1606 (s), 1566 (m), 1421 (sh), 1350(m), 1313 (w), 1209 (m), 1178 (m), 1068 (s), 1004 (s), 865 (m), 786 (s), 765 (s), 727 (m) cm^{-1}. UV-Vis (DMF): 430 nm, 545 nm 592 nm.

Co-PCN222: A double scale reaction was carried out compared to the literature procedure.[7] Yield: 139 mg, 63%. Analysis: XRD, IR: 3353 (w), 2976 (w), 2924 (w), 1697 (w), 1604 (s), 1552 (s), 1415 (s), 1351(m), 1305 (w), 1209 (m), 1178 (m), 1099 (m), 1007 (s), 866 (m), 793 (s), 765 (s), 725 (m) cm^{-1}. UV-VIS diffuse reflectance λ, nm: 422, 542, 576 (sh).

Ni-PCN222: A double scale reaction was carried out compared to the literature procedure.[7] Yield: 39.2 mg, 18.9% Analysis: XRD, IR: 3342 (w), 2975 (w), 2927 (w), 1708 (m), 1604 (s), 1556 (s), 1415 (s), 1354 (m), 1305 (w), 1207 (m), 1180 (m), 1099 (m),

1002 (s), 869 (m), 800 (s), 775 (s), 715 (m) cm^{-1}. UV-VIS diffuse reflectance λ, nm: 424, 531.

M-PCN222-x (M = Co(II) or Ni(II) and x = acetone or pyridine): The as-synthesized MOF samples were soaked for 3 days in acetone then activated for 12 h at 120 ºC in the vacuum prior to treatment with other guest molecules. 50 mg of each activated MOF sample were soaked in guest molecule solvent (acetone or pyridine) for 12 hours. Each sample was again characterized by XRD to ensure the preservation of the structure.

Co(III)-PCN222ClO_4: The oxidized MOF was obtained by a modified procedure reported for the complex.[51] After soaking in acetone, Co-PCN222 (60 mg) was suspended in 60 mL methanol with an addition of 1.2 mL of 5% $HClO_4$. The mixture was left stirring overnight at room temperature. The solid was filtered out and washed with 150 mL (3x50 mL) of water. Yield: 61.2 mg. Analysis: IR: 3338 (w), 3116 (w), 3062 (w), 1697 (m), 1606 (s), 1536 (sh), 1407 (s), 1347(m), 1305 (w), 1205 (m), 1176 (m), 1070 (m), 1002 (s), 865 (m), 794 (s), 773 (s), 711 (m) cm^{-1}.UV-VIS diffuse reflectance λ, nm: 424, 531.

2.5.2 Characterization methods

Powder X-ray diffraction (XRD) patterns were recorded using Bruker D8 ADVANCE ECO Diffractometer. Full metallation of the metalloporphyrin precursors was confirmed by high resolution ESI-MS using a Bruker Daltonics Apex-ultra 70 hybrid Fourier transform mass spectrometer and UV-vis spectroscopy. Diffuse reflectance UV-vis spectra were collected using a Cary-Varian UV-visible-NIR spectrophotometer equipped with a diffuse reflectance accessory (Harrick Scientific). Samples were diluted and finely ground with KBr. Final spectra were plotted in Kubelka-Munk units and

normalized to the Soret band peak maximum for better comparison. Attenuated total reflectance infrared spectra were collected for solid samples at room temperature using Nicolette 6700 FT-IR spectrometer. Each IR spectrum was recorded as an average of 64 scans.

2.5.3 Resonance Raman spectroscopy

Raman spectra were collected using 420 nm laser excitation generated from the second harmonic of the fundamental output of a ps Ti:Sapphire laser oscillator (Tsunami, Spectra-Physics), which was pumped by a 532 nm diode pumped solid state laser (Millenia, Spectra-Physics). The Raman scattered light was collected and focused onto the slit (100μm) of a triple monochromator, and detected using a 1340×100 pixel liquid nitrogen-cooled CCD detector (Princeton Instruments). The power of the laser was attenuated to ~8 mW at the sample using neutral density filters. Samples were measured in pellet form by pressing a mixture of 20% complex or MOF with 20% of KNO_3 internal frequency standard and 60% of KBr. Samples were spun to minimize the residence time of the laser on one spot of the sample, thereby voiding heat- or photodamage of framework or complex.

2.5.4 X-ray absorption spectroscopy

X-ray absorption data were collected at the Co and Ni K-edges (7709, and 8333 eV respectively) in transmission mode at Beamline 2-2 at SSRL. The X-ray white beam was monochromatized by a Si(111) monochromator and detuned by 30% to minimize the harmonic content of the beam. Cobalt and nickel metal foils were used as references for energy calibration. The incident beam intensity (I_0) was measured by a 15 cm ionization chamber with 100% N_2 for both metal K-edges. The transmitted (I_t) and reference (I_r)

beam intensities were both measured using 30 cm ionization chambers, each with a 75% N_2 and 25% Ar gas mixture. A mixture of approximately 20 mg of the reference complexes thoroughly ground with ~100 mg of boron nitride was packed into 3 mm sealed Kapton tubes to yield approximately one X-ray absorption length. MOF samples were ground and used in the same 3mm sample tube format without additional dilution. Activated samples were packed and sealed inside a glovebox.

2.6 References

[1] J.-H. K. Chou, M. E.; Nalwa, H.S.; Rakow, N.A.; Suslick, K. S., in *The Porphyrin Handbook,* **2000**, *K. S. Kadish, K.; Guilard, R. (Ed.)*, Vol. 6, Academic Press, New York, 43-131.

[2] K. S. Suslick, P. Bhyrappa, J. H. Chou, M. E. Kosal, S. Nakagaki, D. W. Smithenry, S. R. Wilson, *Acc. Chem. Res.*, **2005**, *38*, 283-291.

[3] M. P. Byrn, C. J. Curtis, I. Goldberg, Y. Hsiou, S. I. Khan, P. A. Sawin, S. K. Tendick, C. E. Strouse, *J. Am. Chem. Soc.*, **1991**, *113*, 6549-6557.

[4] P. Dastidar, Z. Stein, I. Goldberg, C. E. Strouse, *Supramol. Chem.*, **1996**, *7*, 257-270.

[5] P. Bhyrappa, S. R. Wilson, K. S. Suslick, *J. Am. Chem. Soc.*, **1997**, *119*, 8492-8502.

[6] B. F. Abrahams, B. F. Hoskins, R. Robson, *J. Am. Chem. Soc.*, **1991**, *113*, 3606-3607.

[7] D. Feng, Z.-Y. Gu, J.-R. Li, H.-L. Jiang, Z. Wei, H.-C. Zhou, *Angew. Chem. Int. Ed.*, **2012**, *51*, 10307-10310.

[8] W. Morris, B. Volosskiy, S. Demir, F. Gándara, P. L. McGrier, H. Furukawa, D. Cascio, J. F. Stoddart, O. M. Yaghi, *Inorg. Chem.*, **2012**, *51*, 6443-6445.

[9] A. M. Shultz, O. K. Farha, J. T. Hupp, S. T. Nguyen, *J. Am. Chem. Soc.*, **2009**, *131*, 4204-4205.

[10] O. K. Farha, A. M. Shultz, A. A. Sarjeant, S. T. Nguyen, J. T. Hupp, *J. Am. Chem. Soc.*, **2011**, *133*, 5652-5655.

[11] W.-Y. Gao, M. Chrzanowski, S. Ma, *Chem. Soc. Rev.*, **2014,** 5841-5866.

[12] H. Furukawa, K. E. Cordova, M. O'Keeffe, O. M. Yaghi, *Science*, **2013**, *341*, 1230444.

[13] C. Wang, D. Liu, W. Lin, *J. Am. Chem. Soc.*, **2013**, *135*, 13222-13234.

[14] D. Feng, W.-C. Chung, Z. Wei, Z.-Y. Gu, H.-L. Jiang, Y.-P. Chen, D. J. Darensbourg, H.-C. Zhou, *J. Am. Chem. Soc.*, **2013**, *135*, 17105-17110.

[15] S. Nakagaki, G. Ferreira, G. Ucoski, K. Dias de Freitas Castro, *Molecules*, **2013**, *18*, 7279-7308.

[16] M.-H. Xie, X.-L. Yang, Y. He, J. Zhang, B. Chen, C.-D. Wu, *Chem. Eur. J.*, **2013**, *19,* 14316-14321.

[17] J. S. Anderson, A. T. Gallagher, J. A. Mason, T. D. Harris, *J. Am. Chem. Soc.*, **2014**, *136*, 16489-16492.

[18] M. Zhao, S. Ou, C.-D. Wu, *Acc. Chem. Res.*, **2014**, *47*, 1199-1207.

[19] J. W. Brown, Q. T. Nguyen, T. Otto, N. N. Jarenwattananon, S. Glöggler, L.-S. Bouchard, *Catal. Commun.*, **2015**, *59*, 50-54.

[20] Y. Chen, T. Hoang, S. Ma, *Inorg. Chem.*, **2012**, *51*, 12600-12602.

[21] P. Kucheryavy, N. Lahanas, E. Velasco, C.-J. Sun, J. V. Lockard, *J. Phys. Chem. Lett.*, **2016**, *7*, 1109-1115.

[22] J. M. Burke, J. R. Kincaid, S. Peters, R. R. Gagne, J. P. Collman, T. G. Spiro, *J. Am. Chem. Soc.*, **1978**, *100*, 6083-6088.

[23] P. G. Wright, P. Stein, J. M. Burke, T. G. Spiro, *J. Am. Chem. Soc.*, **1979**, *101*, 3531-3535.

[24] M. Kozuka, K. Nakamoto, *J. Am. Chem. Soc.*, **1981**, *103*, 2162-2168.

[25] H. Oshio, T. Ama, T. Watanabe, J. Kincaid, K. Nakamoto, *Spectrochim. Acta A*, **1984**, *40*, 863-870.

[26] T. Kitagawa, Y. Ozaki, in *Metal Complexes with Tetrapyrrole Ligands I,* **1987**, J. Buchler (Ed.), Vol. 64, Springer Berlin Heidelberg, 71-114.

[27] A. Bianconi, A. Congiu-Castellano, M. Dell'Ariccia, A. Giovannelli, P. J. Durham, E. Burattini, M. Barteri, *FEBS Lett.*, **1984**, *178*, 165-170.

[28] I. Ascone, J. Goulon, A. Bianconi, M. Tegoni, F. Labeyrie, *J. Phys. Colloques*, **1986**, *47*, C8-1143-C1148-1146.

[29] I. Ascone, A. Bianconi, E. Dartyge, S. Della Longa, A. Fontaine, M. Momenteau, *BBA-Protein Struct M*, **1987**, *915*, 168-171.

[30] H. Oyanagi, T. Iizuka, T. Matsushita, S. Saigo, R. Makino, Y. Ishimura, T. Ishiguro, *J. Phys. Soc. Jpn.*, **1987**, *56*, 3381-3388.

[31] S. Wang, G. S. Waldo, R. Fronko, J. E. Penner-Hahn, *Physica B*, **1989,** *158*, 119-120.

[32] S. Kim, I. T. Bae, M. Sandifer, P. N. Ross, R. Carr, J. Woicik, M. R. Antonio, D. A. Scherson, *J. Am. Chem. Soc.*, **1991**, *113*, 9063-9066.

[33] C. Cartier, M. Momenteau, E. Dartyge, A. Fontaine, G. Tourillon, A. Bianconi, M. Verdaguer, *BBA-Protein Struct M*, **1992**, *1119*, 169-174.

[34] C. Cartier, M. Momenteau, E. Dartyge, A. Fontaine, G. Tourillon, A. Michalowicz, M. Verdaguer, *J. Chem. Soc., Dalton Trans.*, **1992,** 609-618.

[35] S. Della Longa, A. Bianconi, I. Ascone, A. Fontaine, A. Congiu-Castellano, G. Borghini, *AIP Conf. Proc.*, **1992,** *258*, 397-408.

[36] K. A. Carrado, S. R. Wasserman, *Chem. Mater.*, **1996**, *8*, 219-225.

[37] I. T. Bae, D. A. Scherson, *J. Phys. Chem. B*, **1998**, *102,* 2519-2522.

[38] H. Yamashige, S. Matsuo, T. Kurisaki, R. C. C. Perera, H. Wakita, *Anal. Sci.*, **2005**, *21*, 309-314.

[39] P.-P. Knops-Gerrits, D. E. De Vos, E. J. P. Feijen, P. A. Jacobs, *Microporous Mater.*, **1997**, *8*, 3-17.

[40] G. Agostini, C. Lamberti, L. Palin, M. Milanesio, N. Danilina, B. Xu, M. Janousch, J. A. van Bokhoven, *J. Am. Chem. Soc.*, **2009**, *132*, 667-678.

[41] D. E. Doronkin, M. Casapu, T. Günter, O. Müller, R. Frahm, J.-D. Grunwaldt, *J Phys Chem C*, **2014,** *118*, 10204-10212.

[42] D. Grandjean, A. M. Beale, A. V. Petukhov, B. M. Weckhuysen, *J. Am. Chem. Soc.*, **2005**, *127*, 14454-14465.

[43] I. J. Drake, Y. Zhang, M. K. Gilles, C. N. Teris Liu, P. Nachimuthu, R. C. C. Perera, H. Wakita, A. T. Bell, *J. Phys. Chem. B*, **2006**, *110*, 11665-11676.

[44] G. Plazenet, E. Payen, J. Lynch, B. Rebours, *J. Phys. Chem. B*, **2002**, *106*, 7013-7028.

[45] F. Bonino, S. Chavan, J. G. Vitillo, E. Groppo, G. Agostini, C. Lamberti, P. D. C. Dietzel, C. Prestipino, S. Bordiga, *Chem. Mater.*, **2008**, *20*, 4957-4968.

[46] S. Bordiga, F. Bonino, K. P. Lillerud, C. Lamberti, *Chem. Soc. Rev.*, **2010**, *39*, 4885-4927.

[47] S. Chavan, J. G. Vitillo, E. Groppo, F. Bonino, C. Lamberti, P. D. C. Dietzel, S. Bordiga, *J Phys Chem C*, **2009**, *113*, 3292-3299.

[48] Y. Chen, J. Zhang, J. Li, J. V. Lockard, *J Phys Chem C*, **2013**, *117*, 20068-20077.

[49] C. Prestipino, L. Regli, J. G. Vitillo, F. Bonino, A. Damin, C. Lamberti, A. Zecchina, P. L. Solari, K. O. Kongshaug, S. Bordiga, *Chem. Mater.*, **2006**, *18*, 1337-1346.

[50] Y. Chen, H. Wang, J. Li, J. V. Lockard, *J. Mat. Chem. A*, **2015,** *3*, 4945-4953.

[51] H. Masuda, T. Taga, K. Osaki, H. Sugimoto, M. Mori, *Bull. Chem. Soc. Jpn.*, **1982**, *55*, 4-8.

[52] J. H. S. Green, W. Kynaston, A. S. Lindsey, *Spectrochim. Acta*, **1961**, *17*, 486-502.

[53] K. Nakamoto, *Infrared and Raman Spectra of Inorganic and Coordination Compounds, Part B*, **2009**, *6th ed., John Wiley & Sons, Inc.*

[54] M. Kozuka, M. Iwaizumi, *Bull. Chem. Soc. Jpn.*, **1983**, *56*, 3165-3166.

[55] T. S. Rush, P. M. Kozlowski, C. A. Piffat, R. Kumble, M. Z. Zgierski, T. G. Spiro, *J. Phys. Chem. B*, **2000**, *104*, 5020-5034.

[56] T. Kitagawa, M. Abe, H. Ogoshi, *J. Chem. Phys.*, **1978**, *69*, 4516-4525.

[57] T. G. L. Spiro, X.-Y. , in *Biological Application of Raman Spectroscopy,* **1998,** S. T. G. (Ed.), *Vol. 3*, Wiley, New York, 15-33.

[58] V. C. Briois, C.; Momenteau, M.; Maillard, P.; Zarembowitch, J.; Dartyge, E.; Fontaine, A.; Tourillon, G.; Thuery, P.; Verdaguer, M. , *J. Chim. Phys. Phys.- Chim. Biol.*, **1989**, *86*, 1623-1634.

[59] L. X. Chen, Z. Wang, G. Hartwich, I. Katheder, H. Scheer, A. Scherz, P. A. Montano, J. R. Norris, *Chem. Phys. Lett.*, **1995**, *234*, 437-444.

[60] S. E. Shadle, J. E. Penner-Hahn, H. J. Schugar, B. Hedman, K. O. Hodgson, E. I. Solomon, *J. Am. Chem. Soc.*, **1993,** *115*, 767-776.

[61] L. S. Kau, D. J. Spira-Solomon, J. E. Penner-Hahn, K. O. Hodgson, E. I. Solomon, *J. Am. Chem. Soc.*, **1987**, *109*, 6433-6442.

[62] T. A. Smith, J. E. Penner-Hahn, M. A. Berding, S. Doniach, K. O. Hodgson, *J. Am. Chem. Soc.*, **1985,** *107*, 5945-5955.

[63] R. D. Chapman, E. B. Fleischer, *J. Am. Chem. Soc.*, **1982**, *104*, 1575-1582.

[64] S.-L. Jia, W. Jentzen, M. Shang, X.-Z. Song, J.-G. Ma, W. R. Scheidt, J. A. Shelnutt, *Inorg. Chem.*, **1998**, *37*, 4402-4412.

[65] L. Campbell, S. Tanaka, S. Mukamel, *Chem. Phys.*, **2004**, *299*, 225-231.

[66] S. J. Cole, G. C. Curthoys, E. A. Magnusson, J. N. Phillips, *Inorg. Chem.*, **1972,** *11,* 1024-1028.

[67] H. Duval, V. Bulach, J. Fischer, R. Weiss, *Inorg. Chem.*, **1998**, *38*, 5495-5501.

[68] Y. Song, R. E. Haddad, S.-L. Jia, S. Hok, M. M. Olmstead, D. J. Nurco, N. E. Schore, J. Zhang, J.-G. Ma, K. M. Smith, S. Gazeau, J. Pécaut, J.-C. Marchon, C. J. Medforth, J. A. Shelnutt, *J. Am. Chem. Soc.*, **2005,** *127,* 1179-1192.

[69] J. K. M. Sanders, N. Bampos, Z. Clyde-Watson, S. L. Darling, J. C. Hawley, H.-J. Kim, C. C. Mak, S. J. Webb, in *The Porphyrin Handbook,* **2000,** K. S. Kadish, K.; Guilard, R. (Ed.), *Vol. 3*, Academic Press, New York, 1-40.

[70] J. A. Shelnutt, C. J. Medforth, M. D. Berber, K. M. Barkigia, K. M. Smith, *J. Am. Chem. Soc.*, **1991**, *113*, 4077-4087.

Chapter 3. Spectroscopic evidence for room temperature interaction of molecular oxygen with cobalt porphyrin linker sites within a metal-organic framework

3.1 Introduction

The interaction of molecular oxygen and other diatomic molecules with metalloporphyrin complexes has been a subject of investigation for well over half a century, often with the aim of better understanding small molecule transport and storage behavior in related heme-based protein systems.[1-2] Moreover, much of this effort has been focused on exploiting this axial binding behavior of metalloporphyrins for catalytic purposes.[3] The incorporation of these complexes as building blocks in synthetic porous solid-state networks is a common design strategy for both modeling naturally occurring metalloporphyrin cofactors in protein environments and for creating new heterogeneous catalytic materials with high densities of accessible metal reaction sites.[4-5] Metal-organic frameworks (MOFs) have recently provided a unique platform for this approach.[6-10] When metalloporphyrin units are incorporated as linkers in MOF materials, the resulting self-assembled porous crystalline architectures allow controlled access to their axial binding sites through host-guest interactions. These interactions can be further regulated by tuning the framework pore sizes and linker arrangements. Probing small molecule interactions at the metalloporphyrin sites within these materials on a molecular level is vital for both understanding and ultimately harnessing this functionality for potential catalytic purposes. The axial coordination of dioxygen with metalloporphyrin sites in an iron porphryrin-based MOF[11] and, more recently, in the isostructural cobalt porphyrin-based version,[12] was demonstrated at low temperatures using single crystal XRD and other techniques. While these studies provide strong evidence for the formation of the

oxygen bound adducts of the porphyrin-based MOFs at low temperature, it is equally important to evaluate small molecule interactions in metalloporphyrin-based frameworks at ambient or even elevated temperatures that would be more relevant for realistic catalytic conditions. Under ambient conditions, axial binding is expected to be quite weak with far too much disorder to be resolved crytallographically. Other characterization methods are therefore needed to probe these more elusive interactions.

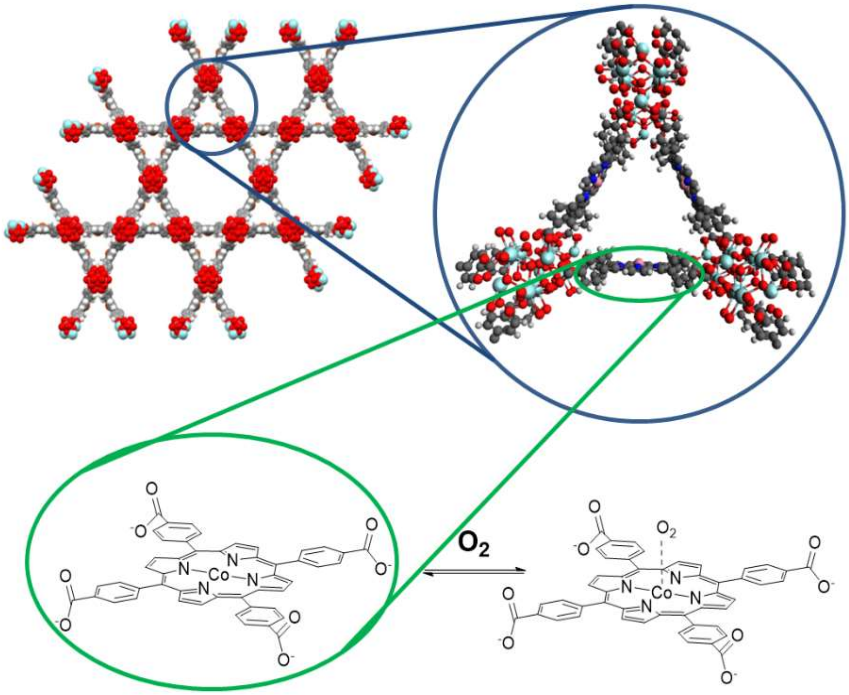

Figure 3.1 Co-PCN-222 structure with cobalt porphyrin linker site and its interaction with oxygen highlighted

Here we present the investigation of the metalloporphyrin-oxygen interactions in a cobalt porphyrin framework at room temperature using both *in situ* UV-visible diffuse reflectance (DR) and X-ray absorption spectroscopy (XAS). The specific framework

under investigation, Co-PCN-222, shown in Figure 1, is comprised of carboxyphenyl meso-substituted cobalt porphyrin linkers connected through Zr_6 nodes to produce a framework with two different pore size channels along the c-axis (diameters of ~37Å and ~10Å).[6] Chapter 2 showcased the use of DR and X-ray spectroscopy methods to probe axial interactions of both strongly and weakly coordinating guest molecules with the metalloporphyrin sites within this framework[13] Those studies revealed the influence of the framework on the axial coordination of the metalloporphyrin metal sites with the liquid phase guest species contained within the pores. In this chapter we explore the substantially weaker gas-solid interaction of Co-PCN-222 with molecular oxygen at room temperature.

3.2 Results

3.2.1 Characterization methods

Co-PCN-222 was synthesized according to published literature procedures,[6] and was characterized by powder XRD before and after activation and gas treatment processes to verify crystallinity and its retention (Figure 3.2).

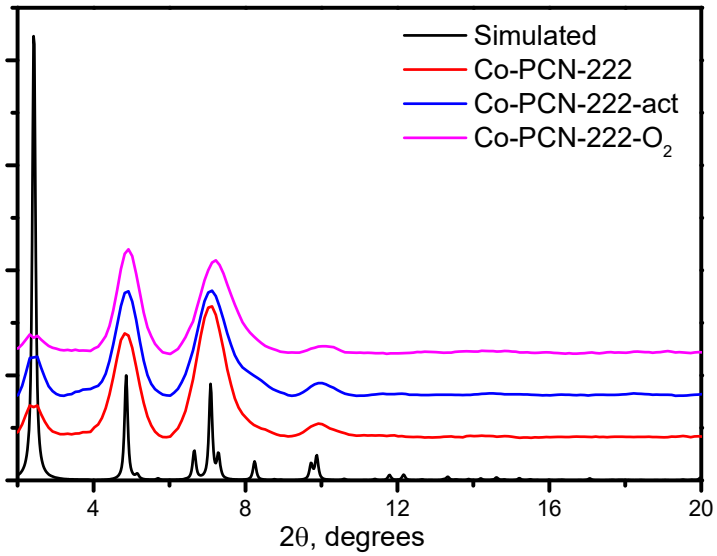

Figure 3.2 Simulated and experimental XRD pattern for Co-PCN222 samples.

Infrared spectra of the metalloporphyrin MOFs are presented and compared to the relevant reference complexes in Figure 3.3. These data were used mainly to characterize the vibrational modes and to confirm the presence of the guest molecules inside the pores of the MOF.

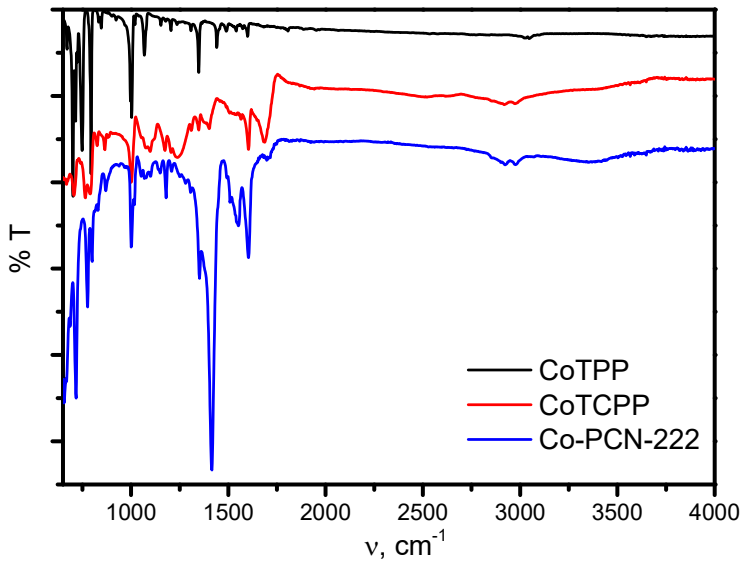

Figure 3.3 IR spectrum of Co-PCN222 samples and reference complexes

In the CoTCPP complex, the carboxylic acid stretching mode appears in the IR spectra as a strong feature in the range 1685-1691 cm^{-1}. In the MOF systems, the resulting asymmetric carboxylate modes appear at 1554-1556 $cm^{-1}$and a strong broad band around 1405 cm^{-1} is assigned to overlapping C-C aromatic stretch and symmetric -COO^- stretch peaks.[23] These carboxylate mode frequencies are consistent with the bridging type coordination with Zr in the MOF.[24]

3.2.2 UV-visible Diffuse Reflectance

CoTPP (TPP = 5,10,15,20-tetraphenylporphin) was used as a reference complex for comparison with the MOF. Using a controlled environment sample chamber, spectra of an acetone-loaded Co-PCN-222 micro-crystalline powder sample (pre-activated and then soaked in acetone prior to measurement) were collected *in situ* upon heating at 120°C under dynamic vacuum until no further spectral changes were observed and again upon subsequent cooling to room temperature and exposure to either ambient pressure (1 atm) oxygen or nitrogen gas. The final spectra collected after each step, which are dominated by porphyrin-based absorption bands, are presented in the overlay of the top graph of Figure 3.4.

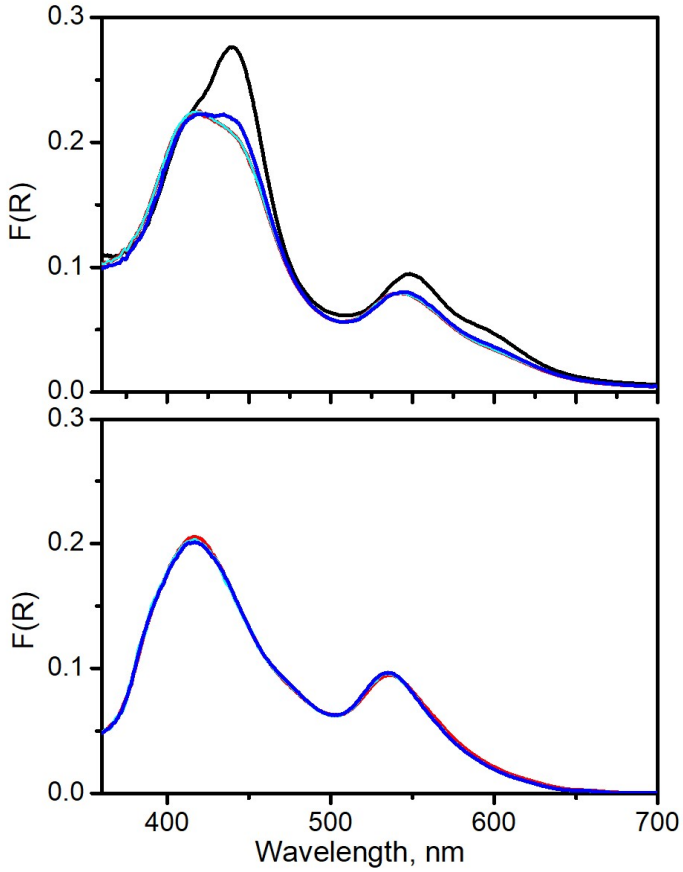

Figure 3.4 UV-VIS diffuse reflectance spectra of Co-PCN-222 MOF (top) and CoTPP reference complex (bottom) before (black) and after (red) activation under vacuum and after 15 minutes exposure to oxygen (blue) or nitrogen (cyan) gas.

The DR spectrum of acetone-soaked Co-PCN-222 has Soret and Q-band peak maxima at 439 and 548 nm that shift to 416 and 543 nm, respectively upon the vacuum assisted thermal treatment. Subsequent exposure of the activated Co-PCN-222 MOF to oxygen gas then leads to the appearance of a band in the Soret region at 438nm and a slight bathochromic shift of Q-band maximum to 546 nm. These changes were observed almost immediately, indicating rapid gas diffusion into the porous framework. No spectral changes were observed when the activated MOF was instead exposed to 1 atm N_2 gas.

3.2.3 X-ray absorption spectroscopy

Activated and O_2 treated MOF samples were prepared ex situ and sealed in 3 mm Kapton tubing under ambient pressure-controlled gas environment conditions prior to XAS measurements, while CoTPP was used without additional treatment. XAS spectra were collected at the Co K-edge (7709 eV) at room temperature. Figure 3.5 shows the XANES spectrum for the model CoTPP complex, the activated framework, and the oxygen exposed MOF.

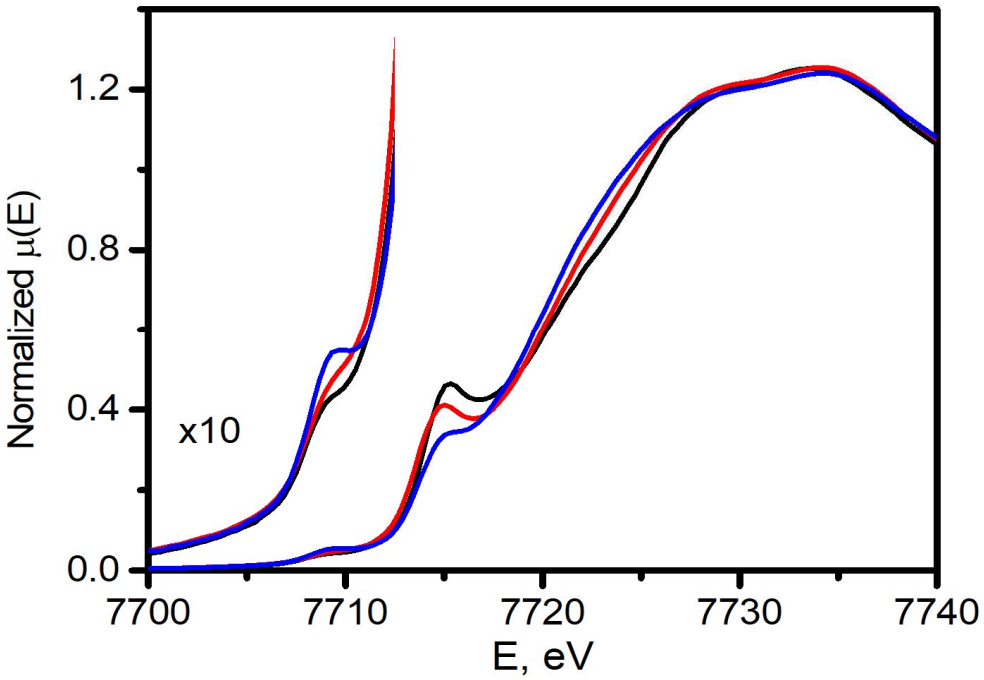

Figure 3.5 Co K-edge XANES spectra of CoTPP (black), Co-PCN-222-act (red), andCo-PCN-222-O2 (blue).

These spectra each contain a pre-edge feature at 7709 eV, which corresponds to a 1s→3d transition,[19-20] and an additional edge feature around 7715 eV, attributed to a 1s→4p + LMCT shakedown transition.[21]

3.3 Discussion

3.3.1 UV-visible Diffuse Reflectance

The observed DR spectral differences, particularly in the Soret band region, reflect the cobalt porphyrin coordination environments associated with the changes in guest molecule composition of the pores. The Soret and Q-band peak values for the framework in the absence of any axially interacting species (i.e. under activation conditions or N_2 gas environment) are similar to those measured for the square planar CoTPP reference complex (Figure 3.4, bottom), reflecting the comparable four-coordinate environments of the two cobalt porphyrin systems. Axial coordination of cobalt(II) porphyrins with π-acceptor ligands has been reported to shift the Soret and Q-band to lower energies due to the accompanying orbital energy perturbations.[15-16] The acetone loaded initial framework follows this spectral trend, indicating that the weakly coordinating solvent interacts with the Co-porphryin sites in the MOF. Similarly, the appearance of the lower energy feature in the Soret band region and slight red shift of the Q-band for Co-PCN-222 exposed to molecular oxygen after activation points to weak interaction of O_2 with the pore wall-facing open cobalt sites at room temperature. Similar spectral changes were notably reported for CoTPP compared with the CoTPP·O_2 complex in toluene glass solutions (77 K).[15]

The relatively weak O_2 interaction with the cobalt porphryin sites in the MOF showed high reversibility as the diffuse reflectance spectrum exhibits a complete return to that of the activated Co-PCN222 framework upon vacuum removal of the O_2 environment. DR spectra measured for the CoTPP reference complex in the solid state displayed almost no change upon identical *in situ* activation and oxygen treatments

(Figure 3.4, bottom), indicating negligible interaction of the cobalt sites with the O_2 gas. As expected, this solid state cobalt porphyrin environment, unlike that of the MOF, does not provide the porous structure needed to afford access to the metalloporphyrin sites through host-guest interactions. This comparison also shows that the DR changes in the Co-PCN-222 spectra are not just indicating interactions of the cobalt porphyrin sites located on the surface of the MOF particles.

3.3.2 X-ray absorption spectroscopy

Further evidence that O_2 guest molecules are interacting specifically with the cobalt sites within the MOF at room temperature is provided by X-ray absorption spectroscopy. Soft X-rays have been applied to study gas molecule binding at open metal sites in MOF materials.[17-18] This energy range may be useful for probing the structure sensitive Co L-edges in the current framework upon O_2 interaction at very low pressures but hard X-ray spectroscopy at the Co K-edge is more compatible with the desired ambient pressure oxygen gas environment. The relative intensities of the pre-edge and edge features vary with each system and reflect the local coordination geometry of the Co sites in each case. The low intensity of the quadrupole allowed 1s→3d peak for CoTPP reflects the relatively high degree of centrosymmetry produced by its approximate D_{4h} symmetry, even in the presence of oxygen. Moreover, the 1s→4p + LMCT edge feature is observed with significant intensity. This feature, common to metal coordination complexes with square planar geometries, arises from transitions with metal $4p_z$ final state character.[22] The similarities of the Co-PCN-222-act XANES spectrum (i.e. weakly resolved 1s→3d feature and more pronounced 1s→4p transition) indicate a similar 4-coordinate porphyrin

geometry without any axially interactions. The oxygen-exposed MOF, Co-PCN-222-O_2 however produces a spectrum with increased intensity of the pre-edge peak and substantially decreased intensity of the shakedown feature. These observations are in line with the changes in metal 3d-ligand 4p orbital mixing expected upon axial ligation. The higher intensity of the former peak is attributed to increased dipole allowed character of the 1s→3d transition and the reduced intensity of the latter feature signals a reduction in pure metal $4p_z$ character. Together these changes indicate a lower symmetry environment of the Co sites accompanying mono axial (z-axis) interaction with oxygen.

The electronic consequences of these weak Co-O_2 interactions are quite different than those associated with the more formally bound species that can only be obtained at low temperatures. Recent crystallographic and EPR measurements of a similar cobalt porphyrin-based MOF under ambient pressure oxygen environment at cryogenic temperatures strongly point to the formation of a Co(III) superoxide species upon oxygen binding.[12] In this study, the O_2 binding behavior observed for the MOF at room temperature however, indicates no accompanying oxidation state changes. The edge energy shift of the Co-PCN-222-O_2 XANES spectrum is unchanged relative to those of the activated MOF and Co(II)TPP reference, illustrated by the XANES derivative spectra in Figure 3.6, indicating that the cobalt sites remain in the +2 oxidation state upon weak oxygen interaction at room temperature.

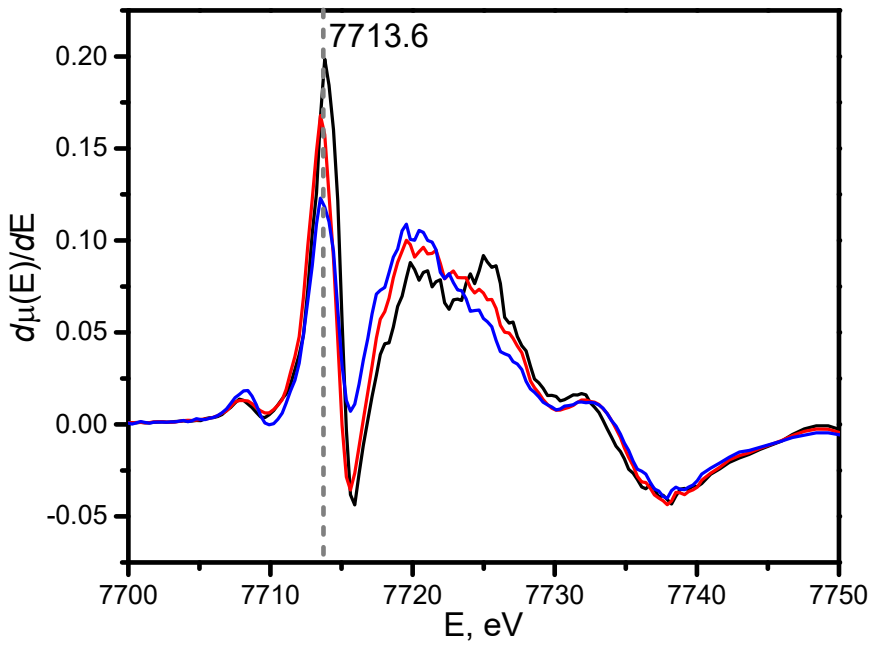

Figure 3.6 Derivative of XANES spectra for CoTPP (black), Co-PCN-222-act (red), and Co-PCN-222-O_2 (blue)

3.4 Conclusion

In conclusion, both optical diffuse reflectance and XANES spectroscopy were used to investigate a cobalt porphyrin-based MOF under oxygen gas environment. Compared to the CoTPP solid state reference, increased access to the Co(II) sites afforded by the porous framework in the MOF is the driving factor that enables Co-O_2 interaction. These measurements revealed that weak interactions between the open metalloporphyrin sites of the framework and the O_2 molecules contained within the pores occur even under ambient conditions but are not strong enough to induce an oxidation state change of the Co-metal center. Moreover, this work illustrates that these electronic and structurally sensitive methods can be used as *in situ* probes for the weak host-guest interactions

associated with intermediate species during catalytic reactions within these porous materials.

3.5 Materials and methods

3.5.1 Materials

All starting materials for synthesis were purchased from TCI America or Alfa Aesar. The CoTPP porphyrin reference complex was obtained from Frontier Scientific.

Co-PCN222: A double scale reaction was carried out compared to the literature procedure.[1] Yield: 139 mg, 63%. Analysis: XRD (Figure S1), IR (Figure S2): 3353 (w), 2976 (w), 2924 (w), 1697 (w), 1604 (s), 1552 (s), 1415 (s), 1351(m), 1305 (w), 1209 (m), 1178 (m), 1099 (m), 1007 (s), 866 (m), 793 (s), 765 (s), 725 (m) cm^{-1}. UV-VIS diffuse reflectance λ, nm: 422, 542, 576 (sh). Activated sample was prepared by soaking the as synthesized Co-PCN-222 in acetone followed by heating in the vacuum at 120 °C for 12 h in a Schlenk tube.

3.5.2 Characterization

Powder X-ray diffraction (XRD) patterns were recorded using Bruker APEX II diffractometer equipped with a 4K CCD detector and Cu Kα X-ray tube. Full metallation of the metalloporphyrin precursors was confirmed by high resolution ESI-MS using a Bruker Daltonics Apex-ultra 70 hybrid Fourier transform mass spectrometer and UV-vis spectroscopy. Diffuse reflectance UV-vis spectra were collected using a Cary-Varian UV-visible-NIR spectrophotometer equipped with a diffuse reflectance accessory (Harrick

Scientific). Samples were diluted and finely ground with KBr. Final spectra were plotted in Kubelka-Munk units.

3.5.3 In-situ diffuse reflectance

In situ diffuse reflectance experiments were carried out on the UV-vis setup described above using a controlled environment reaction chamber (Harrick Scientific). KBr-diluted Co-PCN-222 sample was heated to 120 °C under dynamic vacuum and held under these conditions for 6 hours. The activation process was monitored by DR spectroscopy. Once no additional spectral changes were observed, the sample was cooled to room temperature for subsequent gas treatment. Spectra were recorded at room temperature in the vacuum, and upon exposure to 1 atm of either nitrogen or oxygen gas environment. Spectra were again recorded 15 minutes after gas treatments.

3.5.4 X-ray absorption spectroscopy

X-ray absorption data were collected at the Co K-edge (7709 eV) in transmission mode at Beamline 2-2 at SSRL. The X-ray white beam was monochromatized by a Si(111) monochromator and detuned by 30% to minimize the harmonic content of the beam. Cobalt metal foil was used as reference for energy calibration. The incident beam intensity (I_0) was measured by a 15 cm ionization chamber with 100% N_2 for both metal K-edges. The transmitted (I_t) and reference (I_r) beam intensities were both measured using 30 cm ionization chambers, each with a 75% N_2 and 25% Ar gas mixture. A mixture of approximately 20 mg of the CoTPP reference complex thoroughly ground with ~100 mg of boron nitride was packed and sealed in 3 mm Kapton tubes to yield approximately one

X-ray absorption length. MOF samples were ground and packed in the same 3mm sample tube format without any dilution. The activated MOF sample was packed and sealed inside a glovebox. For the oxygen loaded MOF sample, Co-PCN222-O_2, a portion of the activated MOF sample was packed in a 3-mm sample tube and removed from the glovebox in the schlenk flask and exposed to 100% oxygen gas environment for three days. The sample was subsequently sealed inside the tube prior to removal from the schlenk line.

3.6 References

[1] Momenteau, M.; Reed, C. A., *Chem. Rev.* **1994,** *94*, 659-698.

[2] Kadish, K. M.; Smith, K. M.; Guilard, R., *The Porphyrin Handbook*. Academic Press: 1999; Vol. 4.

[3] Meunier, B., *Chem. Rev.* **1992,** *92*, 1411-1456.

[4] Chou, J.-H. K., M. E.; Nalwa, H.S.; Rakow, N.A.; Suslick, K. S., In *The Porphyrin Handbook*, Kadish, K.; Smith, K.; Guilard, R., Ed. Academic Press: New York, 2000; Vol. 6, pp 43-131.

[5] Suslick, K. S.; Bhyrappa, P.; Chou, J. H.; Kosal, M. E.; Nakagaki, S.; Smithenry, D. W.; Wilson, S. R., *Acc. Chem. Res.* **2005,** *38*, 283-291.

[6] Feng, D.; Gu, Z.-Y.; Li, J.-R.; Jiang, H.-L.; Wei, Z.; Zhou, H.-C., *Angew. Chem. Int. Ed.* **2012,** *51*, 10307-10310.

[7] Morris, W.; Volosskiy, B.; Demir, S.; Gándara, F.; McGrier, P. L.; Furukawa, H.; Cascio, D.; Stoddart, J. F.; Yaghi, O. M., *Inorg. Chem.* **2012,** *51*, 6443-6445.

[8] Shultz, A. M.; Farha, O. K.; Hupp, J. T.; Nguyen, S. T., *J. Am. Chem. Soc.* **2009,** *131*, 4204-4205.

[9] Farha, O. K.; Shultz, A. M.; Sarjeant, A. A.; Nguyen, S. T.; Hupp, J. T., *J. Am. Chem. Soc.* **2011,** *133*, 5652-5655.

[10] Gao, W.-Y.; Chrzanowski, M.; Ma, S.; Metal-Metalloporphyrin Frameworks: A Resurging Class of Functional Materials. *Chem. Soc. Rev.* **2014,** *43*, 5841-5866.

[11] Anderson, J. S.; Gallagher, A. T.; Mason, J. A.; Harris, T. D., *J. Am. Chem. Soc.* **2014,** *136*, 16489-16492.

[12] Gallagher, A. T.; Kelty, M. L.; Park, J. G.; Anderson, J. S.; Mason, J. A.; Walsh, J. P. S.; Collins, S. L.; Harris, T. D., *Inorganic Chemistry Frontiers* **2016,** *3*, 536-540.

[13] Kucheryavy, P.; Lahanas, N.; Lockard, J. V., *J. Coord. Chem.* **2016,** *69*, 1780-1791.

[14] Kucheryavy, P.; Lahanas, N.; Velasco, E.; Sun, C.-J.; Lockard, J. V., *J. Phys. Chem. Lett.* **2016,** *7*, 1109-1115.

[15] Wayland, B. B.; Minkiewixz, J. V.; Abd-Elmageed, M. E., *J. Am. Chem. Soc.* **1974,** *96*, 2795-2801.

[16] Gouterman, M., In *The Porphyrins*, Dolphin, David, Ed. Academic Press, Inc.: New York, 1978; Vol. III.

[17] Drisdell, W. S.; Poloni, R.; McDonald, T. M.; Long, J. R.; Smit, B.; Neaton, J. B.; Prendergast, D.; Kortright, J. B., *J. Am. Chem. Soc.* **2013,** *135*, 18183-18190.

[18] Drisdell, W. S.; Poloni, R.; McDonald, T. M.; Pascal, T. A.; Wan, L. F.; Pemmaraju, C. D.; Vlaisavljevich, B.; Odoh, S. O.; Neaton, J. B.; Long, J. R.; Prendergast, D.; Kortright, J. B., *Phys. Chem. Chem. Phys.* **2015,** *17*, 21448-21457.

[19] Briois, V. C., C.; Momenteau, M.; Maillard, P.; Zarembowitch, J.; Dartyge, E.; Fontaine, A.; Tourillon, G.; Thuery, P.; Verdaguer, M., *J. Chim. Phys. Phys.- Chim. Biol.* **1989,** *86*, 1623-1634.

[20] Srivastava, U. C.; Nigam, H. L., *Coord. Chem. Rev.* **1973,** *9*, 275-310.

[21] Shadle, S. E.; Penner-Hahn, J. E.; Schugar, H. J.; Hedman, B.; Hodgson, K. O.; Solomon, E. I., *J. Am. Chem. Soc.* **1993,** *115*, 767-776.

[22] Smith, T. A.; Penner-Hahn, J. E.; Berding, M. A.; Doniach, S.; Hodgson, K. O.; *J. Am. Chem. Soc.* **1985,** *107*, 5945-5955.

[23] J. H. S. Green, W. Kynaston, A. S. Lindsey, *Spectrochim. Acta*, **1961**, *17*, 486-502.

[24] K. Nakamoto, *Infrared and Raman Spectra of Inorganic and Coordination Compounds*, *Part B*, 6th ed., John Wiley & Sons, Inc, **2009.**

Chapter 4. Spectroscopic evidence of pore geometry effect on axial coordination of guest molecules in metalloporphyrin-based metal-organic frameworks

4.1 Introduction

Metalloporphyrins in native protein environments play essential roles in small molecule activation and catalysis. Incorporation of these organometallic macrocycles in synthetic porous solid state matrixes offers an intriguing way of generating artificial systems imparted with this type of functionality.[1–3] Metalloporphyrin-based metal−organic frameworks (MOFs) are one emerging class of such materials. These porous self-assembled 3D networks are composed of metal ions or clusters connected through coordination bonds with metalloporphyrin linker molecules and exhibit permanent microporosity upon solvent removal.[3–13] Consequently, their robust structures offer potentially unhindered guest species access to the porphyrin metal centers that make up the pore walls while preventing the undesirable dimerization deactivation pathways that would inevitably occur in solution.[14] Several porphyrin-based MOFs have demonstrated high stability and catalytic activity with respect to various substrates for reactions such as olefin epoxidation and biomimetic oxidation.[5,8,9,15] Understanding the mechanism of these reactions, in particular the role of the MOF structure, in terms of pore size and shape restrictions, is important for their continued development as potential single site catalysts. Metalloporphyrin reactivity depends on the axial coordination accessibility, spin, and oxidation state of the metal center. Thus, in a MOF environment, framework influence on these properties becomes an important parameter for controlling the reactions within these materials. In this fundamental study, we focus on a series of

MOFs composed of Zr-oxo cluster nodes and iron porphyrin linkers, which serves as a convenient platform for exploring framework imposed structural restrictions on substrate binding and reactivity. The two frameworks under investigation, PCN222[4–6] and PCN224,[7] have similar composition but quite dissimilar pore structures, as shown in Figure 4.1.

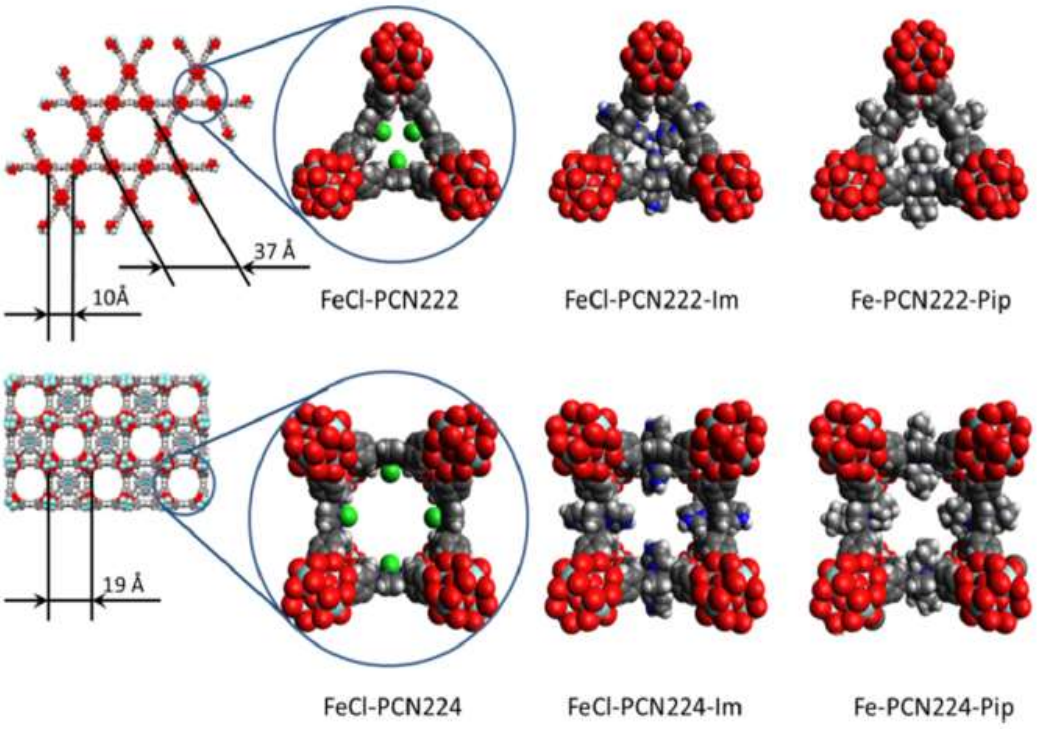

Figure 4.1 Pore structure and dimensions of FeCl-PCN222 (top) and FeCl-PCN224 (bottom) MOFs. Space-filling models of magnified pore regions illustrate the predicted binding patterns of the metalloporphyrin linker sites with axially coordinating guests: imidazole (FeCl-PCN222-Im, FeCl- PCN224-Im) and piperidine (Fe-PCN222-Pip, Fe-PCN224-Pip).

While PCN222 has two types of 1D pores with drastically different shapes and dimensions (hexagonal versus trigonal channels with spans of ~37 Å and ~10 Å, respectively), PCN224 has only intermediate sized cubic pores (~19 Å diameter). These two types of pore environments impose different restrictions on axial binding and

therefore the reactivity of the metalloporphyrin linkers. This chapter covers an investigation of the pore size restrictions and host−guest interactions in both Fe-PCN222 and Fe-PCN224 upon introduction of selected guest molecules (acetone, imidazole, or piperidine) that differ in size, binding affinity, and reactivity. Though acetone is a comparatively noninteracting guest, imidazole and piperidine are coordinating species with iron porphyrins, according to well-established literature precedent for analogous metalloporphyrins in other environments.[17−20] Moreover, piperidine serves as a reducing ligand in this context, but imidazole is expected to exhibit nonreductive coordination with the iron centers. Given the pore dimensions of the two frameworks, the size of these guest molecules is also a factor affecting the extent of axial coordination at the iron sites. Spacefilling models (Figure 4.1) indicate that imidazole is small enough for accommodation within the pores at both axial coordination sites of the iron porphyrin linkers in both frameworks. Piperidine is significantly more bulky compared to imidazole (48$Å^3$/molecule vs 80$Å^3$/molecule, respectively). The small pores of the PCN222 framework are spatially limited and consequently, should restrict piperidine dual coordination to only one out of the three Fe porphyrin linkers. The uniform pore size of PCN224, however, affords equal access to both axial coordination sites and, as the space-filling model suggests, is theoretically large enough to accommodate full axial coordination of piperidine at the metal centers. The axial interaction patterns between guest molecules and porphyrin linkers of these frameworks cannot be evaluated on the molecular level using macroscale characterization techniques such as gas sorption measurements. Here, we use a combination of optical diffuse reflectance (DR), Raman, X-ray absorption (XAS), and X-ray emission (XES) spectroscopies to probe the guest

molecule interactions with the iron centers in the two MOF environments. Optical,[19,21,22] vibrational,[23–27] and Fe K-edge X-ray absorption[28–30] spectroscopic signatures of other iron porphyrin-containing systems are well established and thus provide convenient points of reference for the porphyrin-based MOF systems investigated here. Differences among the Soret and Q-bands in optical DR spectra, the oxidation and spin state marker modes in the Raman spectra, and the shape and intensity of the 1s → 3d pre-edge features of XANES spectra together yield a qualitative picture of the local coordination geometry, oxidation, and spin state changes experienced by the iron sites upon interaction with the different guest species. To gain quantitative insights regarding the relative contributions of different Fe coordination and electronic structure environments in these frameworks, we turn to a complementary X-ray emission spectroscopy technique. On account of its particular sensitivity to the number of unpaired d electrons,[31–33] mainline Kβ non-resonant X-ray emission spectroscopy provides a route for evaluating the extent of axial interaction since different coordination scenarios result in different oxidation/spin states of the metal centers. Furthermore, quantitative spin state information can be obtained from XES spectra through line shape analysis methods (e.g., integrated absolute difference (IAD) analysis),[34–36] which have proved useful for the assessment of mixed spin environments in other systems.[37–39] Applied to the Fe porphyrin-based MOF systems, these quantitative measures verify the overall trends in axial coordination predicted by the space-filling diagrams, but reveal important deviations from the simple model for some guest species/framework combinations. These coordination discrepancies along with potential explanations will be discussed in detail.

4.2 Results

4.2.1 Synthesis and Characterization

The high-spin (HS) Fe(III) MOFs, FeCl-PCN222 and FeCl-PCN224, were treated, after activation, with the target guest species: acetone, imidazole, or piperidine to modify the iron porphyrin linker sites. The inclusion of acetone within the framework pores is not expected to alter the axial coordination, oxidation, or spin state of the iron sites. FeCl-PCN222-ace and FeCl-PCN224-ace each retain the HS Fe(III) status with an axially coordinated chloride ligand, similar to FeClTPP, which is used as a reference complex. The imidazole-loaded frameworks, FeCl-PCN222-Im and FeCl-PCN224-Im, are expected to generate iron porphyrin linker sites analogous to the reference complex $FeTPPIm_2Cl$, which contains low-spin (LS) Fe(III) sites with two axially bound imidazole ligands. In these modified frameworks, the chloride ions are no longer directly coordinated to the iron sites but are likely located within the pores, closely associated with the iron sites as outer sphere counterions for charge balance as in the case of $FeTPPIm_2Cl$. Upon piperidine treatment, the iron sites of the resulting modified MOFs, Fe-PCN222-Pip and Fe-PCN224-Pip, undergo reduction to Fe(II) and contain mixtures of HS pentacoordinated and LS hexacoordinated environments as discussed in detail below in comparison with the hexacoordinated Fe(II) reference complexes, $FeTPPPip_2$ and $FeTPPPy_2$. The displaced chloride ions in these modified MOFs are most likely trapped within the pores as piperidinum salt counterions that form as a byproduct of the reduction reaction. MOF crystallinity and its preservation upon activation and guest molecule treatments were confirmed by PXRD characterization (Figure 4.2).

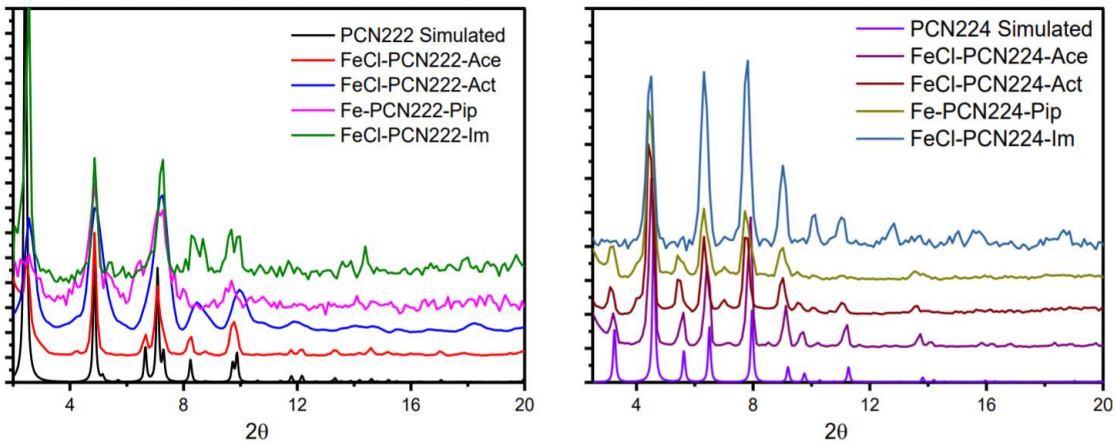

Figure 4.2 Powder XRD patterns for PCN-222 samples (left) and PCN224 (right)

Infrared absorption spectroscopy verified the presence of the guest molecules in the pores (Figure 4.3). Acetone-treated MOF samples have a medium intensity peak at 1702 cm^{-1}, indicating the presence of the carbonyl group. The other acetone peaks severely overlap with the MOF vibrational modes and therefore cannot be used for verification. IR peaks, clearly attributed to imidazole, in the spectra of both FeCl-PCN222-Im and FeCl-PCN224-Im appear at 3122, 2925, 2703, 1326, 1253, and 1139 cm^{-1}. The other imidazole related modes overlap with ones attributed to the framework. The presence of piperidine in the pores in Fe-PCN222-Pip and Fe-PCN224-Pip was also confirmed by IR. Corresponding peaks appear at the aliphatic C-H stretch region at 2937 and 2855 cm^{-1} as well as in the fingerprint region at 1280 and 1257 cm^{-1}. Porphyrin localized structure-sensitive vibrational modes, Band I and Band II,[25] also occur in the fingerprint region, but their overlap with carboxylate and guest vibrational modes complicates the assignment and evaluation as oxidation and spin markers.

4.2.2 UV-visible diffuse reflectance

The UV−vis DR spectra of the PCN22X MOFs and corresponding reference complexes are presented in Figure 4.4. The Soret and Q-band absorption maxima of the reference complex spectra are fully consistent with literature data[22] and are similar both in solid state and in solution (Figure 4.5 a,b). The acetone-treated MOFs, FeCl-PCN222-ace and FeCl-PCN224-ace, exhibit very similar DR spectra to that of the FeClTPP reference complex. Their Soret band maxima are found in the region 432−435 nm, along with Q-bands with maxima at 515, 580, and 691 nm. In situ activation for 3 h at 120 °C did not reveal any significant changes in band position or intensity (Figure 4.5c). The spectra of the imidazole- and piperidine-treated MOFs also closely follow the spectral trends of the corresponding reference complexes. $FeTPPIm_2Cl$ as well as FeCl-PCN222-Im and FeCl-PCN224-Im have the simplest spectra: for the MOFs, maxima of Soret bands are around 425 nm while a single resolved Q-band is observed in each case at 555 nm. These peak maxima are similar to those of the reference complex with maxima at 429 and 552 nm, respectively. Piperidine-treated MOFs have Soret band maxima around 420 nm, and three resolved Q-bands with maxima around 531, 570, and 615 nm, which compare with the Soret and Q-band maxima of the $FeTPPPip_2$ reference spectrum at 431, 531, 563, and 612 nm, respectively.

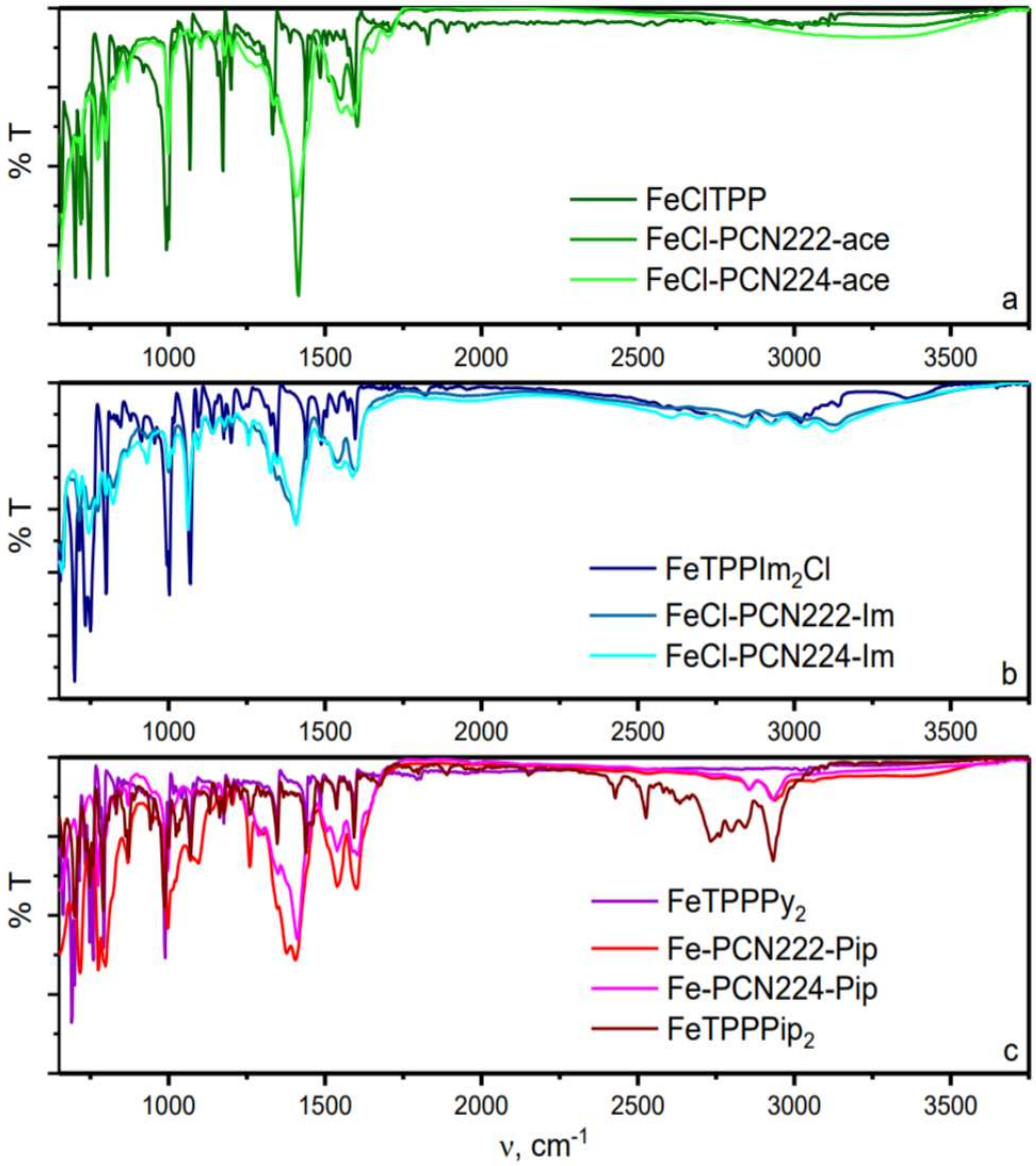

Figure 4.3 FTIR spectra of (a) MOFs treated acetone and FeClTPP, (b) MOFs treated with imidazole and $FeTPPIm_2Cl$ (c) MOFs treated with piperidine, $FeTPPPip_2$ and $FeTPPPy_2$.

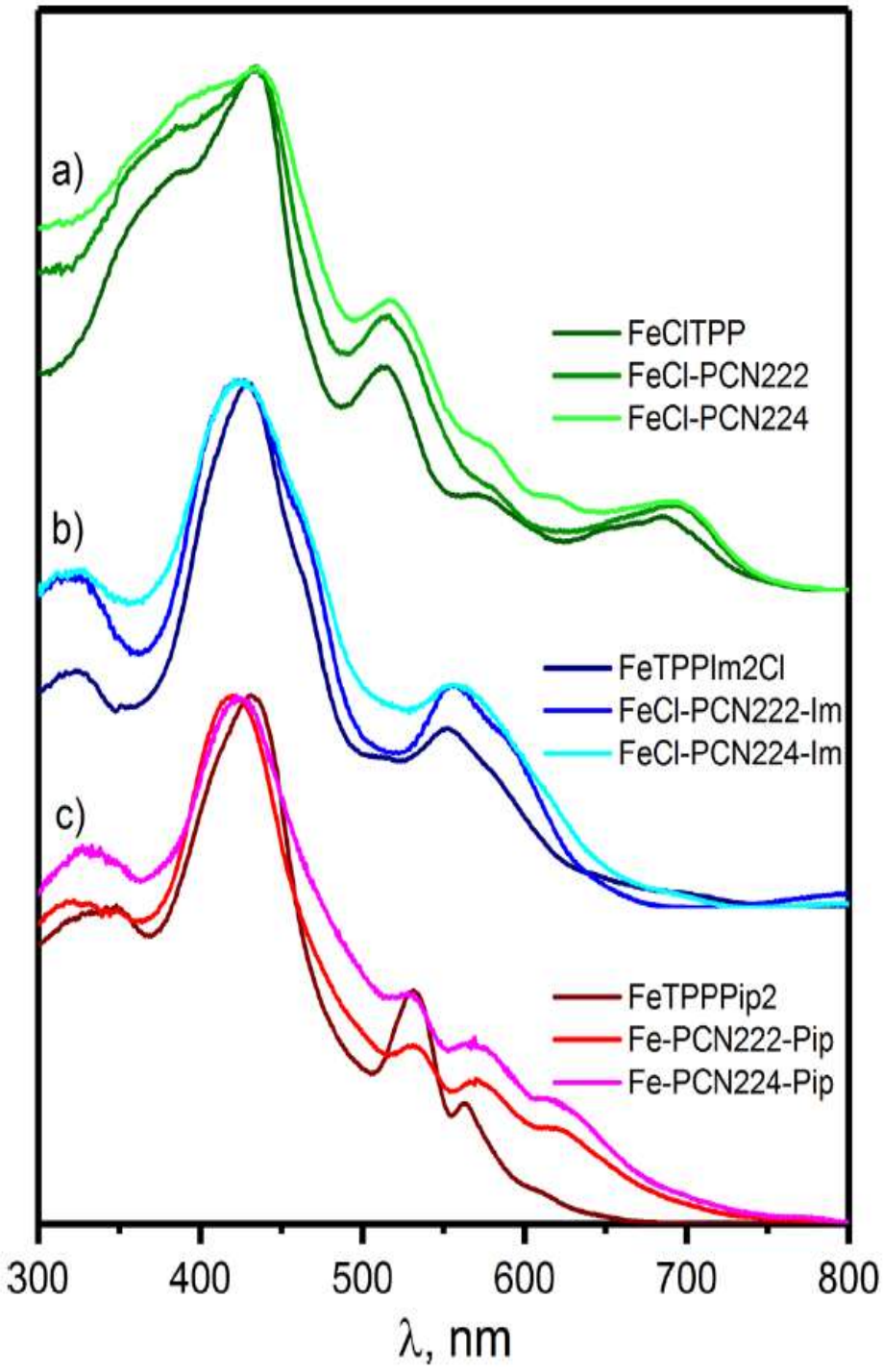

Figure 4.4 Diffuse reflectance spectra of (a) FeClTPP, FeCl-PCN222-ace, and FeCl-PCN224-ace; (b) $FeTPPIm_2Cl$, FeCl PCN222-Im, and FeCl-PCN224-Im; and (c) $FeTPPPip_2$, Fe-PCN222-Pip, and Fe-PCN224-Pip.

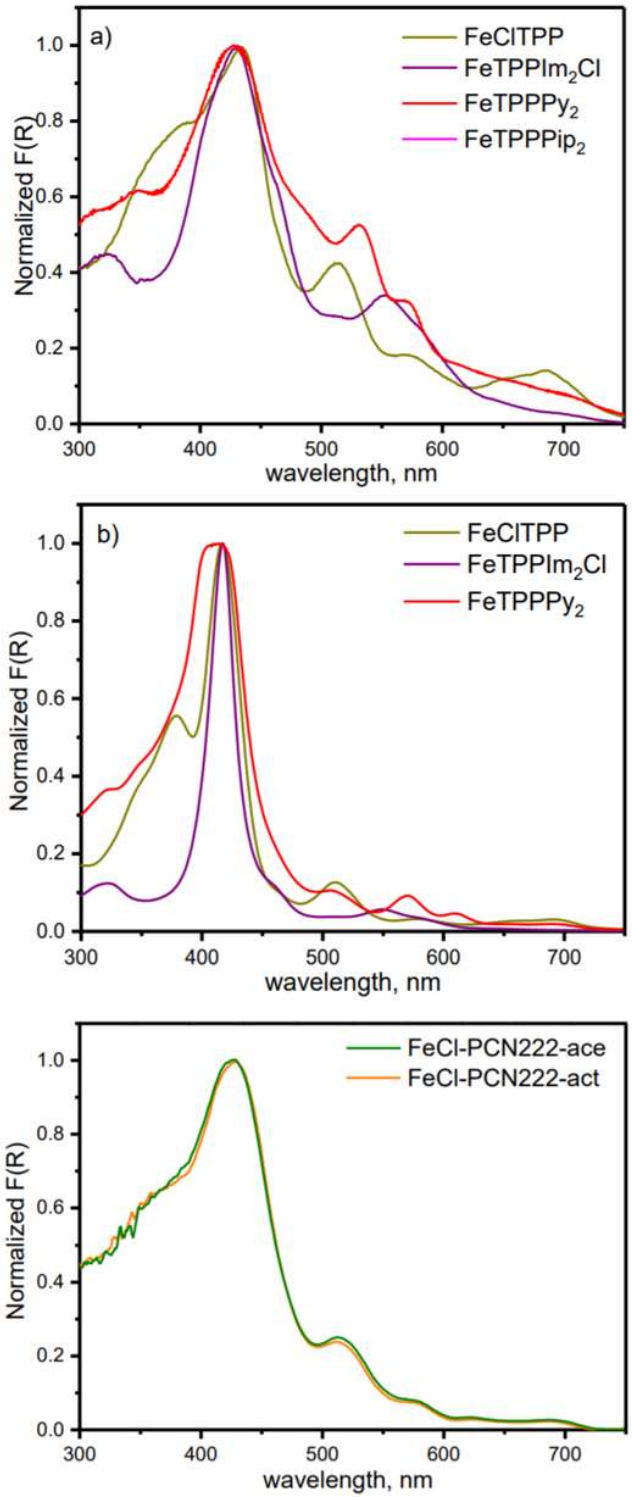

Figure 4.5 a) UV-Vis diffuse reflectance spectra of iron porphyrin reference complexes in solid state, b) UV-VIS spectra of reference complexes in DMF for Fe(III) porphyrins and for Fe(II) porphyrin recorded in an air-free quartz cell in dichloromethane – pyridine mixture, c) UV-Vis Diffuse reflectance of acetone treated and activated FeCl-PCN222 sample.

4.2.3 Resonance Raman spectroscopy

The resonance Raman spectra measured for the two MOF systems under different guest environments are shown along with the relevant iron porphyrin reference complexes in Figure 4.6. Here we highlight the important skeletal porphyrin modes that are sensitive to the metal ion size and, therefore, the oxidation and spin state of the metal center.[24]

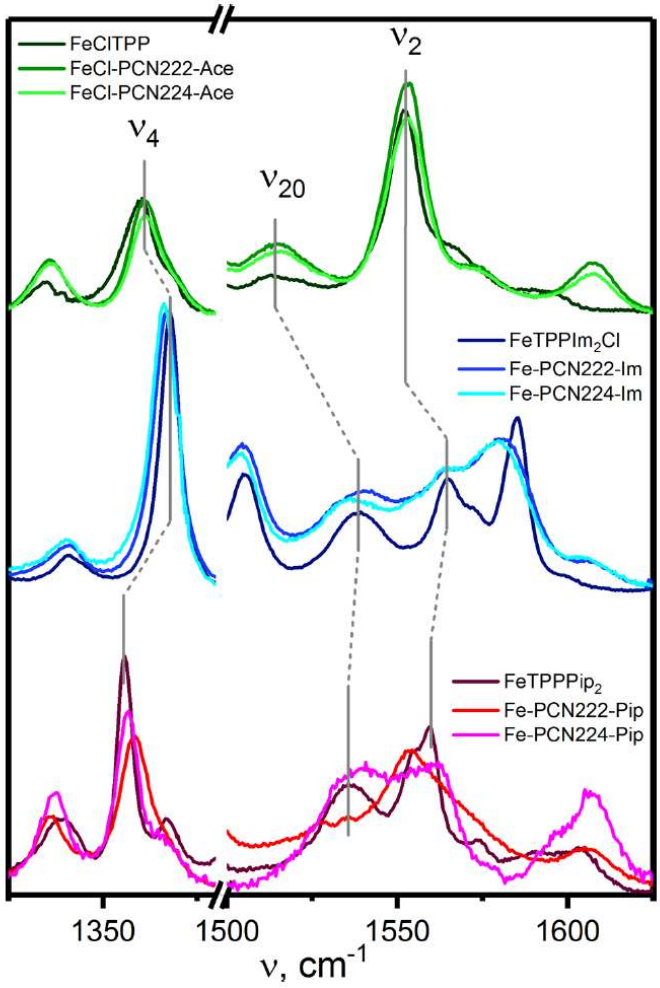

Figure 4.6 Raman spectra (highlighting oxidation and spin marker band regions) of reference complexes FeClTPP, FeTPPIm2Cl, FeTPPPip2, and MOFs treated with acetone, imidazole, and piperidine.

Table 4.1 contains a summary of frequencies of these relevant structure-sensitive modes. Notably omitted from our comparisons is the core breathing mode, ν_8, which

occurs in the range of 380 cm^{-1} and is known as an oxidation state marker mode in other metalloporphyrin systems.[25] In MOF environments, however, this mode becomes significantly less sensitive to the oxidation state of the metal center, as discussed in chapter 2.[43] For this reason, we only focus on ν_4, another porphyrin marker mode assigned to a pyrrole deformation mode,[24,27] which we found retains its acute sensitivity to metal oxidation and spin state even within the MOF environment. Porphyrin core C-C stretching modes, ν_2 and ν_{20}, are also highlighted as they have been found to maintain their spin state sensitivity in MOF environments as well.

Table 4.1 Structure-Sensitive Raman Modes for Reference Complexes FeClTPP, $FeTPPIm_2Cl$, $FeTPPPip_2$, and MOFs Treated with Acetone, Imidazole, and Piperidine[a]

	ν_4 (cm^{-1})	ν_{20} (cm^{-1})	ν_2 (cm^{-1})
FeClTPP	1360.1	1511.7	1553.7
FeCl-PCN222-ace	1360.9	1515.1	1553.6
FeCl-PCN224-ace	1361.0	1515.9	1553.4
$FeTPPIm_2Cl$	1367.3	1538.5	1564.8
FeCl-PCN222-Im	1366.4	1534.9	1565.2
FeCl-PCN224-Im	1366.3	1536.5	1564.8
$FeTPPPip_2$	1355.4	1536.9	1560.7
Fe-PCN222-Pip	1358.5	1535.6/1527.6	1554.3
Fe-PCN224-Pip	1356.7	1538.2	1560.1

[a]Vibrational mode indexing based on the assignments established in refs 24 and 44.

All of these core-localized modes (in terms of frequency and resonance intensity enhancement patterns upon excitation into the Q-band region of their absorption spectra) are well-documented for other metalloporphyrin systems with different metal axial coordination scenarios that lead to various oxidation/spin state combinations.[24–27] As illustrated in Figure 4.6 and summarized in Table 4.1, the frequencies of these peaks for each MOF system under different guest molecule environments follow the trends established by the corresponding reference complex spectra. Fe-PCN222-Pip is a notable exception, with significant spectral deviation from the $FeTPPpip_2$ reference, particularly in the spin state marker mode region. The implications of these spectral comparisons, in terms of iron coordination environments within the MOF structures, will be discussed below.

4.2.4 X-ray absorption spectroscopy

Fe K-edge XANES spectra for the reference complexes and MOFs are shown in Figure 4.7. The edge energies, as determined by the first inflection point (Figure 4.8), as well as the pre-edge peak energies are summarized in Table 4.2. XANES edge energies provide information on oxidation and the spin state of the absorbing atom. Moreover, the pre-edge features are also sensitive to metal oxidation and spin states as well as local geometry, with lower symmetry metal centers, such as C_{4v}, generally having more intense pre-edge features.[28] For all Fe(III)-based metalloporphyrin complexes and MOFs, the edge energy was found at ~7122 eV or higher, while the Fe(II) systems have lower energy edge positions at 7120.5 eV. This lower edge energy is consistent with the decrease in effective nuclear charge on the Fe sites upon reduction and is consistent with

values reported in the literature for similar iron porphyrin systems.[29] The pre-edge peak energies and intensities of the Fe(III) porphyrin-based MOFs (Figure 4.7a,b) closely match those of the corresponding reference complexes. Except for Fe-PCN222-Pip, which has a pre-edge feature consisting of multiple unresolved peaks, the pre-edge region of the Fe(II) porphyrin-based systems contains single peak maxima with comparably low energies and intensities (Figure 4.7c).

Table 4.2 Electronic Structure, Local Geometry, XANES Data, and IAD Results for Reference Complexes and MOFs Treated with Acetone, Imidazole, and Piperidine

	Ox. state	Spin State (S_{eff})[a]	XANES		XES				
			Pre-edge, eV	Edge, eV	K$\beta_{1,3}$, eV	Kβ' eV	IAD	Calc S	HS or LS, %
FeClTPP	+3	2.5	7113.5	7122.3	7058.7	7044.7	0.333	2.50	100% HS
FeCl-PCN222-ace	+3	2.5	7113.2	7122.5	7058.7	7044.7	0.335	2.52	100% HS
FeCl-PCN224-ace	+3	2.5	7113.5	7122.5	7058.9	7044.7	0.316	2.38	94% HS and 6% LS
$FeTPPIm_2Cl$	+3	0.5	7112.5	7122.0	7057.7	7045.5	0.062	0.47	100% LS
FeCl-PCN222-Im	+3	0.5	7112.5	7122.0	7057.7	7045.5	0.065	0.49	100% LS
FeCl-PCN224-Im	+3	0.5	7112.5	7121.7	7057.7	7045.2	0.065	0.49	100% LS
$FeTPPpip_2$	+2	0	7112.0	7120.5	7057.3	7044.0	0.026	0.19	9% HS and 91% LS
$FeTPPPy_2$	+2	0	7112.0	7120.5	7057.3	7044.0	0	0	100% LS
FeCl-PCN222-pip[b]	+2	1.33	7112.0, 7113.2	7120.5	7057.6	7044.3	0.181	1.42	71% HS and 29% LS
FeCl-PCN224-pip	+2	0	7112.0	7120.5	7057.8	7044.3	0.103	0.78	39% HS and 61% LS

[a]Effective spin state values, Seff, derived from space-filling model coordination pattern predictions (see text for details). [b]Effective spin state values calculated from IAD value. [c]XANES and XES data from ref [16].

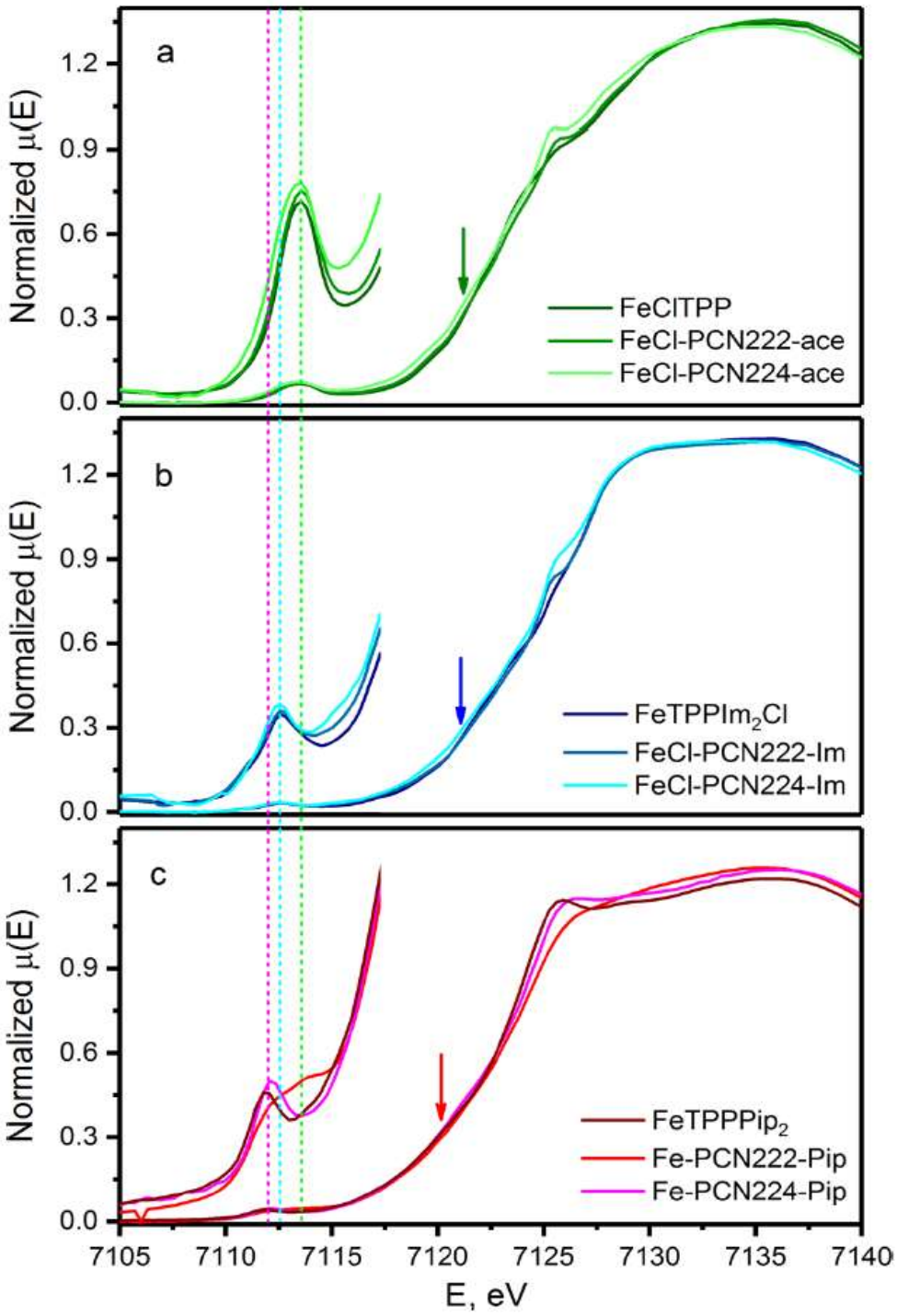

Figure 4.7 Normalized Fe K-edge XANES spectra with 10× magnification of the pre-edge region for (a) reference complexes FeClTPP, FeCl-PCN222-ace, FeCl-PCN224-ace; (b) $FeTPPIm_2Cl$, FeCl-PCN222-Im, FeCl-PCN224-Im; (c) $FeTPPPip_2$, Fe-PCN222-Pip,[16] Fe-PCN224-Pip.

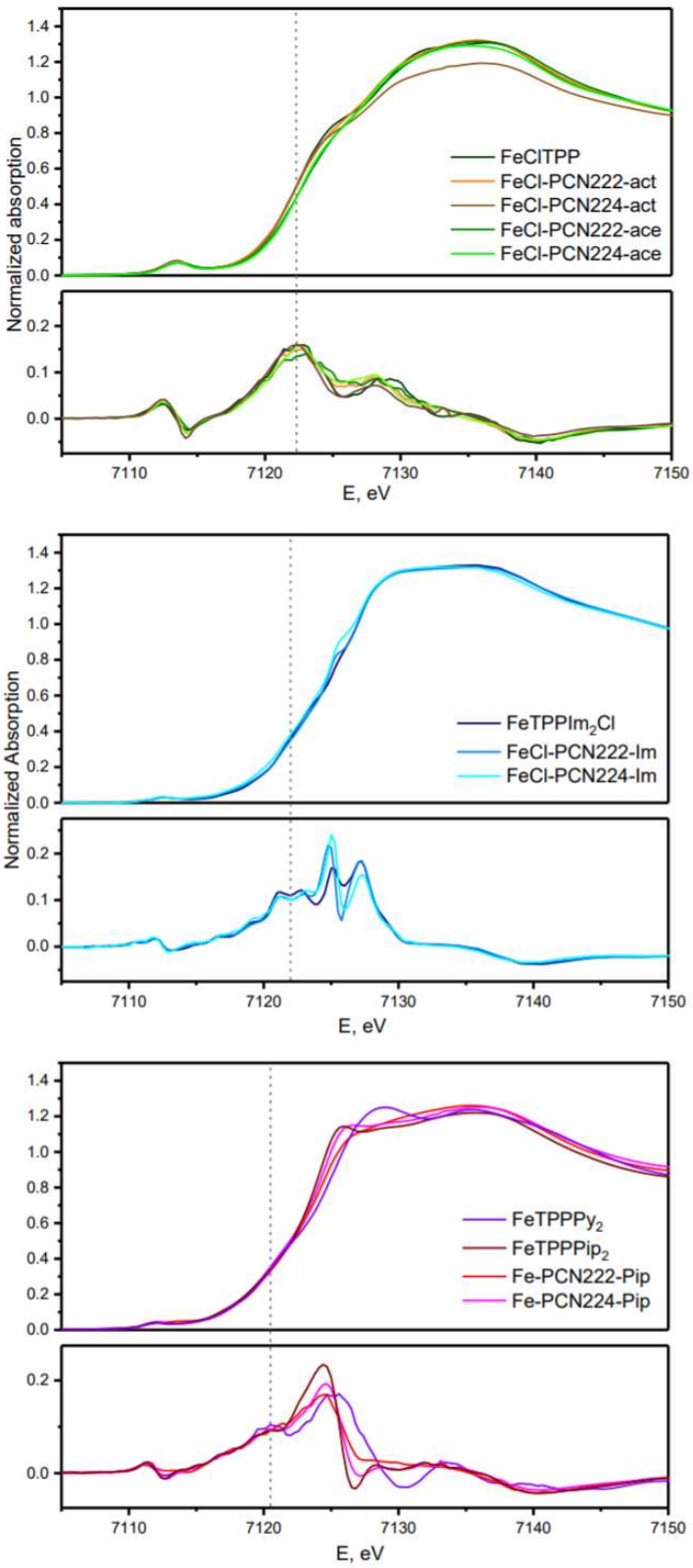

Figure 4.8 Fe K-edge XANES and derivative spectra for reference complexes and MOFs. Vertical dashed lines in top three panels indicate the first inflection points used to mark the edge energies reported in Table 2.

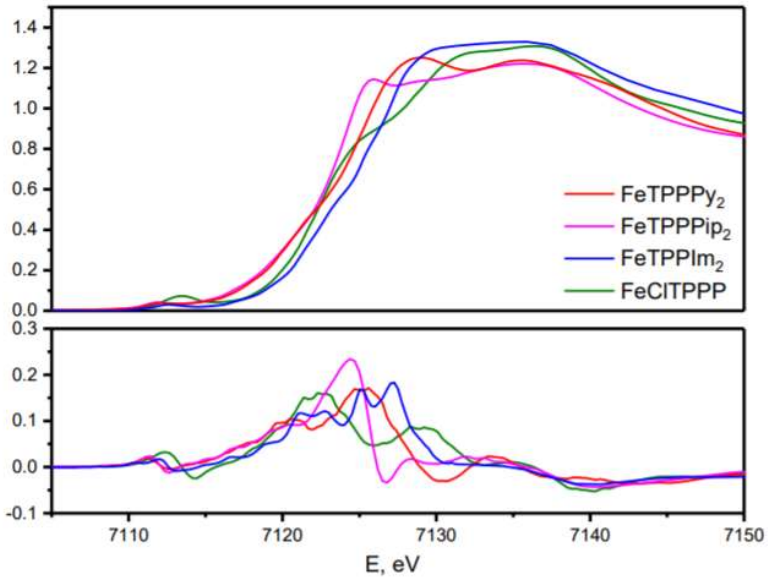

Figure 4.9 Fe K-edge XANES and derivative spectra for reference complexes.

The EXAFS data (Figure 4.10 for the frameworks under the different guest molecule environments follow the trends established by the corresponding reference complexes in terms of scattering distances. Most notably, the first shell peak position in the spectra of the porphyrin systems containing Fe-Cl coordination occurs at significantly higher $\chi(R)$ values than those of the iron porphyrin systems for which the axially coordinated chloride ligands are replaced by amines. This difference reflects the longer axial coordination bond length of Fe−Cl compared to Fe−N bonds associated with either imidazole or piperidine ligands. Attempts to fit these data to extract accurate coordination number information, however, were severely hindered by the uncertainties in the other parameters that also strongly influence the scattering amplitudes, namely, differences in the static disorder in the coordination bond lengths among these systems (i.e., σ^2 terms; the σ^2 term in the EXAFS equation accounts for the mean square variation in path length).

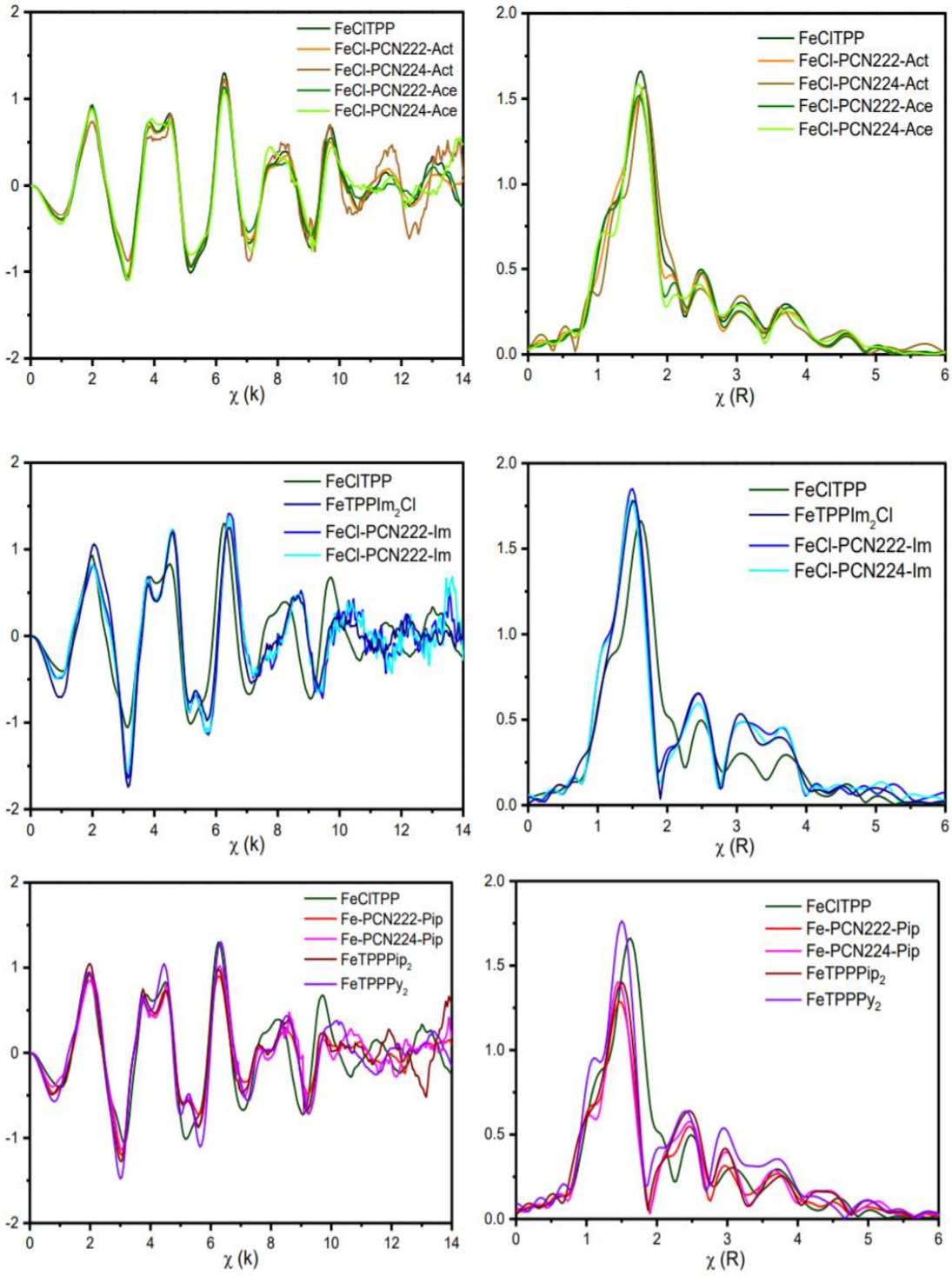

Figure 4.10 EXAFS spectra presented in k-space (left) and R-space (right) of reference complexes and MOFs. The spectrum of the FeClTPP reference is included along with the spectra of the amine axial ligand systems (middle and bottom rows of graphs) for comparison.

4.2.5 X-ray emission spectroscopy

Fe Kβ XES spectra (each normalized to unit area) obtained for the reference complexes and MOFs are shown in Figure 4.11 (top). These comparisons illustrate that the MOFs treated with acetone, FeCl-PCN222-ace and FeCl-PCN224-ace, along with the high-spin Fe(III) reference complex, FeClTPP, produce nearly identical X-ray emission spectra. Likewise, the spectra of the imidazole-treated MOFs, Fe-PCN222-Im and FePCN224-Im, also closely match that of the low-spin Fe(III) reference complex, $FeTPPIm_2Cl$. While the spectra of both low-spin Fe(II) reference complexes, $FeTPPPip_2$ and $FeTPPPy_2$, are quite similar to each other, those of the piperidine-treated MOFs, Fe-PCN222-Pip and Fe-PCN224-Pip, have notably different intensity ratios and energy splitting of the Kβ'and K$\beta_{1,3}$ bands compared to the reference complexes.

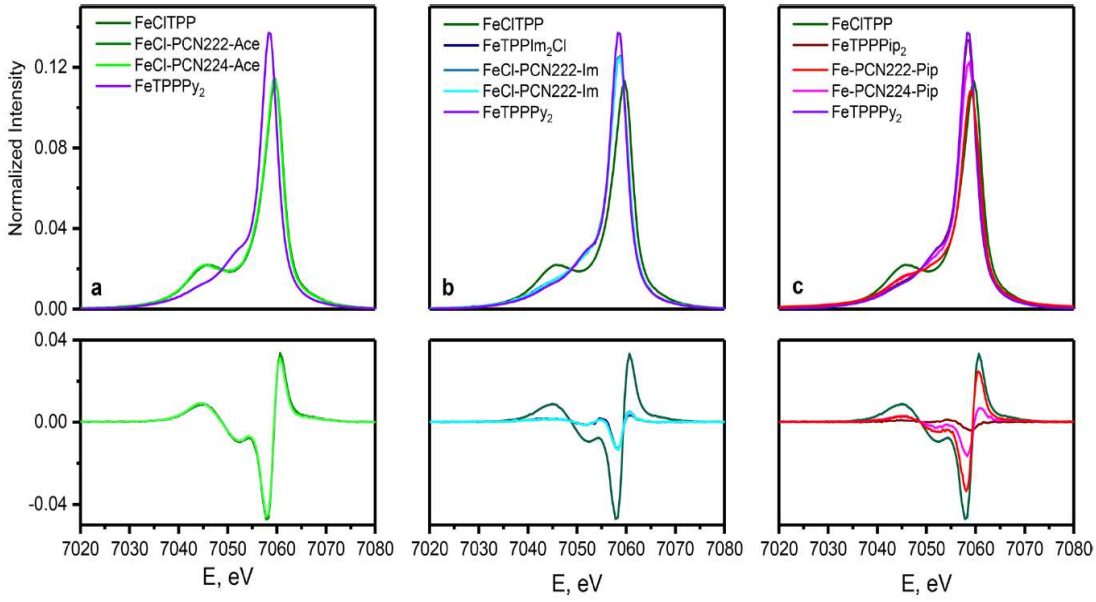

Figure 4.11 Normalized mainline Fe Kβ XES (top) and difference spectra for IAD analysis (bottom) for (a) Fe-PCN222-Ace, Fe-PCN224-Ace; (b) Fe-PCN222-Im, Fe-PCN224-Im; (c) Fe-PCN222-Pip,16 Fe-PCN224-Pip, and FeTPPPip2. The HS and LS reference complexes, FeClTPP and FeTPPPy2, respectively, are included in each graph for comparison. See text for details.

These spectral deviations are quantified using a line shape analysis method based on the integrated areas of the absolute values of difference spectra (IADs).[34–36] Since IAD values scale linearly with the corresponding difference in number of unpaired electrons (as previously discussed in chapter 1), an average spin state can be derived for each MOF system with either pure or mixed spin composition. These effective spin states, S_{eff}, are then broken down into the relative, relevant high, and low-spin state contributions in each case, (S = 2.5 and S = 0.5 for Fe^{3+} or S = 2 and S = 0 for Fe^{2+}). The results of this line shape analysis are summarized in Table 2. For the acetone- and imidazole treated Fe(III) MOF systems, calculated S_{eff} values indicate nearly pure high and low-spin state environments, respectively. The S_{eff} value calculated for the piperidine-treated MOFs, however, indicates a mixture of spin states in each case. The implications of these mixed spin environments will be discussed below. The difference spectra used in these analyses, generated from the XES spectra of each system and that of the low-spin reference complex, FeTPPPy2 (S = 0), are depicted in the bottom graphs of Figure 4.11.

4.3 Discussion

Spectroscopic characterization of the two MOF systems demonstrates significant differences in their host−guest interactions under acetone, imidazole, and piperidine guest environments. UV−vis DR, resonance Raman, and X-ray absorption spectroscopy together verify the presence of specific oxidation states of the iron sites in these materials. These measurements however only provide a qualitative assessment of the iron porphyrin coordination environments. Mainline Kβ XES data with IAD analysis is used to quantify the extent of axial metal ligation of the Fe porphyrin linkers within the MOF

systems since the different coordination scenarios yield different metal spin states. The spectroscopic analyses for the three guest molecule environments are summarized below and discussed in terms of the different framework-imposed structural restrictions on their axial binding behavior and reactivity in the MOFs.

4.3.1 Acetone-treated frameworks

The acetone-treated MOFs have nearly identical UV−vis DR spectra as that of the high-spin Fe(III) reference FeClTPP. Moreover, the similarity of the structure-sensitive mode frequencies in Raman spectra of these materials also indicates the presence of high-spin Fe(III) centers. Activation of the samples at 120°C does not cause significant change in either DR or Raman spectra (Figure 4.5c). The XANES spectra of the FeClTPP reference complex, and the MOFs upon activation and treatment with acetone, all contained an identically intense pre-edge feature at 7113.5 eV, as well as the same edge position at 7122.3. Additionally, the strong similarity of their EXAFS spectra to that of the FeClTPP complex (Figure 4.10) indicates parallel coordination environments involving the same scattering paths. These observations signify the presence of lower symmetry square-pyramidal Fe(III) high-spin centers,[45] as well as the absence of any appreciable interaction of acetone molecules with iron centers inside the framework. The purity of the high-spin (S = 2.5) environments is further confirmed by their Fe Kβ XES spectra, which show nearly identical $K\beta_{1,3}$-to-Kβ′ intensity ratios.

4.3.2 Imidazole-treated frameworks

Imidazole is known as a strongly binding ligand to the iron center in porphyrin environments.[46] Upon interaction with square-pyramidal Fe(III) porphyrin complexes, it

has been found that one imidazole molecule binds to the open axial position, while the second one substitutes the axial ligand, leading to the formation of hexacoordinated low-spin iron(III) centers. These differences in metal coordination and spin state cause drastic changes in the UV−vis DR, resonance Raman, XAS, and XES spectra. Spectral changes are consistent for the $FeTPPIm_2Cl$ reference complex and imidazole-treated MOFs. The shorter average first shell scattering distance associated with Fe-imidazole coordination is identically reflected by the EXAFS data (Figure 4.10) of $FeTPPIm_2Cl$, FeCl-PCN222-Im, and FeCl-PCN224-Im, which confirms the replacement of the chloride by the amine in all three systems. Qualitative comparison of XANES spectra for these systems shows that all three possess a low intensity pre-edge feature at 7112.5 eV and an edge position at 7122.0 eV, which are highly consistent with those reported for low-spin Fe(III) octahedral complexes.[29] More quantitative information on spin state is revealed through the IAD analysis of XES spectra. From the calculations, it was found that the effective spin state for both imidazole-treated MOFs as well as the corresponding reference complex is very close to S = 1/2 in each case, which is fully consistent with reported literature data.[47] Confirming our initial hypothesis based on space-filling models, the small size of the imidazole guest molecules allows for coordination at all pore-facing axial sites of the iron porphyrin linkers in both PCN222 and PCN224, thus leading to full formation of hexacoordinated metal centers in both frameworks.

4.3.3 Piperidine-treated frameworks

Unlike the other guest molecules discussed above, piperidine is expected to coordinate and reduce the iron (III) centers of the porphyrin linkers. The reference

complexes FeTPPPip$_2$, and FeTPPPy$_2$ both contain low-spin Fe(II) centers as evidenced by the resonance Raman, XAS, and XES characterization results. Spectral analyses of the PCN222 and PCN224 MOFs indicate a complete reduction of the iron sites to Fe(II) upon introduction of piperidine as well, but a mixture of axial coordination environments. The spectral differences can be quantitatively analyzed to estimate the ratio of the two spin states and therefore the two different axial ligation scenarios in Fe-PCN-222-pip and Fe-PCN-224-pip. One quantitative approach that has been established for evaluating relative spin state contributions to Kβ XES utilizes the integrated area of the absolute values of difference spectra (IADs) as a means for extracting the relative spin state contribution.[50,51] This line-shape analysis method takes advantage of the finding that IAD values scale linearly with the difference in number of unpaired electrons (ΔS) associated with the spectra used to generate the difference spectra. The effective or average spin state of a mixed-spin system of unknown composition compared to a reference with known spin state (e.g., a low-spin reference system), ΔS_{ML}, can be derived using the equations found on page 26 of this thesis. One of the advantages of this method is its dependence on the effective number of unpaired d electrons, rather than the oxidation state of the metal.[50,51] In our case, therefore, the spectra of FeClTPP (S = 5/2) and FePy$_2$TPP (S = 0) serve as the HS(*E*) and LS(*E*) references, respectively, to generate IAD_{HL}, with $\Delta S_{HL} = 5/2$. IAD_{ML} is then generated using the spectra of Fe-PCN-222-pip (MS(*E*)) and FePy$_2$TPP (LS(*E*)). The difference spectra are presented in Figure 4.9 (bottom). Following the above-described analysis, ΔS_{ML} is calculated to be 1.42. In terms of the relative Fe(II) spin state contributions to the Fe-PCN-222-pip spectrum, (i.e., S = 2 and 0), this ΔS_{ML} value translates to a 71% high-spin Fe(II) and 29% low-spin

Fe(II) composition. The small trigonal pores must therefore prevent full coordination of other piperidine molecules. In contrast to that framework, the pores in Fe-PCN224 allow equal access to both porphyrin axial ligation sites and, based on pore size alone, should allow for full coordination of piperidine at all iron sites. The resonance Raman spectrum of Fe-PCN224-Pip shows that the majority of structure-sensitive modes match those of the reference complex $FeTPPPip_2$. Analysis of the XANES spectrum affords a similar conclusion: a single low intensity pre-edge peak observed at 7112.2 eV and the edge position at 7120.5 eV indicate the predominance of hexacoordinate Fe(II) low-spin centers. The EXAFS data indicate coordination bond lengths consistent with axial amine coordination, although uncertainties in other factors influencing the scattering amplitudes prevent the extraction of accurate insights on coordination number, this is because axial and equatorial Fe-N and Fe-C cannot be distinguished by EXAFS.

By using spin state as an indicator of Fe(II) axial coordination status, Kβ XES provides the most accurate appraisal of the axial ligation of the iron porphyrin sites. The XES spectrum of Fe-PCN224-Pip has more intensity in the Kβ' region compared to that of the low spin Fe(II) reference complex spectra, which indicates a small presence of high-spin component. IAD analysis yields a quantitative assessment of the overall spin state of the system and therefore a more accurate estimate for the ratio of high-spin (5-coordinate) to low-spin (6-coordinate) Fe (II) centers. This ratio was calculated to be ~1:1.6, or 61% HS spin and 39% LS. While confirming the trend that the uniform, larger pore size of the PCN224 framework can accommodate full axial ligation of the iron porphyrin sites, this result is notably different from the space-filling model predictions. There are a couple of possibilities for this undersaturation. The simplest explanation

would be that substantial framework collapse had occurred and the loss in crystallinity rendered a substantial number of pores inaccessible to the piperidine guest molecules. XRD analysis, however, indicates comparably high crystallinity of this framework both before and after piperidine treatment as was found for the PCN222 MOF. While a small degree of pore collapse may be occurring, this alone would not account for the lower than predicted axial ligation of the Fe coordination sites.

A more likely contributor may be found in the byproduct of the reduction reaction.[17] Upon reaction with Fe(III) porphyrin, piperidine is oxidized to piperideine, which is known to trimerize (Scheme 4.1).[48,49]

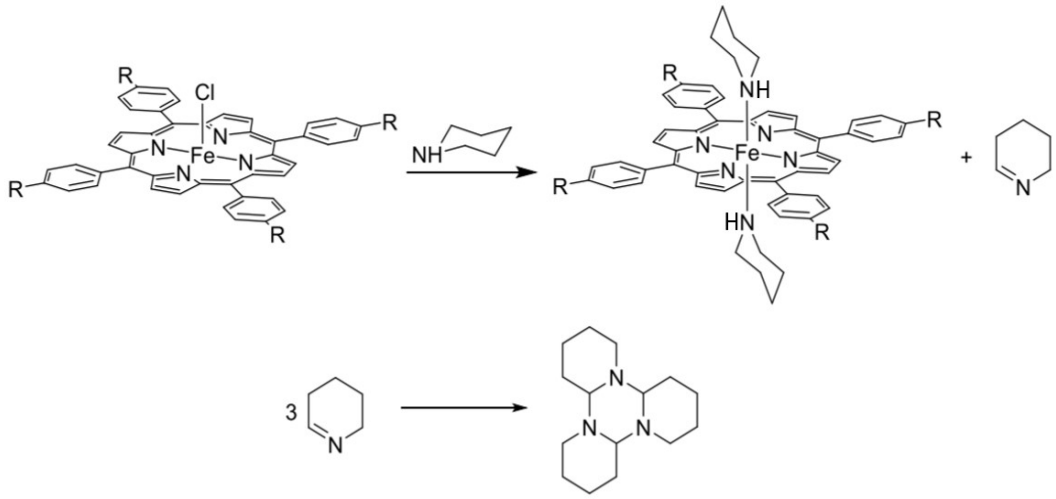

Scheme 4.1 Proposed formation trimer after oxidation of piperidine

Formation of this bulky trimer within the pores may block access and prevent coordination of other piperidine molecules, leading to the formation of coordinatively unsaturated metal centers. This hypothesis is first supported by our observation that activation of this piperidine-treated framework, unlike all the other guest-treated

frameworks of this study, did not exhibit the expected weight loss that is commensurate with guest removal from the pores.[5,7] For further proof, we confirmed the presence of the trimer by high resolution ESI-MS (Figure 4.12) after digestion of the MOF in NaOH solution, followed by organic fraction extraction. Both findings indicate that, unlike acetone or imidazole, the piperidine oxidation side product is too large to exit the pores and remains trapped within the framework even after activation.

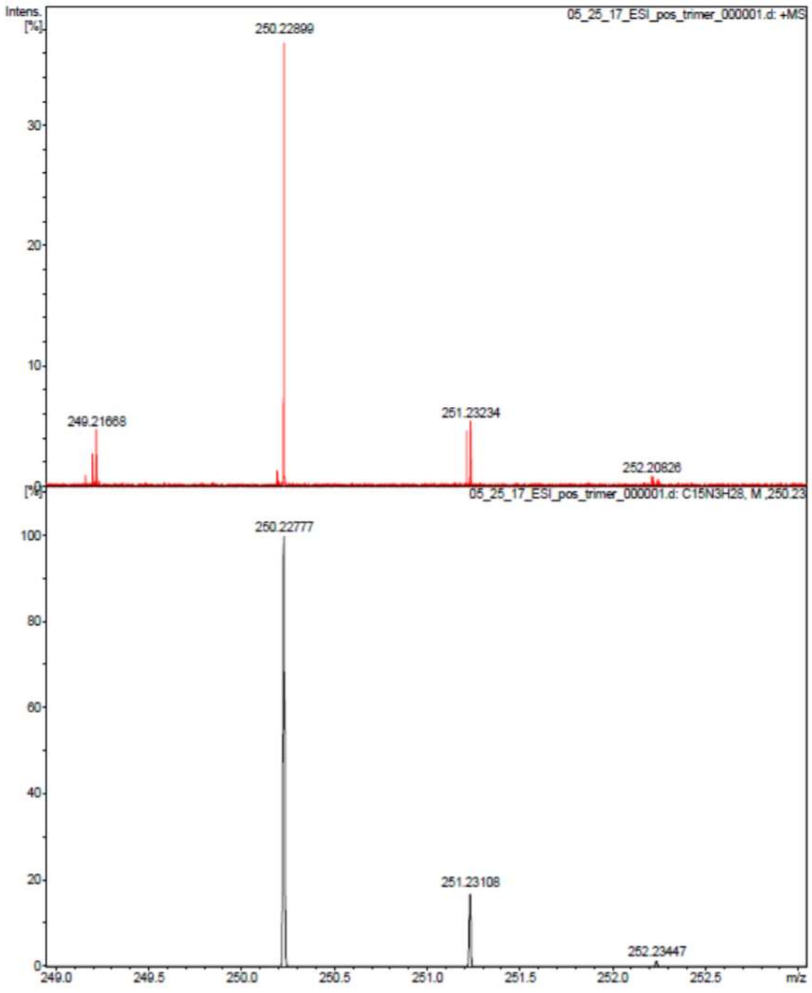

Figure 4.12 ESI-MS spectrum of isolated 2,3,4,5-tetrahydropyridine trimer from Fe-PCN224- Pip. Top: experimental, bottom: simulated.

4.4 Conclusion

Pore size restrictions on axial host−guest interactions of metalloporphyrin linkers in MOF environments may drastically affect their spin states and overall red-ox reactivity with respect to the substrate and therefore their potential catalytic properties. From that perspective, this comparative study serves to demonstrate the complexity of these interactions that occur inside the pores of the MOF. While smaller substrates may fully coordinate to the metal centers, as illustrated by the imidazole guest example, larger ones (like piperidine) can leave some metal centers coordinatively unsaturated due to steric effects. Moreover, as the likely trimerization of the oxidized piperidine guest species in PCN224 demonstrates, further reactivity of redox products trapped within the frameworks can lead to bulky side products that can block otherwise open porphyrin linker metal sites. All of the above factors related to the size and reactivity of the guest and the framework pores are relevant when utilizing or designing new porphyrin-based MOF catalysts.

4.5 Materials and Methods

4.5.1 Materials

Reference complexes, $FeTPPIm_2Cl$, $FeTPPPip_2$, and FeTPPPy2 (TPP = tetraphenylporphyrin, Im = imidazole, Pip =piperidine, and Py = pyridine), were prepared according to literature procedures,[18,20,40,41] as were the FeCl-PCN222[5] and FeCl-PCN224[6] MOFs, with some modifications. Following solvent exchange and activation via vacuum assisted heat treatment (120 °C for 12 h),[5,16] the resulting activated MOFs, FeCl-PCN222-act and FeCl-PCN224-act, were suspended in either acetone, piperidine, or a

dichloromethane solution of imidazole, utilizing modified treatment procedures based on the synthesis of the reference complexes $FeTPPPip_2$,[18] and $FeTPPIm_2Cl$,[20] to generate the amine guest molecule-loaded frameworks, Fe-PCN222-Pip, Fe-PCN224-Pip, FeCl-PCN222-Im, and FeCl-PCN224-Im, respectively. Crystallinity of the MOF samples before and after treatment with different guests was confirmed by powder XRD (Figure 4.2).

4.5.2 UV-vis Diffuse Reflectance

UV−vis diffuse reflectance spectra were collected using a Cary-Varian UV−visible− NIR spectrophotometer equipped with a diffuse reflectance accessory (Harrick Scientific). Samples were mixed with KBr and finely ground to ensure even dilution of the sample. Air-sensitive samples were prepared in the same way inside the glovebox and transferred to the spectrophotometer in the sealed vials to prevent sample oxidation. Spectra were plotted in Kubelka−Munk units and normalized to the maximum of the Soret band for better comparison.

4.5.3 Raman Spectroscopy

Raman spectra were collected at room temperature using a 532 nm single-frequency diode-pumped solid-state laser (Spectra-Physics) with ∼8 mW power, a triple monochromator, and a 1340 × 100 pixel liquid nitrogen-cooled CCD detector (Princeton Instruments). Air-stable samples in the form of pellets were made by mixing 20% iron porphyrin complex or MOF with 20% of KNO_3 and 60% of KBr. Air-sensitive samples

in powder form were packed into a 1 mm quartz cell inside a glovebox. The cell was sealed in order to avoid exposure to air. All samples were spun during alignment and data acquisition to minimize photo and thermal damage due to exposure to the laser light.

4.5.4 X-ray Absorption Spectroscopy

X-ray absorption data were collected at the Fe K-edge (7111.2 eV) in transmission mode at either Beamline 2-2 at SSRL or 20ID at APS. At both beamlines, the X-ray white beam was monochromatized by a Si(111) monochromator. At SSRL, the monochromatized beam (1.5 × 1 mm spot size, 0.3 eV resolution) was detuned by 30% to minimize the harmonic content of the beam. The incident beam intensity (I_0) was measured by a 15 cm ionization chamber with 100% N2 while the transmitted (I_t) and reference (I_r) beam intensities were both measured by 30 cm ionization chambers with 75% N_2 and 25% Ar gas mixtures. At APS, the monochromatized beam was focused (50 × 50 μm spot size, 0.2 eV resolution) and detuned by 15%. I_0, I_t, and I_r were measured by 5, 30, and 5 cm ionization chambers, respectively, each with 100% N_2.

Iron foil was used as the reference for energy calibration at both beamlines. For the reference complexes, a mixture of 20 mg of sample thoroughly ground with ∼100 mg of boron nitride was packed into 3 mm Kapton tubes for experiments at SSRL and undiluted reference complexes were packed in 1 mm tubes for measurements at APS to yield approximately one X-ray absorption length. All tubes were heat sealed prior to measurement. MOF samples were thoroughly ground and used without additional dilution. Air-sensitive samples, $FeTPPPip_2$, $FeTPPPy_2$, FeCl-PCN222-act, FeCl-PCN224-act, Fe-PCN222-Pip, and Fe-PCN224-Pip, were packed in the capillary tubes in

the glovebox and pre-sealed using vacuum grease prior to permanent heat sealing performed outside the glovebox. All data were collected at room temperature. At SSRL, three spectra were collected for each sample and compared in order to verify the absence of X-ray damage. At APS, damage prevention was achieved by using the following protocol: (1) defocusing the X-ray beam to a spot size of 50 × 50 μm at the sample, (2) closing the X-ray shutter between each movement of the monochromator, and (3) linearly translating the sample in 50 μm steps after each scan. Obtained spectra were averaged over 3 scans.

4.5.5 X-ray Emission Spectroscopy

Nonresonant Fe Kβ XES spectra were collected at room temperature at beamline C1 at CHESS.[42] The incident X-ray energy was set to 8000 eV, with a beam size of 1 × 1 mm. X-ray emission was collected using five spherically bent Ge(620) analyzer crystals aligned in the Rowland circle geometry and focused to a Pilatus 1000k detector. A helium-filled bag was placed between the analyzer crystals and detector to maximize the collection efficiency of the emission. Energy resolved spectra were collected between 7010 and 7085 eV with 0.2 eV step. A total of three spectra were collected and averaged for each sample. Samples were packed in sealed 1.6 mm Kapton tubes without dilution and were translated within the X-ray beam by 1 mm between each spectrum scan in order to avoid sample damage. Air-sensitive samples were packed in the glovebox in a similar way as those prepared for XAS measurements, as described above.

4.6 References

[1] Bhyrappa, P.; Wilson, S. R.; Suslick, K. S., *J. Am. Chem. Soc.* **1997**, *119,* 8492−8502.

[2] Chou, J.-H.; Kosal, M. E.; Nalwa, H. S.; Rakow, N. A.; Suslick, K.S., *In The Porphyrin Handbook*, **2000**, Kadish, K., Smith, K., Guilard, R., Eds.; Academic Press: New York, Vol. 6, 43−131.

[3] Suslick, K. S.; Bhyrappa, P.; Chou, J.-H.; Kosal, M. E.; Nakagaki, S.; Smithenry, D. W.; Wilson, S. R., *Acc.Chem. Res.* **2005**, *38*, 283−291.

[4] Chen, Y.; Hoang, T.; Ma, S., *Inorg. Chem.* **2012**, *51*, 12600−12602.

[5] Feng, D.; Gu, Z-Y.; Li, J.-R.; Jiang, H.-L.; Wei, Z.; Zhou, H.-C., *Angew. Chem., Int. Ed.* **2012**, *51*, 10307−10310.

[6] Morris, W.; Volosskiy, B.; Demir, S.; Gándara, F.; McGrier, P. L.; Furukawa, H.; Cascio, D.; Stoddart, J. F.; Yaghi, O. M., *Inorg. Chem.* **2012**, *51*, 6443−6445.

[7] Feng, D.; Chung, W.-C.; Wei, Z.; Gu, Z.-Y.; Jiang, H.-L.; Chen,Y.-P.; Darensbourg, D. J.; Zhou, H.-C., *J. Am. Chem. Soc.* **2013,** *135*, 17105−17110.

[8] Feng, D.; Gu, Z.-Y.; Chen, Y.-P.; Park, J.; Wei, Z.; Sun, Y.; Bosch, M.; Yuan, S.; Zhou, H.-C., *J. Am. Chem. Soc.* **2014**, *136*, 17714−17717.

[9] Brown, J. W.; Nguyen, Q. T.; Otto, T.; Jarenwattananon, N. N.;Glöggler, S.; Bouchard, L.-S., *Catal. Commun.* **2015**, *59*, 50−54.

[10] Burnett, B. J.; Barron, P. M.; Choe, W., *CrystEngComm* **2012**, *14*, 3839−3846.

[11] Gao, W.-Y.; Chrzanowski, M.; Ma, S., *Chem. Soc.Rev*. **2014**, *43*, 5841−5866.

[12] Zhao, M.; Ou, S.; Wu, C.-D., *Acc. Chem. Res.* **2014**, *47*, 1199−1207.

[13] Farha, O. K.; Shultz, A. M.; Sarjeant, A. A.; Nguyen, S. T.; Hupp, J. T., *J. Am. Chem. Soc.* **2011**, *133*, 5652−5655.

[14] White, W. I., In Porphyrins; Dolphin, D., Ed.; Academic Press: New York, **1978**, *Vol. 5*, 202−340.

[15] Xie, M.-H.; Yang, X.-L.; He, Y.; Zhang, J.; Chen, B.; Wu, C.-D., *Chem. - Eur. J.* **2013**, *19*, 14316−14321.

[16] Kucheryavy, P.; Lahanas, N.; Velasco, E.; Sun, C.-J.; Lockard, J. V., J. *Phys. Chem. Lett.* **2016**, *7,* 1109−1115.

[17] Castro, C. E.; Jamin, M.; Yokoyama, W.; Wade, R., *J. Am. Chem. Soc.* **1986**, *108*, 4179−4187.

[18] Radonovich, L. J.; Bloom, A.; Hoard, J. L., *J. Am. Chem. Soc*. **1972**, *94*, 2073−2078.

[19] Walker, F. A.; Lo, M.-W.; Ree, M. T., *J. Am. Chem. Soc.* **1976**, *98*, 5552−5560.

[20] Scheidt, W. R.; Osvath, S. R.; Lee, Y. J., *J. Am. Chem. Soc.* **1987**, *109*, 1958−1963.

[21] Kobayashi, H.; Yanagawa, Y., *Bull. Chem. Soc. Jpn*. **1972**, *45*, 450−456.

[22] Mezger, M.; Hanack, M.; Hirsch, A.; Kleinw ächter, J.; Mangold, K.-M.; Ramaswami Subramanian, L., *Chem. Ber.* **1991,** *124*, 841−847.

[23] Spiro, T. G.; Strekas, T. C., *J. Am. Chem. Soc.* **1974**, *96*, 338−345.

[24] Parthasarathi, N.; Hansen, C.; Yamaguchi, S.; Spiro, T. G., *J. Am. Chem. Soc.* **1987**, *109*, 3865−3871.

[25] Oshio, H.; Ama, T.; Watanabe, T.; Kincaid, J.; Nakamoto, K., *Spectrochim. Acta, Part A*, **1984**, *40*, 863−870.

[26] Chottard, G.; Battioni, P.; Battioni, J. P.; Lange, M.; Mansuy, D., *Inorg. Chem.* **1981**, *20*, 1718−1722.

[27] Paulat, F.; Praneeth, V. K. K.; Näther, C.; Lehnert, N., *Inorg. Chem.* **2006**, *45*, 2835−2856.

[28] Westre, T. E.; Kennepohl, P.; DeWitt, J. G.; Hedman, B.; Hodgson, K. O.; Solomon, E. I., *J. Am. Chem. Soc.* **1997**, *119*, 6297−6314.

[29] Wilson, S. A.; Green, E.; Mathews, I. I.; Benfatto, M.; Hodgson, K. O.; Hedman, B.; Sarangi, R., *Proc. Natl. Acad. Sci. U. S. A.* **2013**, *110*, 16333−16338.

[30] Cartier, C.; Momenteau, M.; Dartyge, E.; Fontaine, A.; Tourillon, G.; Michalowicz, A.; Verdaguer, M., *J. Chem. Soc.,* Dalton Trans. **1992**, 609−618.

[31] Tsutsumi, K.; Nakamori, H.; Ichikawa, K., *Phys. Rev. B* **1976**, *13*, 929−933.

[32] Peng, G.; deGroot, F. M. F.; Haemaelaeinen, K.; Moore, J. A.; Wang, X.; Grush, M. M.; Hastings, J. B.; Siddons, D. P.; Armstrong, W. H., *J. Am. Chem. Soc.* **1994**, *116*, 2914−2920.

[33] Peng, G.; Wang, X.; Randall, C. R.; Moore, J. A.; Cramer, S. P., *Appl. Phys. Lett.* **1994**, *65*, 2527−2529.

[34] Vankó, G.; Neisius, T.; Molnár, G.; Renz, F.; Kárpáti, S.; Shukla, A.; de Groot, F. M. F., *J. Phys. Chem. B*, **2006**, *110*, 11647−11653.

[35] Rueff, J. P.; Shukla, A.; Kaprolat, A.; Krisch, M.; Lorenzen, M.; Sette, F.; Verbeni, R., *Phys. Rev. B: Condens. Matter Mater. Phys*. **2001**, *63,* 132409.

[36] Vankó, G.; Rueff, J.-P.; Mattila, A.; Németh, Z.; Shukla, A., *Phys. Rev. B: Condens. Matter Mater. Phys.* **2006**, *73*, 024424.

[37] Mebs, S.; Braun, B.; Kositzki, R.; Limberg, C.; Haumann, M., *Inorg. Chem*. **2015**, *54*, 11606−11624.

[38] Wu, L.-C.; Weng, T.-C.; Hsu, I.-J.; Liu, Y.-H.; Lee, G.-H.; Lee, J.- F.; Wang, Y., *Inorg. Chem.* **2013**, *52*, 11023−11033.

[39] Gul, S.; Ng, J. W. D.; Alonso-Mori, R.; Kern, J.; Sokaras, D.; Anzenberg, E.; Lassalle-Kaiser, B.; Gorlin, Y.; Weng, T.-C.; Zwart, P. H.; Zhang, J. Z.; Bergmann, U.; Yachandra, V. K.; Jaramillo, T. F.; Yano, J., *Phys. Chem. Chem. Phys*. **2015**, *17*, 8901−8912.

[40] Li, N.; Petricek, V.; Coppens, P.; Landrum, J., *Acta Crystallogr., Sect. C: Cryst. Struct. Commun.* **1985**, *41*, 902−905.

[41] Collman, J. P.; Hoard, J. L.; Kim, N.; Lang, G.; Reed, C. A., *J. Am. Chem. Soc.* **1975**, *97*, 2676−2681.

[42] Finkelstein, K. D.; Pollock, C. J.; Lyndaker, A.; Krawcyk, T.; Conrad, J., *AIP Conf. Proc.* **2015**, *1741*, 030009.

[43] Kucheryavy, P.; Lahanas, N.; Lockard, J. V., *J. Coord. Chem.* **2016**, *69*, 1780-1791.

[44] Choi, S.; Spiro, T. G.; Langry, K. C.; Smith, K. M., *J. Am. Chem. Soc.* **1982**, *104*, 4337−4344.

[45] Xu, W.; Dziedzic-Kocurek, K.; Yu, M.; Wu, Z.; Marcelli, A., *RSC Adv.* **2014**, *4*, 46399−46406.

[46] Sheidt, W. R., *In The Porphyrin Handbook*, Kadish, K., Smith, K., Guilard, R., Eds.; Academic Press: New York, **2000**; *Vol. 3*, 49−112.

[47] Epstein, L. M.; Straub, D. K.; Maricondi, C., *Inorg. Chem.* **1967**, *6*, 1720−1724.

[48] Gravel, E.; Poupon, E.; Hocquemiller, R., *Tetrahedron*, **2006**, *62*, 5248−5253.

[49] Leeper, F. J.; Grue-Sørensen, G.; Spenser, I. D., *Can. J. Chem.* **1981**, *59*, 106−115.

[50] Vanko, G.; Neisius, T.; Molnaŕ , G.; Renz, F.; Kaŕ pat́ i, S.; Shukla, A.; de Groot, F. M. F., *J. Phys. Chem. B*, **2006**, *110*, 11647−11653.

[51] Vanko, G.; Rueff, J.-P.; Mattila, A.; Neḿ eth, Z.; Shukla, A. *Phys. Rev. B: Condens. Matter Mater. Phys*. **2006**, *73*, 024424.

[52] Balch, A. L.; Noll, B. C.; Olmstead M. M.; Phillips S. L.; *Inorg Chem,* **1996**, 35, 6495-6506.

Chapter 5. Crystallographic identification of a series of manganese porphyrin complexes with nitrogenous bases

5.1 Introduction

Metalloporphyrin complexes have long been investigated to gain a better understanding of small-molecule activation, transport, and storage behavior in related heme-based protein systems[1-2]. Manganese(III) porphyrin complexes are important model systems in the study of these naturally occurring proteins through their incorporation into apoproteins with heme-binding sites[3-4] or by comparison with iron porphyrin analogues.[5-6] Moreover, like Fe porphyrins, Mn porphyrin complexes demonstrate elevated reactivity toward biomimetic oxidation.[6-9] Furthermore, it has been shown that the interaction of manganese complexes with amines influences their reactivity. For example, in the oxidation of olefins catalyzed by manganese porphyrin complexes, the presence of the amine may limit the reaction rate and yield.[10] Another important catalytic reaction involves the oxidation of amines to imines by Mn porphyrins.[11-14] This reactivity is particularly appealing for incorporation in solid-state materials, such as thin-film-deposited surfaces[15-16], zeolites[17], or metal–organic frameworks (MOFs)[18]. The key to their biological function and catalytic behavior in protein or other environments lies in their affinity for axial binding at the metalloporphyrin active sites. In-depth characterization of these metalloporphyrin complexes with a range of axially coordinating ligands therefore continues to be an important avenue of investigation for understanding their reactivity in these environments.[19-21] Amine-based axial ligands are important for their biological and catalytic relevance. While the structures and axial ligation properties of iron porphyrin complexes with several nitrogenous base ligands

have been thoroughly explored[22-25], their manganese counterparts have undergone far less characterization.[3, 26-29] Moreover, the planarity of the porphyrin ring and its relation to the binding affinities of the ligand is an important aspect of metalloporphyrin chemistry that has been extensively studied for nickel[30-32] and iron porphyrin complexes,[33] but not for the manganese porphyrin analogues.

In this chapter, the syntheses and crystal and molecular structures are reported for three new manganese porphyrin complexes with different nitrogenous base ligands, namely bis(imidazole)(5,10,15,20-tetraphenylporphyrinato)manganese(III) chloride chloroform disolvate, [Mn(TPP)(im)$_2$]-Cl*2CHCl$_3$, (I), bis(piperidine)(5,10,15,20-tetraphenylporphyrinato) manganese(III) chloride, [Mn(TPP)(pip)$_2$]Cl, (II), and chlorido(1,4-diazabicyclo[2.2.2]octane)(5,10,15,20-tetraphenyltetraphenylporphyrin) manganese(III)–1,4-diazabicyclo[2.2.2]octane–toluene–water (4/4/4/1), [Mn(TPP)Cl(DABCO)]*(DABCO)* (toluene)*0.25H2O, (IV), as well as a fourth complex, chlorido(pyridine)(5,10,15,20-tetraphenylporphryinato)manganese(III) pyridine disolvate, [Mn(TPP)Cl(py)] * 2(py), (III), a structure previously published by Kirner & Scheidt (1975)[29], but prepared by a new method of crystallization and having a slightly different structure than that reported previously (Scheme 5.1). The series of amines, i.e. imidazole, piperidine, pyridine, and DABCO, present a range of basicities and axial coordination affinities. Piperidine, based on literature precedents,[34] can cause the reduction of the Mn porphyrin complex, leading to the formation of a Mn(II) porphyrin species. Axial ligand binding constants for two of the complexes were determined in chloroform solution and are reported and discussed. The reported complexes serve as model systems for comparison with Mn-porphyrin-based MOF materials containing

analogous axially coordinating nitrogenous base guest molecules. As part of this related project, XANES data for the analogous Mn-porphyrin MOF, PCN-222, and the new reference complexes will be discussed as well.

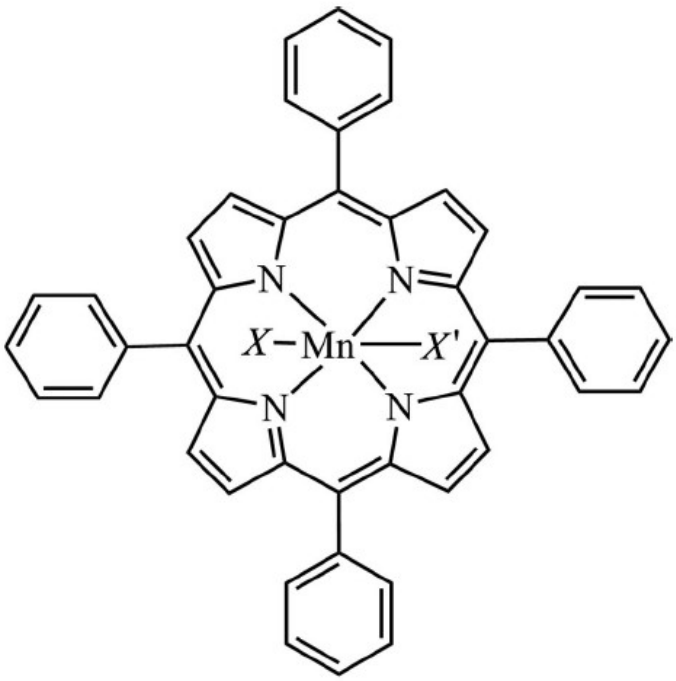

(I) $X = X'$ = imidazole
(II) $X = X'$ = piperidine
(III) X = pyridine, X' = Cl
(IV) X = DABCO, X' = Cl

Scheme 5.1 Manganese porphyrin complex with axially coordinating nitrogenous bases

5.2 Results

The $[Mn(TPP)(im)_2]^+$ cation is shown in Figure 5.1, looking down on the Mn porphyrin plane; in this view, the imidazole ligands are oriented above and below the Mn porphyrin plane (see Figure 5.2). The structures of $[Mn(TPP)(pip)_2]^+$, $[Mn(TPP)Cl(py)]^+$, and

$[Mn(TPP)(DABCO)Cl]^+$ are similar, differing only in the axial substituents. Accordingly, only the diagrams with the view parallel to the porphyrin ring systems are included for the other structures (Figures. 5.3, 5.4 and 5.5).

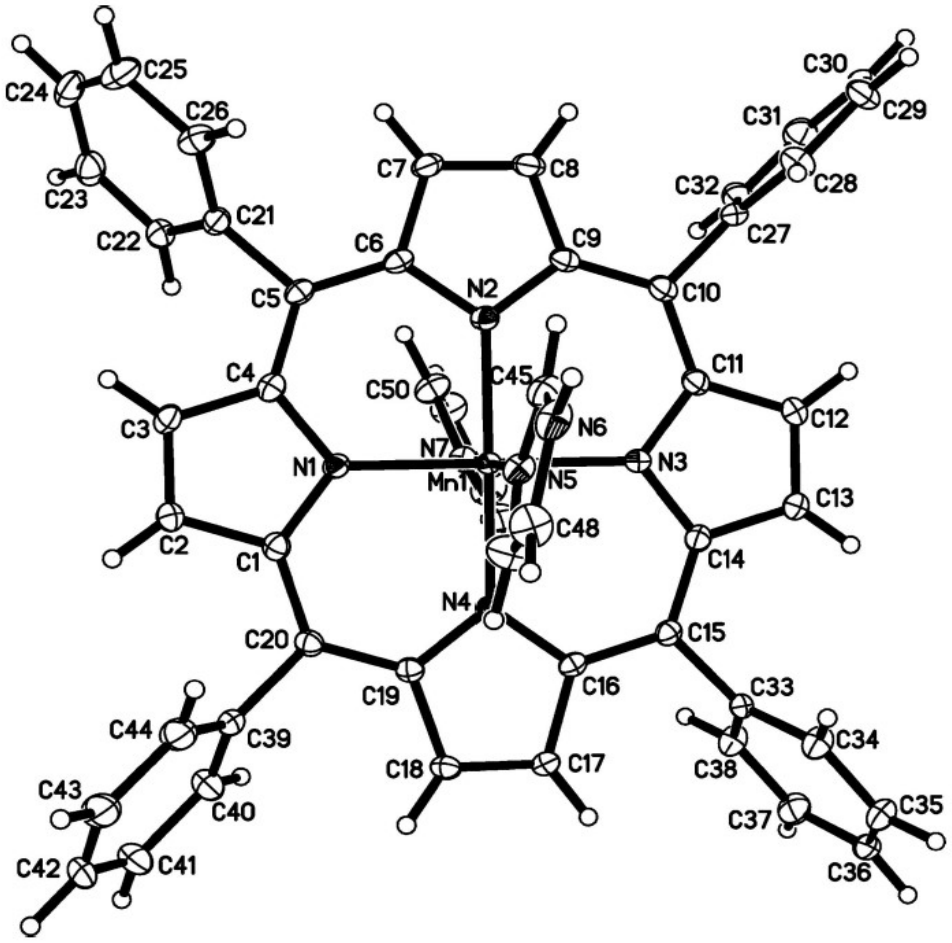

Figure 5.1 The asymmetric unit of the $[Mn(TPP)(im)_2]^+$ cation looking down on the porphyrin plane. Displacement ellipsoids are drawn at the 40% probability level. H atoms are represented by spheres of arbitrary radius.

5.2.1 Crystal Structure of $[Mn(TPP)(im)_2]^+$ (I)

The $[Mn(TPP)(im)_2]^+$ cation crystallizes with a noncoordinating chloride and with two molecules of chloroform. The Mn—N bond lengths in the porphyrin ring and the

Mn—N bond lengths for both of the imidazole rings are all given in Table 5.2. The Mn1 atom essentially sits in the plane of the four N atoms, being only -0.0075 (8) Å out of the plane. The dihedral angle between the two imidazole rings, i.e. N5/ C45/N6/C46/C47 versus N7/C48/N8/C49/C50, is 37.98 (13)° (Figure 5.1), whereas the dihedral angles of the imidazole ring plane versus the coordination plane of the porphyrin ring, i.e. Mn/N1/N2/N3/N4, are 87.08 (8)° and 77.01 (9)° for the N5/N6- and N7/N8-containing rings, respectively. The N5—Mn1—N7 angle is nearly linear at 178.65 (7)°. The N6—H6---Cl1 hydrogen-bond angle is 166° and the N8—H8---Cl1A [symmetry code: (A) x, y + 1, z] angle is 161°. The Mn porphyrin moiety (Figure 5.2) is slightly nonplanar, as evidenced by the orientation of the pyrrole rings: the dihedral angle between the planes defined by C1–C5/N1/C15–C20/N4 and C5–C9/N2/C10–C15/N3 is 5.64 (5)°, while that between the planes C20/N1/C1–C10/N2 and N3/C10–C20/N4 is 6.79 (5)°. Also, the dihedral angles between the planes defined by C39/C20/Mn1 and C27/C10/Mn1, and between the planes defined by C33/C15/Mn1 and C21/C5/Mn1 are 1.64 (9)° and 6.27 (9)°, respectively. The dihedral angles between the planes of the core and the planes of the phenyl groups are all given in Table 5.2; they range between 64.48 (8)° and 88.75 (7)°. Shown in Figure 5.2 is the hydrogen bond between each of the imidazole N—H groups and the Cl1 counter-ion; for N6—H6---Cl1, the donor–acceptor distance is 2.26 Å and for N8—H8---Cl1A it is 2.28 Å.

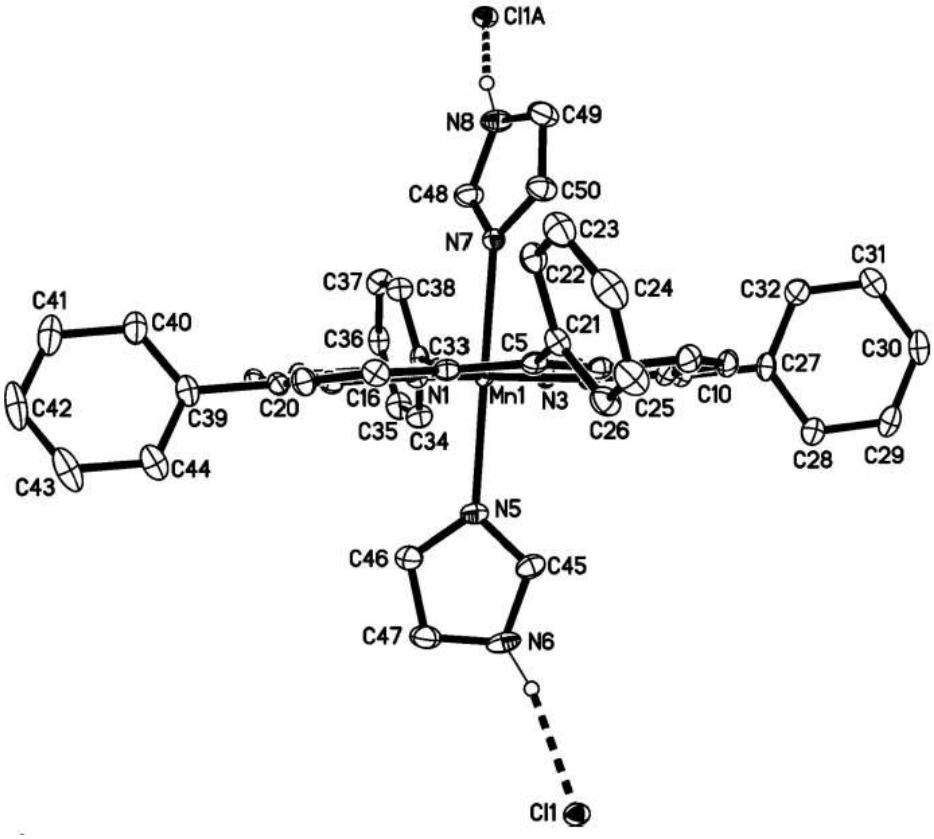

Figure 5.2 A view of the $[Mn(TPP)(im)_2]^+$ cation parallel to the porphyrin plane; only H atoms involved in hydrogen bonding to the chloride anion are shown. Displacement ellipsoids are drawn at the 40% probability level.

5.2.2 Crystal Structure of $[Mn(TPP)(pip)_2]^+$ (II)

The structure of the $[Mn(TPP)(pip)_2]^+$ cation of (II) is shown in Figure 5.3, in addition to the charge-balancing Cl^- counter-ion. The electron-density peaks suggested one mixed-occupancy piperidine/piperidinium chloride moiety of crystallization in the asymmetric unit, or two molecules per formula unit (one protonated, one not), situated in a cavity around a center of symmetry, plus a water molecule. The piperidine/piperidinium moiety was disordered over at least two orientations; however, attempts to model this were difficult. Accordingly, the SQUEEZE routine[37] of PLATON[38] was used to account

for the diffuse/disordered moieties, giving an electron count of 112 in a volume of 380 e Å^{-3}, consistent with one piperidine molecule, one piperidinium chloride unit and one water molecule per formula unit, i.e. $(C_5H_{12}N)[Mn(TPP)(pip)_2]Cl*[C_5H_{12}N^+*Cl^-]*(pip)*H_2O$. By measuring the density of this complex by the floatation method using hexane and carbon tetrachloride, we obtained 1.290 Mg m^{-3}. This allows us to calculate the molecular weight of the complete material and this is 1097.8 g mol^{-1}, leading to the above formulation for the disordered complex. The porphyrin ring system is planar. All pertinent bond lengths and angles can be found in Table 5.2.

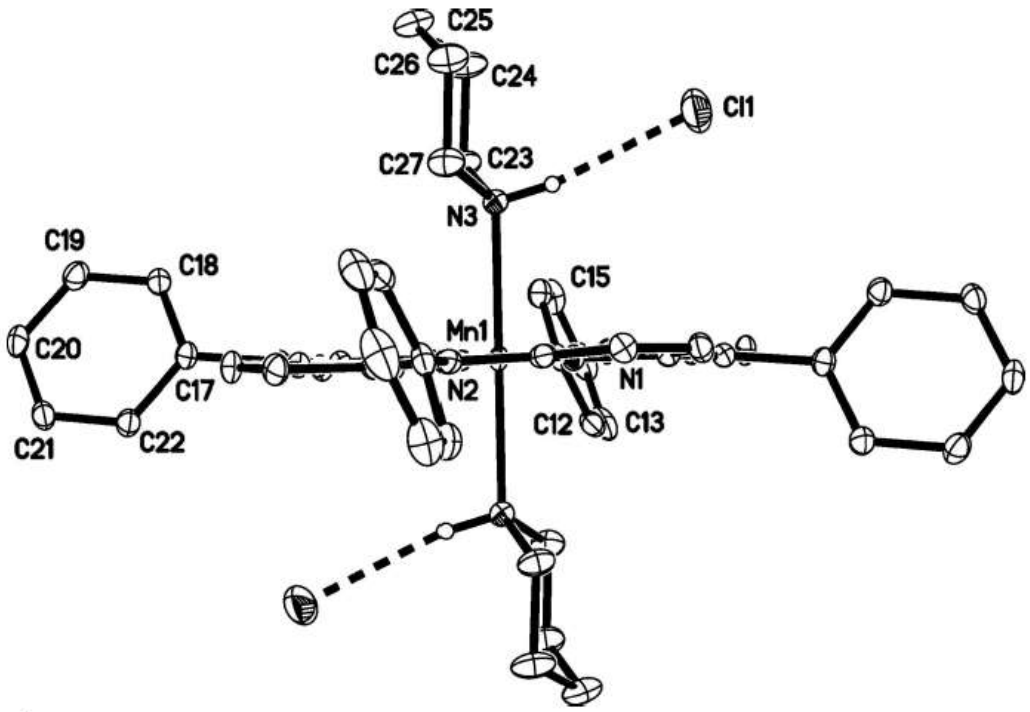

Figure 5.3 A view of the $[Mn(TPP)(pip)_2]^+$ cation parallel to the porphyrin plane. The chloride counter-anion is shown as Cl1. The second chloride, generated by 1 symmetry, is the counter-anion for the disordered piperidinium cation (not shown), which was removed by SQUEEZE. Only H atoms involved in hydrogen bonding to the chloride anion are shown. Displacement ellipsoids are drawn at the 50% probability level. Only the atoms of the asymmetric unit have been labeled as the molecule lies on a center of symmetry.

5.2.3 Crystal Structure of $[Mn(TPP)Cl(py)]^+$ (III)

Figure 5.4 shows a displacement ellipsoid plot of [Mn(TPP)Cl(py)], (III); the bond lengths and angles are given in Table 2. The Mn—N bond lengths in the porphyrin ring system range between 2.0025 (12)° and 2.0124 (12) Å , the distance to the bound pyridine N atom (Mn1—N5) is longer at 2.4203 (12) Å , and the Mn1—Cl1 distance is 2.4693 (4) Å . The angle defined by (pyridine)N5—Mn1—Cl1 is 175.43 (3). In this complex, the porphyrin ring is significantly nonplanar, the dihedral angle between the previously defned sets of planes are 19.66 (3)° and 21.66 (4)°, which leads to the bowl-shaped arrangement of the porphyrin in which the coordinated pyridine molecule resides. The dihedral angles between the planes of the core and the planes of the phenyl groups are again given in Table 5.2. The large phenyl group dihedral angles [ranging from 60.40 (4)° to 74.79 (3)°] lead to the criss-cross arrangement of the phenyl groups seen in Figure 5.4. The structure of another crystal form of this complex, namely chloro–α,β,γ,δ-tetraphenylporphyrinato–pyridine–manganese(III), [Cl(py)MnTPP], as a benzene solvate, is known.[29] Despite the differences in the solvents of crystallization, one benzene molecule versus two molecules of pyridine here, a comparison of the bond lengths and angles of the two structures (Table 5.2) shows that there are only very slight differences in the overall structure.

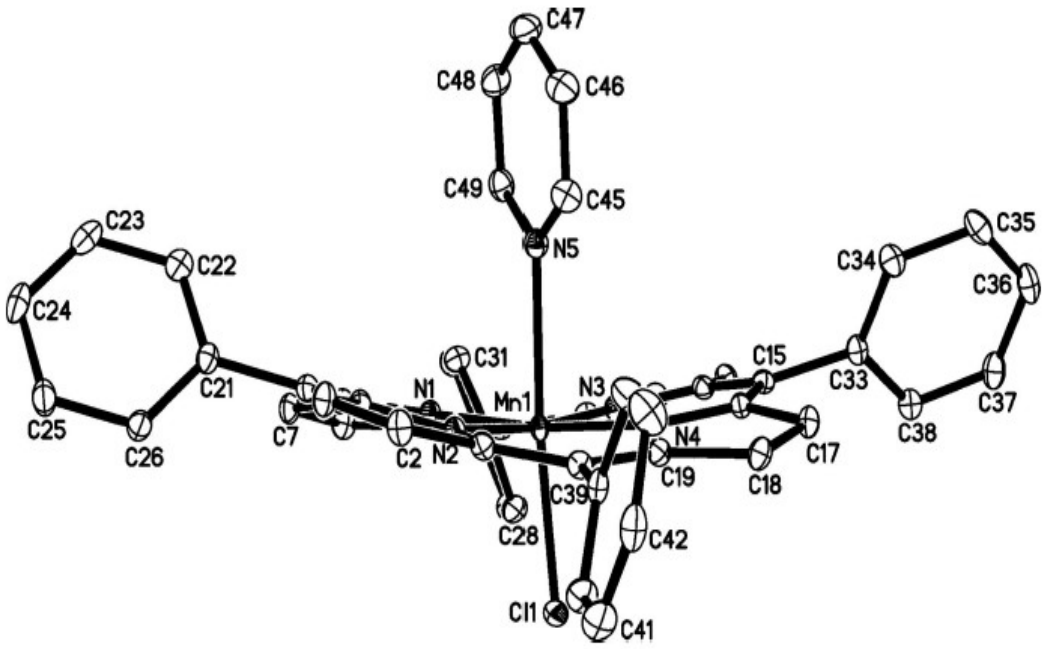

Figure 5.4 A view of the $[Mn(TPP)Cl(py)]^+$ cation parallel to the porphyrin plane. H atoms have been omitted for clarity and displacement ellipsoids are shown at the 40% probability level.

5.2.4 Crystal Structure of $[Mn(TPP)(DABCO)Cl]^+$ (IV)

The structure of the DABCO complex [Mn(TPP)Cl (DABCO)]*(DABCO)*(toluene)*0.25H_2O], is shown in Figure 6.5, where the numbering of some of the atoms are given. The metal–ligand distances in the porphyrin system are given in Table 5.2. Interestingly, the Mn1—N5 distance, involving the N atom of the DABCO molecule, is 2.612 (3) Å , which is much longer than the metal-to-N bond lengths in the other three molecules; it is also much longer that the Mn1—Cl1 distance of 2.4253 (9) Å. This just means that the DABCO N atom is only very weakly bonded to the Mn1 ion. In this structure, there are three molecules of crystallization [a molecule of DABCO, a molecule of toluene (the crystallizing solvent), and 0.25 molecules of H_2O], which sit in the large voids between the MnTPP complexes.

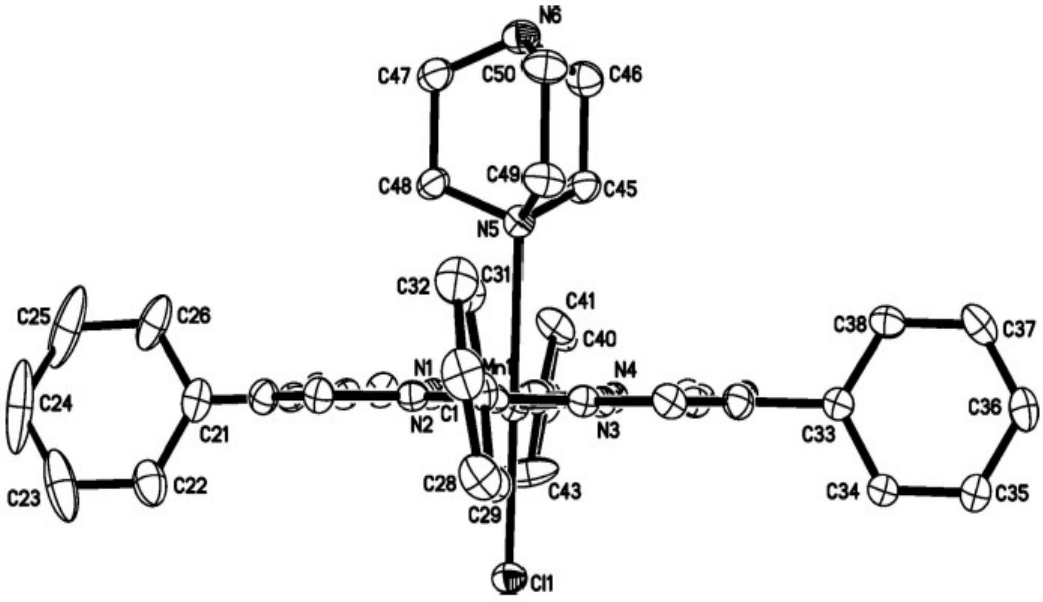

Figure 5.5 A view of the $[Mn(TPP)(DABCO)Cl]^+$ cation parallel to the porphyrin plane. H atoms have been omitted for clarity and displacement ellipsoids are shown at the 40% probability level.

Table 5.1 Experimental details

	(I)	(II)	(III)	(IV)
Crystal data				
Chemical formula	$[Mn(C_{44}H_{28}N_4)(C_3H_4N_2)_2]$-Cl·2$CHCl_3$	$[Mn(C_{44}H_{28}N_4)(C_5H_{11}N)_2]$-Cl	$[Mn(C_{44}H_{28}N_4)Cl$-$(C_5H_5N)]\cdot 2C_5H_5N$	$[Mn(C_{44}H_{28}N_4)(C_6H_{12}N_2)]$-Cl·$C_6H_{12}N_2$·$C_7H_8$·-0.25$H_2O$
M_r	1077.99	873.39	940.39	1023.58
Crystal system, space group	Triclinic, $P\overline{1}$	Triclinic, $P\overline{1}$	Triclinic, $P\overline{1}$	Triclinic, $P\overline{1}$
Temperature (K)	100	100	100	100
a, b, c (Å)	11.3475 (2), 14.2479 (3), 16.4138 (4)	10.5211 (1), 11.9123 (1), 12.6355 (1)	11.0499 (1), 12.1051 (1), 18.5362 (2)	11.4402 (2), 13.4019 (3), 18.6407 (4)
α, β, γ (°)	92.510 (1), 99.529 (1), 108.699 (1)	66.1342 (5), 78.3107 (5), 89.5778 (6)	90.177 (1), 90.324 (1), 110.537 (1)	95.774 (1), 92.199 (1), 113.630 (1)
V (Å^3)	2465.63 (9)	1413.24 (2)	2321.76 (4)	2595.35 (9)
Z	2	1	2	2
Radiation type	Cu $K\alpha$	Cu $K\alpha$	Cu $K\alpha$	Cu $K\alpha$
μ (mm^{-1})	6.03	3.04	3.22	2.95
Crystal size (mm)	0.43 × 0.31 × 0.22	0.48 × 0.26 × 0.24	0.30 × 0.26 × 0.24	0.24 × 0.22 × 0.18
Data collection				
Diffractometer	Bruker SMART CCD APEXII area-detector	Bruker SMART CCD APEXII area-detector	Bruker SMART CCD APEXII area-detector	Bruker SMART CCD APEXII area-detector
Absorption correction	Numerical (*SADABS*; Krause *et al.*, 2015)	Numerical (*SADABS*; Krause *et al.*, 2015)	Numerical (*SADABS*; Krause *et al.*, 2015)	Numerical (*SADABS*; Krause *et al.*, 2015)
T_{min}, T_{max}	0.168, 0.447	0.406, 0.572	0.501, 0.653	0.540, 0.737
No. of measured, independent and observed [$I > 2\sigma(I)$] reflections	23350, 8162, 7785	13568, 4750, 4719	21813, 7797, 7543	24215, 8538, 6596
R_{int}	0.027	0.019	0.032	0.038
$(\sin\theta/\lambda)_{max}$ (Å^{-1})	0.595	0.606	0.604	0.596
Refinement				
$R[F^2 > 2\sigma(F^2)]$, $wR(F^2)$, S	0.043, 0.111, 1.03	0.045, 0.115, 1.04	0.028, 0.077, 1.08	0.064, 0.180, 1.07
No. of reflections	8162	4750	7797	8538
No. of parameters	614	286	614	668
No. of restraints	0	0	0	12
H-atom treatment	H-atom parameters constrained	H-atom parameters constrained	H-atom parameters constrained	H-atom parameters constrained
$\Delta\rho_{max}$, $\Delta\rho_{min}$ (e Å^{-3})	1.24, −1.03	0.70, −1.00	0.25, −0.31	1.30, −0.68

Computer programs: *APEX2* (Bruker, 2006), *SAINT* (Bruker, 2005), *SHELXT2014* (Sheldrick, 2015*a*), *SHELXL2014* (Sheldrick, 2015*b*) and *SHELXTL* (Sheldrick, 2008).

Table 5.2 Comparison of bond lengths and angles for structures (I)–(IV) and associated literature.

	(I)	(II)	(III)	(IV)	MnClTPP (Boucher, 1972)	MnClTPP-py (Kirner & Scheidt, 1975)
Porphyrin angles (°)						
N1—Mn1—N3	179.75 (9)		173.58 (5)	173.4 (1)	166.9 (3)	172.8 (2)
N2—Mn1—N4	178.75 (8)		173.32 (5)	172.8 (1)	161.7 (3)	173.6 (2)
N1—Mn1—N1A		180.00 (15)				
N2—Mn1—N2A		180.00 (11)				
Ligand–Mn1–ligand angles (°)						
N5—Mn1—N7	178.65 (7)					
N3—Mn1—N3A		180.00 (11)				
N5—Mn1—Cl1			175.43 (3)	179.41 (6)		175.5 (1)
Ruffle angles (°)						
C1→C5—N1—C15→C20—N4						
C5→C9—N2—C10→C15—N3	5.64 (5)		19.66 (3)	1.63 (9)		
C5→C9—N2—C10—C11A→C5A—N1A						
C5→C1—N1—C10—C10A→C5A—N2A		0.00 (4)				
C20—C1→C4—N1—C5→C10—N2						
C10→C14—N3—C15→C20—N4	6.79 (5)		21.66 (4)	0.42 (7)		
C10A—C1→C4—N1—C5→C10—N2						
C10—C1A→C4A—N1A—C5A→C10A—N2A		0.00 (0)				
'Swayback' angles (°)						
C27—C10—Mn1						
C39—C20—Mn1	1.64 (9)		6.34 (7)	3.0 (2)		
C17—C10—Mn1						
C17A—C10A—Mn1		0.00 (6)				
C11—C5—Mn1						
C11A—C5A—Mn1		0.00 (6)				
C21—C5—Mn1						
C33—C15—Mn1	6.27 (9)		3.07 (8)	1.78 (4)		
Phenyl angles to porphyrin ring (°)						
C21→C26	66.87 (7)		60.40 (4)	72.61 (8)	54.2	59.8
C27→C32	88.75 (7)		67.95 (3)	80.6 (1)	123.5	79.1
C33→C38	77.94 (7)		61.72 (4)	79.51 (8)	49.7	69.1
C39→C44	64.48 (8)		74.79 (3)	80.29 (11)	77.4	72
C11→C16		70.13 (7)				
C17→C22		64.49 (6)				
Mn1-to-ligand distances (Å)						
Mn1—N1	2.018 (2)	2.0199 (17)	2.0124 (12)	2.022 (3)	1.999 (7)	2.022 (4)
Mn1—N2	2.025 (2)	2.0164 (17)	2.0060 (12)	2.026 (3)	2.0212 (7)	2.006 (4)
Mn1—N3	2.025 (2)	2.3704 (17)	2.0083 (12)	2.007 (2)	1.992 (7)	2.010 (3)
Mn1—N4	2.015 (2)		2.0025 (12)	2.019 (3)	2.022 (7)	2.000 (4)
Mn1—N5	2.285 (2)		2.4203 (12)	2.612 (3)		2.444 (4)
Mn1—N7	2.284 (2)					
Mn1—Cl1			2.4693 (4)	2.4253 (9)	2.363 (3)	2.467 (1)
Mn-atom displacement from the N1/N2/N3/N4 plane (Å)	−0.0075 (8)	0.0000 (0)	−0.0913 (5)	−0.097 (1)	0.27	0.145
Plane N1/N2/N3/N4/Mn1 *versus* Cl1 angle (°)			93.77 (6)	93.44 (14)	4.7 (175.3)	
Plane N1/N2/N3/N4/Mn1 *versus* N5 angle (°)			86.73 (8)	86.56 (18)		

Symmetry code: (A) $x, y + 1, z$.

5.2.5 Binding Constants

Upon the addition of the pyridine and DABCO ligands through titration to Mn(TPP)Cl in chloroform, the intensity of the Soret band decreased along with its broadening, as shown in Figure 5.6(a) and 5.6(b). We attribute the spectral changes to the formation of the monoamine coordination complexes, [Mn(TPP)(L)]Cl, where L is a nitrogenous ligand.[10] One isosbestic point was observed for the pyridine complex at 462 nm, and two for the DABCO complex (469 and 490 nm). We estimate binding constants for these complexes using equation (1) and find β_{py} = 3.6 +/- 0.8 and β_{DABCO} = 5.8 +/- 1.7.

$$p\beta = \log\left(\frac{A-A_{0PL}}{A_{0P}-A}\right) + \log[L] \quad (1)$$

where β – binding constant, pβ = -logβ, A – absorption at 479 nm at concentration [L] of the ligand, A_{0PL} – absorption of the MnClTPPL complex at 479 nm, and A_{0P} – absorption of the MnClTPP complex at 479 nm. The imidazole complex is known to be doubly ligated;[10] therefore, the imidazole complex has two equivalence points: the first at a ligand concentration of ~4.25 x10^{-3} M and the second at 2.5 x10^{-2} M, attributed to the first and second binding interactions of imidazole. Estimation of the binding constants for this complex using this titration method is not trivial because the close proximity of the two equivalence points leads to binding constants that are indistinguishable within error. However, it has been reported that the binding constants for the imidazole complex, in a similarly noncoordinating solvent, toluene, are β_1 = 1.76 x10^2 and β_2 = 3.57 x10^2.[10] These results show that imidazole has a much higher affinity for forming bis-coordinated complexes in solution than either pyridine or DABCO. Binding studies for the piperidine complex are not possible by monitoring the titration by UV–Vis spectroscopy due to the peak shift caused by the immediate reduction of Mn(III) to Mn(II) upon piperidine

addition. Piperidine reduction of the Mn(TPP)Cl complex to Mn(II) was confirmed by a spectrophotometric experiment where a 1 M piperidine solution was introduced to the Mn complex. This is indicated by an intensity increase and shift of the Soret band peak maximum from 479 to 443 nm.[26] This Mn(II) complex is stable in solution in excess piperidine; however, upon isolation in the solid state, the complex oxidizes back to the Mn(III) state, as evidenced by UV–Vis diffuse reflectance. Crystallization led to the isolation of the Mn(III) bis-piperidine porphyrin complex reported here.

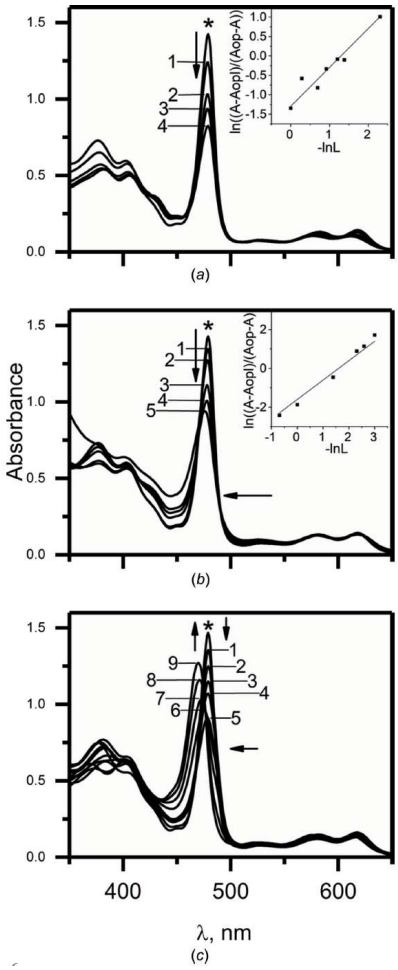

Figure 5.6 UV–Vis absorption spectra of [Mn(TPP)]Cl in chloroform (*) upon the addition of (a) pyridine, forming complex [Mn(TPP)Cl(py)], (b) DABCO, forming complex [Mn(TPP)Cl(DABCO)], and (c) imidazole, forming complex $[Mn(TPP)(im)_2]Cl$. The inset graphs show the linear plot from which the binding constants for pyridine and DABCO are calculated.

5.2.6 X-ray Absorption Spectroscopy

The XAS data for the manganese porphyrin complexes and MOFs are presented in Figure 5.7. The XANES spectra for the Mn-porphyrin systems each contain pre-edge features with significant intensity around 6541 eV. As mentioned earlier in this thesis, XANES edge energies provide information on oxidation state and the spin states as well as local geometry. All the manganese porphyrin systems presented here are in the +3 oxidation state and high-spin. Therefore any spectral differences in the pre-edge should provide the most insight into the local geometry of the Mn porphyrin metal center. The MnClTPP reference complex and MnClPCN222-act MOF samples show an almost identical spectrum with a pre-edge at 6541eV. The MnClPCN222-ace (acetone-soaked MOF) has a noticeably less intense pre-edge feature at 6541eV indicating that acetone is a weakly coordinating/interacting guest solvent. The $MnTPPIm_2Cl$ reference complex has a lower intensity split pre-edge feature. The peak maxima of the split pre-edge are at 6540.3 eV (more intense) and 6542.8 eV (lesser intensity). The $MnTPPpip_2Cl$ reference complex shows the same spectral shape in the pre-edge region as that of $MnTPPIm_2Cl$, with a slight difference in intensity. Complexes MnClTPP-py and MnClTPP-dabco have a complicated and slightly unresolved pre-edge feature at ~6540.6eV that lies in between that of $MnTPPIm_2Cl$/$MnTPPpip_2Cl$ and MnClTPP complexes. MnClTPP-py has a pre-edge spectral shape that is similar to the bis-ligated complexes but varies in the intensity ratio of the two pre-edge features. The dabco complex has a broader pre-edge, including some unresolved spectral features that contribute to the intensity. The MOF samples, treated with py and dabco are nearly identical and have a major pre-edge feature at ~6540.8eV and a second small feature at ~6542.9eV. The imidazole-treated MOF

sample has a very similar pre-edge to the py and dabco samples, differing only with respect to the intensity of the second smaller feature at ~6542.9eV. The MnClPCN222-pip MOF sample has one pre-edge feature of moderate intensity at ~6540.8 eV and some unresolved intensity at ~6542.9 eV.

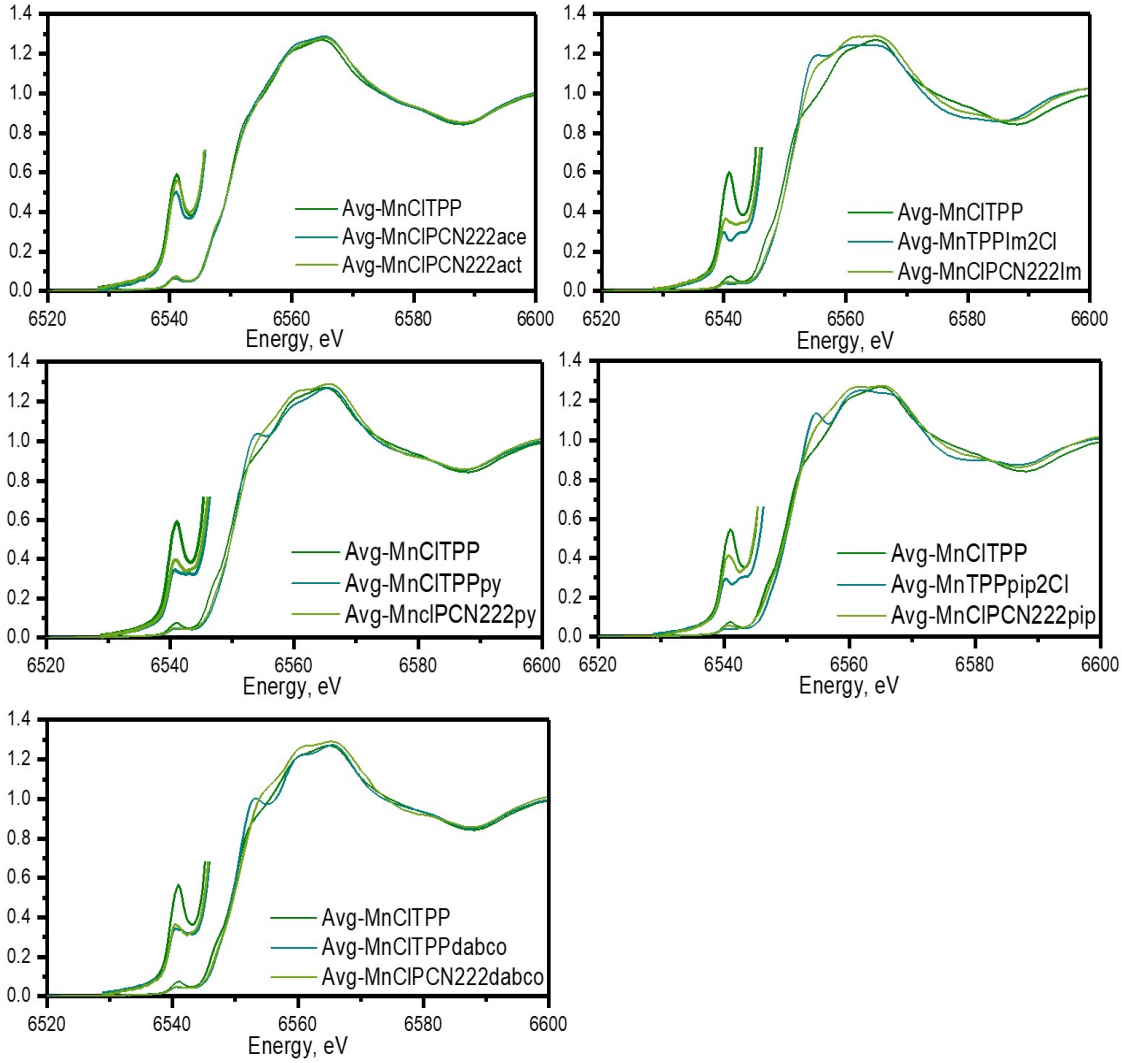

Figure 5.7 XANES for Mn reference complexes and Mn-porphyrin frameworks

5.3 Discussion

5.3.1 Crystal Structures & Binding Constants

The catalytic activity of metalloporphyrins in various environments is attributed to the porphyrin metal center and its ability to perform redox chemistry and coordinate different axial ligands. Whether incorporated in protein environments or in porous solid-state materials, like MOFs,[39-40] the geometry and accessibility of the metalloporphyrin sites afforded by those architectures also plays a crucial role in dictating the binding affinity of substrates. To better understand the binding and reactivity in these environments for Mn-based sytems, we need to first determine the coordination chemistry and structures of the manganese(III) porphyrins in solution and in the solid state for comparison. The structures presented here (Scheme 5.1) provide evidence of the nonplanarity of the porphyrin ring system, which varies according to the individual nitrogenous ligands attached at the 5th and/or 6th positions around the metal center. The average equatorial Mn—N distance (2.0104 Å) of the mixed-ligated complexes is in agreement with that reported for the five-coordinated Mn(TPP)Cl (in chloroform solvate), which is 2.01 Å, and only slightly shorter than the average equatorial Mn—N bond length of 2.0199 Å for the bis-ligated complexes reported here, and comparable to the six-coordinated Mn(III) high-spin complex $N_3(CH_3OH)$MnTPP reported at 2.031 Å.[27,41] The axial Mn—Cl bond lengths for the py [2.4693 (4) Å] and DABCO [2.4253 (9) Å] complexes are much longer than that of the starting material Mn(TPP)Cl (2.363 Å). The elongation of this bond was noted previously for the py complex;[29] it is confirmed in this py complex and further substantiated with the study of the DABCO complex. Furthermore, the axial Mn—N bonds of these two complexes are longer than all other

Mn bond lengths reported both in this article and in all the associated literature we have found. It has been suggested that the rate-determining step in the reaction of Fe(TPP)Cl and two imidazoles is the chloride ionization from intermediate Fe(TPP)(Him)Cl to form $Fe(TPP)(Him)_2^+ * Cl^-$.[42] The ionization of the Cl^- ion seems to be greatly accelerated through hydrogen bonding from the free imidazole. The authors found that hydrogen-bond donors, such as imidazole, account for the different rates observed compared to those of the nonhydrogen-bond donors, such as the alkylated imidazole N-MeIm.[43] This explanation could be extended in the case of our Mn(III) complexes to explain the axial binding behavior of the Lewis bases studied here. Both imidazole and piperidine are capable of the same type of distal hydrogen bonding to the likely intermediate, i.e. Mn(TPP)(HIm)Cl, analogous to the Fe intermediate reported for the iron porphyrins,[42-43] whereas both DABCO and py are unlikely to emulate this behavior. This is one possible explanation for the replacement of the axial chloride for a second Lewis base in the sixth position in the piperidine and imidazole complexes, and also why Cl remains in the other two.

5.3.2 X-ray Absorption Spectroscopy

Literature precedent for Mn porphyrin complexes of this type indicate that manganese porphyrins prefer to be in the high-spin state[19], which is further confirmed by the edge shift observed in the XANES spectra in Figure 5.7. With all Mn porphyrin systems studied here in the +3 oxidation state, spectral differences in the pre-edge can be attributed to the different coordination geometry of each system. When comparing each MOF system with its analogous reference complex, we see a broad degree of variation

between the systems studied. For example, the dabco-soaked framework MnCl-PCN-222-dabco and its analogous reference complex, MnClTPPdabco, have edge and pre-edge features that lay essentially on top of eachother, indicating similar geometry between the reference complex and the MOF, while the XAS spectra for MnTPPpip$_2$Cl and MnCl-PCN-222-pip have very different spectral features. In this former, the pre-edge is split into two distinct features of low intensity, while the later has one pre-edge feature of medium intensity. This may be an indication of the influence of the PCN-222 pore topology, with the larger guest molecules unable to fully fit and therefore coordinate in the 10Å trigonal pores. Another possibility is that once confined in the rigid MOF structure, porphyrin-ring strain prevents full coordination of the guest molecules. A more likely situation however is that the differences in intensity and the degree of splitting of the pre-edge feature indicate that we have a mixture of penta- and hexa- coordination at the manganese metal centers. Ongoing TD-DFT calculations on both the reference complexes and theoretical mixed axial coordination models should help clarify the binding behavior of the guest species inside of the MOF.

5.4 Conclusion

Of the four Mn(III) porphyrin structures reported, two of the structures contain bis-ligated Lewis bases (piperidine and imidazole). These structures follow the observations documented for iron porphyrins of this type with one unexpected deviation: piperidine does not reduce the manganese(III) center in the solid state (as it does in solution and as it does in both solution and the solid state for analogous Fe(III) complexes). As expected for manganese, imidazole bis-coordination does not initialize a

spin-flip from high-spin to low-spin manganese(III). The other two structures reported have metal-bound chloride ions and singly ligated Lewis bases, py, and DABCO. For these complexes, we hypothesize that a lack of hydrogen bonding from the free Lewis base to the intermediate [Mn(TPP)(L)]Cl (where L = py or DABCO) could be the cause. This type of distal hydrogen bonding to the reaction intermediate has been found to facilitate and increase the rate of reaction in analogous iron porphyrins, producing the final [Mn(TPP)(L_2)]Cl product. The reported Mn(III) structures will serve as benchmarks for Mn porphyrins in both natural and synthetic environments and may help elucidate structure mediated chemical interactions.

Additionally, preliminary XAS data suggests a complicated coordination environment in the guest-soaked Mn porphyrin frameworks. This is most likely due to a combination of factors such as pore size, MOF rigidity, and the preference for manganese porphyrins to stay in the high-spin state. Unlike the other MOF systems studied with other metal porphyrin linkers, manganese porphyrin MOFs seem to deviate the most in terms of their coordination behavior when compared to their analogous reference complexes. On-going TD-DFT calculations should provide us with some insight on this interesting behavior.

5.5 Experimental

5.5.1 Synthesis and crystallization

TPP, Mn(TPP)Cl, [Mn(TPP)($im)_2$]Cl*2$CHCl_3$, [Mn(TPP)(pip)2]Cl, [Mn(TPP)Cl(py)]*2(py), and [Mn(TPP)Cl(DABCO)]*(DABCO)*(toluene)*0.25H_2O

were synthesized according to the methods described below. All other reagents were purchased commercially and used without further purification.

Synthesis of 5,10,15,20-tetraphenylporphyrin (TPP). TPP was made following the literature procedure of Adler et al.[35] Pyrrole (5.6 ml, 80 mmol) was added to boiling propionic acid. Benzaldehyde (8 ml, 78 mmol) was then added to the reaction mixture. The reaction continued for 40 min and was then allowed to cool to room temperature. Violet crystals were collected by filtration, washed with methanol and water, and dried in a vacuum oven for 2 h (yield 20%).

Synthesis of (5,10,15,20-tetraphenylporphyrinato)-manganese(III) chloride, Mn(TPP)Cl. This precursor was prepared according to the literature procedure of Feng et al.[18] TPP (1.0 g, 1.6 mmol) was dissolved in DMF and MnCl2 (3.0 g, 24 mmol) was added. The reaction was refluxed overnight, then stopped and allowed to cool to room temperature. Water was added to the reaction mixture and a green powder was filtered off. The resulting powder was dissolved in chloroform and washed with 1 M HCl solution (x3) and water (x2). The resulting organic layer was dried over anhydrous sodium sulfate for 1 h (yield 68%).

Synthesis of bis(imidazole)(5,10,15,20-tetraphenylporphyrinato)-manganese(III) chloride chloroform disolvate, $[Mn(TPP)(im)_2]Cl*2CHCl_3$, (I). Complex (I) was synthesized according to a modified literature procedure for the preparation of a similar iron(III) complex, i.e. [Fe(TPP)(HIim)2]Cl.[36] Mn(TPP)Cl (50 mg, 0.071 mmol) was mixed with

imidazole (20 mg, 0.30 mmol) in chloroform (4 ml) in a 20 ml scintillation vial. A 2:1 (v/v) hexane–chloroform solution was added (15 ml), utilizing the layering technique, to the Mn(TPP)Cl-imidazole mixture. The resulting mixture was left to infuse and crystallize for a minimum of 3 d. The resulting dark-green crystals were filtered off and washed with hexanes (yield 95%).

Synthesis of bis(piperidine)(5,10,15,20-tetraphenylporphyrinato) manganese(III) chloride, [Mn(TPP)$(pip)_2$]Cl, (II). Mn(TPP)Cl (50 mg, 0.071 mmol) was dissolved in piperidine (4 ml). Utilizing the layering technique, octane was added to the Mn(TPP)Cl–piperidine mixture. The resulting mixture was left to infuse and crystallize for a minimum of 3 d. The resulting dark-green crystals were filtered off and washed with octane (yield 48%).

Synthesis of chlorido(pyridine)(5,10,15,20-tetraphenylporphryinato)manganese(III) pyridine disolvate, [Mn(TPP)Cl(py)]*2(py), (III). The synthesis of (III) was performed by dissolving Mn(TPP)Cl (50 mg, 0.071 mmol) in pyridine (4 ml). Utilizing the same layering technique as was applied to complex (I), octane was added to the Mn(TPP)Cl–pyridine mixture. The resulting mixture was left to infuse and crystallize for a minimum of 3 d. The resulting dark-green crystals were filtered off and washed with octane (yield 41%).

Synthesis of chlorido(1,4-diazabicyclo[2.2.2]octane)(5,10,15,20-tetraphenylporphyrin)manganese(III)–1,4-diazabicyclo[2.2.2]octane–toluene–water

(4/4/4/1), [Mn(TPP)Cl(DABCO)]*(DABCO)*(toluene)*0.25H2O, (IV). The synthesis of complex (IV) was performed by dissolving Mn(TPP)Cl (50 mg, 0.071 mmol) in chloroform (2 ml). A saturated DABCO–chloroform solution (3 ml) was added. Utilizing the layering technique, octane was added to the Mn(TPP)Cl-DABCO mixture. The resulting mixture was left to infuse and crystallize for a minimum of 3d, resulting in dark-green crystals (yield 90%).

Mn-MOF samples were prepared analogous to methods described in Chapter 4 of this thesis.

5.5.2 Refinement

Crystal data, data collection, and structure refinement details are summarized in Table 5.1. All the H atoms for structures (I)–(IV) were found in electron-density difference maps. For all structures, the aromatic H atoms were placed in geometrically idealized positions and constrained to ride on their parent C atoms, with C—H = 0.95 Å and U_{iso}(H) = 1.2Ueq(C). For (II) and (IV), the methylene H atoms were fixed at distances of 0.99 Å. For (II), electron-density peaks suggested one mixed-occupancy piperidine/piperidinium chloride moiety of crystallization in the asymmetric unit, or two molecules per formula unit (one protonated, one not), situated in a cavity around a center of symmetry, plus a water molecule. The piperidine/piperidinium moiety was disordered over at least two orientations; however, attempts to model this were difficult. Accordingly, the SQUEEZE routine[37] of PLATON[38] was used to account for the

diffuse/disordered moieties, giving an electron count of 112 in a volume of 380 e $Å^{-3}$, consistent with one piperidine molecule, one piperidinium chloride unit and one water molecule per formula unit, i.e. $[Mn(TPP)(pip)_2]Cl*[C5H_{12}N^+Cl^-]*(pip)*H_2O$. By measuring the density of this complex by the floatation method using hexane and carbon tetrachloride, we got 1.290 Mg m^{-3}. This allows us to calculate the molecular weight of the complete material and this is 1097.8 $g*mol^{-1}$, leading to the above formulation for the disordered complex.

5.5.3 Spectrophotometric titrations for the determination of binding constants

A stock solution of [Mn(TPP)]Cl was prepared by dissolving the complex (7 mg) in chloroform (50 ml, $2x10^{-4}$ M). Aliquots of 0.4 ml were transferred into 4 ml volumetric flasks and each was diluted to 4 ml with solutions of a ligand with different concentrations (from 1 _ $10x^4$ to 4 M). Titration solutions were subsequently monitored by UV–Vis absorption spectroscopy (at 479 nm, where the most drastic changes were observed) using a Cary–Varian UV–Vis–NIR spectrophotometer. Binding constants (β) for the axial ligand L [where L is either pyridine (py) or DABCO] were calculated using equation 1.

5.5.4 X-ray Absorption Spectroscopy

X-ray absorption data were collected at the Mn K-edge (6539 eV) in transmission mode at Beamline 6BM at NSLS II using a 3-pole wiggler source and an optical system composed of a paraboloid collimating mirror, Si(111) face monochromator, a toroidal focusing mirror, and a flat harmonic rejection mirror. The monochromatized beam was

generated with a 2 × 1 mm spot size and a resolving power of 1.3×10^{-4} ΔE/E. The incident (I_0), transmitted (I_t), and reference (I_r) beam intensities were all measured by 15 cm ionization chambers filled with 100% N_2 gas. Manganese foil was used as the reference for energy calibration. Samples were packed in an aluminum sample holder and sealed with Kapton tape.

5.6 References

[1] Momenteau, M. & Reed, C. A., *Chem. Rev.,* **1994,** *94*, 659–698.

[2] Kadish, K., Smith, K. & Guilard, R., *In The Porphyrin Handbook: Inorganic, Organometallic and Coordination Chemistry,* **1999b**, *Vol. 3*. New York: Academic Press.

[3] Calvin, M., *Pure Appl. Chem.* **1965,** *15*, 1–10.

[4] Gunter, M.-J. & Turner, P., *Coord. Chem. Rev*. **1991**, *108*, 115–161.

[5] Boucher, L. J. & Garber, H. K., *Inorg. Chem.* **1970,** *9*, 2644–2649.

[6] Collman, J. P., Kodadek, T., Raybuck, S. A. & Meunier, B., *Proc. Natl Acad. Sci. USA,* **1983**, *80*, 7039–7041.

[7] Mohajer, D., Karimipour, G. & Bagherzadeh, M., *New J. Chem.* **2004,** *28*, 740–747.

[8] Zhou, X.-T., Ji, H.-B., Xu, J.-C., Pei, L.-X., Wang, L.-F. & Yao, X.-D., *Tetrahedron Lett.* **2007,** *48*, 2691–2695.

[9] Li, Y., Zhou, X., Chen, S., Luo, R., Jiang, J., Liang, Z. & Ji, H., *RSC Adv.,* **2005,** *5*, 30014–30020.

[10] Yuan, L. C. & Bruice, T. C., *J. Am. Chem. Soc.* **1986,** *108,* 1643–1650.

[11] Gangopadhyay, S., Ali, M. & Banerjee, P., Coord. Chem. Rev. **1994,** *135–136*, 399–427.

[12] Tollari, S., Fumagalli, A. & Porta, F., *Inorg. Chim. Acta,* **1996**, *247*, 71–74.

[13] Yuan, Q.-Y., Zhou, X.-T. & Ji, H.-J., *Catal. Commun.* **2010,** *12*, 202–206.

[14] Zhou, X.-T., Ren, Q.-G. & Ji, H.-B., *Tetrahedron Lett.* **2012**, *53*, 3369–3373.

[15] Hod, I., Sampson, M. D., Deria, P., Kubiak, C. P., Farha, O. K. & Hupp, J. T., *ACS Catal.* **2015**, *5,* 6302–6309.

[16] Betard, A. & Fischer, R. A., *Chem. Rev.* **2012**, *112*, 1055–1083.

[17] Kadish, K., Smith, K. & Guilard, R., *In The Porphyrin Handbook: Phthalocyanines: Properties and Materials,* **2003**, *Vol. 17*.New York: Elsevier Science USA.

[18] Feng, D., Gu, Z.-Y., Li, J.-R., Jiang, H.-L., Wei, Z. & Zhou, H.-C., *Angew. Chem. Int. Ed.* **2012**, *51*, 10307–10310.

[19] Kadish, K., Smith, K. & Guilard, R., *In The Porphyrin Handbook: Inorganic, Organometallic and Coordination Chemistry,* **1999b**, *Vol. 3*. New York: Academic Press.

[20] Meunier, B., *Chem. Rev*. **1992**, *92*, 1411–1456.

[21] Hanson, L.-K., *Int. J. Quantum Chem. Quantum Biol. Symp.* **1979**, *6*, 73–87.

[22] Castro, C.-E., *Bioinorg. Chem.* **1974**, *4*, 45–65.

[23] Collman, J., *In Oxygen Binding to Heme Proteins and Their Synthetic Analogs,* **1980**, *Vol. 2*. New York: Wiley.

[24] Ricard, D., L'Her, M., Richard, P. & Boitrel, B., *Chem. Eur. J.,* **2001,** *7*, 3291–3297.

[25] Ma, C., Xiang, D., Zhai, C., Che, J., Liu, A.,Wang, J. & Hu, W., *Org. Lett.,* **2013,** *15,* 6140–6143.

[26] Boucher, L. J., *Coord. Chem. Rev.* **1972,** *7*, 289–329.

[27] Day, V. W., Stults, B. R., Tasset, E. L., Day, R. O. & Marianelli, R. S., *J. Am. Chem. Soc.* **1974**, *96*, 2650–2652.

[28] Gonzalez, B., Kouba, J., Yee, S., Reed, C., Kirner, J. F. & Scheidt, R., *J. Am. Chem. Soc.* **1975,** *97*, 3247–3249.

[29] Kirner, J. F. & Scheidt, R., *Inorg. Chem.* **1975,** *14*, 2081–2086.

[30] Jia, S., Jentzen, W., Shang, M., Song, X., Ma, J., Scheidt, W. R. & Shelnutt, J. A., *Inorg. Chem.* **1998**, *37*, 4402–4412.

[31] Duval, H., Bulach, V., Fischer, J. & Weiss, R., *Inorg. Chem.* **1999**, *38*, 5495–5501.

[32] Song, Y., Haddad, R. E., Jia, S., Hok, S., Olmstead, M. M., Nurco, D. J., Schore, N. E., Zhang, J., Ma, J., Smith, K. M., Gazeau, S., Pacaut, J., Marchon, J., Medforth, C. J. & Shelnutt, J. A., *J. Am. Chem. Soc.* **2005,** *127*, 1179–1192.

[33] Lever, A. B. P. & Gray, H.-B., Iron Porphyrins, Part II. Reading, MA: Addison–Wesle Publishing Company, **1983**.

[34] Berezin, B., Usp. Khim. **1980,** *49*, 2389–2417.

[35] Adler, A. D., Longo, F. R., Finarelli, J. D., Goldmacher, J., Assour, J. & Korsakoff, L., *J. Org. Chem.* **1967,** *32*, 476.

[36] Scheidt, W. R., Osvath, S. R. & Lee, Y. J., *J. Am. Chem. Soc.* **1987,** *109*, 1958–1963.

[37] Spek, A. L., *Acta Cryst*. **2015**, *C71*, 9–18.

[38] Spek, A. L., Acta Cryst. **2009,** *D65,* 148–155.

[39] Kucheryavy, P., Lahanas, N., Velasco, E., Sun, C. J. & Lockard, J. V., *J. Phys. Chem. Lett.* **2016**, *7*, 1109–1115.

[40] Kucheryavy, P., Lahanas, N. & Lockard, J. V., *Inorg. Chem.* **2018**, *57*, 3339–3347.

[41] Day, V. W., Stults, B. R., Tasset, E. L., Day, R. O. & Marianelli, R. S., *Inorg. Nucl. Chem. Lett.* **1975,** *11*, 505–509.

[42] Tondreau, G. A. & Sweigart, D. A., *Inorg. Chem.* **1984**, *23*, 1060–1065.

[43] Doeff, M. M. & Sweigart, D. A., *Inorg. Chem.* **1982**, *21*, 3699–3705.

Chapter 6. Study of imidazole diffusion and coordination into iron porphyrin metal-organic frameworks

6.1 Introduction

Metal-organic frameworks are known to have a wide variety of diffusion times based on their structure[1-7]. Diffusion processes within these frameworks may ultimately be the most important factor dictating the overall performance of the material for catalysis applications. Porphyrin-based metal-organic frameworks have recently demonstrated promising catalytic activity in a series of oxidation-reduction reactions in condensed solvent media.[8] The enhancement in catalytic performance is due to their porous nature which provides access to the higher density of active sites they possess. It is expected however, that despite the relatively large number of active sites in these and other MOFs, not all of them will be accessible to participate in catalytic reactions due to diffusion-limited processes. Surface barriers, organic side-reactions, and pore collapse are all possible culprits that may impact substrate diffusion within the frameworks.[9] Moreover, the role of the solvent in facilitating substrate diffusion is not well understood. Understanding these potential limitations will help determine their likely impact on overall catalytic function. Accurately measuring the diffusion of reactive guest species to the active sites within the MOFs is an important first step in addressing possible reaction site accessibility issues. To evaluate these diffusion processes, this chapter presents the results of a series of in-situ experiments on several MOF suspensions upon introduction of a guest molecule with known reactivity to provide insight to the percentage of metal centers in the MOF that are realistically involved in the catalytic cycle and therefore, given the kinetics of the catalytic reactions, elucidate whether it occurs at the reactive sites within the pores

of the framework or merely on the MOF surface. The investigation into the liquid phase diffusion process was studied in the iron porphyrin-based MOFs, FeCl-PCN222 and FeCl-PCN224 with imidazole and 1-methylimidazole guest species using in-situ X-ray absorption spectroscopy. This MOF and guest combination were chosen because imidazole is known to strongly coordinate to the iron porphyrin centers at the 5^{th} and 6^{th} axial positions, changing the spin state from Fe(III) high-spin to Fe(III) low-spin in the process. The suspended MOF particle sizes ranged from 60 nm to 5 μm for each MOF. XAS and XES experiments on model complexes confirm the formation of fully coordinated metal centers in both FeCl-PCN222 and FeCl-PCN224 MOFs after soaking for 24 h. This hard X-ray spectroscopy method also provides a convenient handle for studying the diffusion process due to its element-specific nature and ability to probe the bulk of solid-state material, unlike soft X-ray methods such as X-ray fluorescence (XRF) that are only surface-sensitive. Changes in pre-edge and edge positions in the XANES region can be measured with fast data collection strategies to monitor the diffusion process inside the pores of the MOF in real time. The reaction between the iron-porphyrin and imidazole/1-methylimidazole substrate is shown in scheme 6.1.

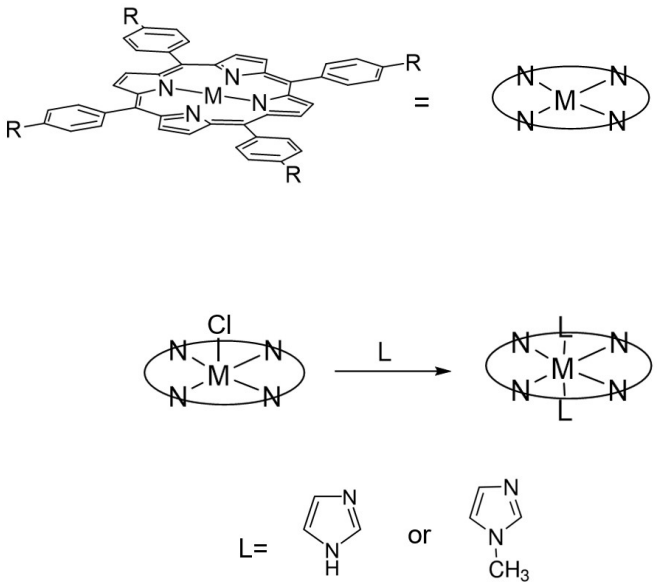

Scheme 6.1 Reaction of M-TPP (TPP=tetraphenylporphyrin, M=Fe) with a strongly coordinating ligand (imidazole or 1-methylimidazole).

6.2 Results and discussion

Transmission Fe K-edge XANES spectra for the reference complexes and MOFs are shown in Figure 6.1. The edge energies, as determined by the first inflection point are summarized in Table 6.1 (see Chapter 4 for details). XANES edge energies provide information on oxidation and the spin state of the absorbing atom. Moreover, the pre-edge features are also sensitive to metal oxidation and spin states as well as local geometry, with lower symmetry metal centers, such as C_{4v}, generally having more intense pre-edge features.[10] The pre-edge peak energies and intensities of the Fe(III) porphyrin-based MOFs (Figure 6.1) closely match those of the corresponding reference complexes.

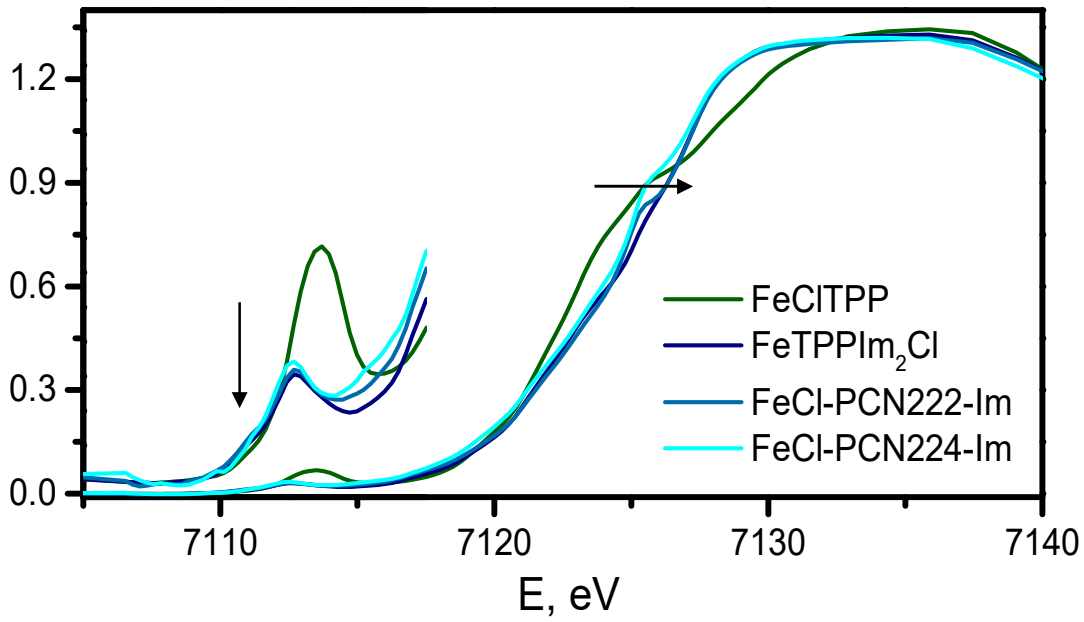

Figure 6.1 Normalized Fe K-edge XANES spectra with 10× magnification of the pre-edge region for solid-state reference complexes FeClTPP and $FeTPPIm_2Cl$ and MOFs FeCl-PCN222-Im, FeCl-PCN224-Im. Arrows indicate direction of changes that will me monitored.

Table 6.1 Electronic structure, local geometry, and XANES data for iron porphyrin reference complexes and imidazole-treated MOFs

	Oxidation state	Spin State	XANES	
			Pre-edge, eV	[a]Edge, eV
FeClTPP	+3	HS	7113.5	7122.3
$FeTPPIm_2Cl$	+3	LS	7112.5	7122.0
FeCl-PCN222-Im	+3	LS	7112.5	7122.0
FeCl-PCN224-Im	+3	LS	7112.5	7121.7

[a]Edge position determined from first inflection point.

Imidazole is known as a strongly binding ligand to the iron center in porphyrin environments.[11] Upon interaction with square-pyramidal Fe(III) porphyrin complexes, it has been found that one imidazole molecule binds to the open axial position, while the

second one substitutes the axial ligand, leading to the formation of hexacoordinated low-spin iron(III) centers. These differences in metal coordination and spin state cause obvious changes in the XAS spectra. Spectral changes are consistent for the $FeTPPIm_2Cl$ reference complex and imidazole-treated MOFs. Qualitative comparison of XANES spectra for these systems shows that all three possess a low intensity pre-edge feature at 7112.5 eV and an edge position at 7122.0 eV, which are highly consistent with those reported for low-spin Fe(III) octahedral complexes.[12] These drastic spectral differences, shown in Figure 6.1, therefore provide a convenient handle in assessing the diffusion of imidazole into the MOFs in real time. Since XAS is an element-specific technique that probes at the entire particle (not just surface iron atoms), this allows us to track specifically the changes at the iron porphyrin metal center as they coordinate imidazole, allowing us to potentially extract out relative diffusion rates. Based off the difference spectrum between FeCl-PCN-22X and FeCl-PCN-22X-Im, the largest difference in their spectra occurs on the rising edge, as shown in Figure 6.2, therefore we expected hypothesized that the in-situ spectroscopic changes to be most evident at this energy.

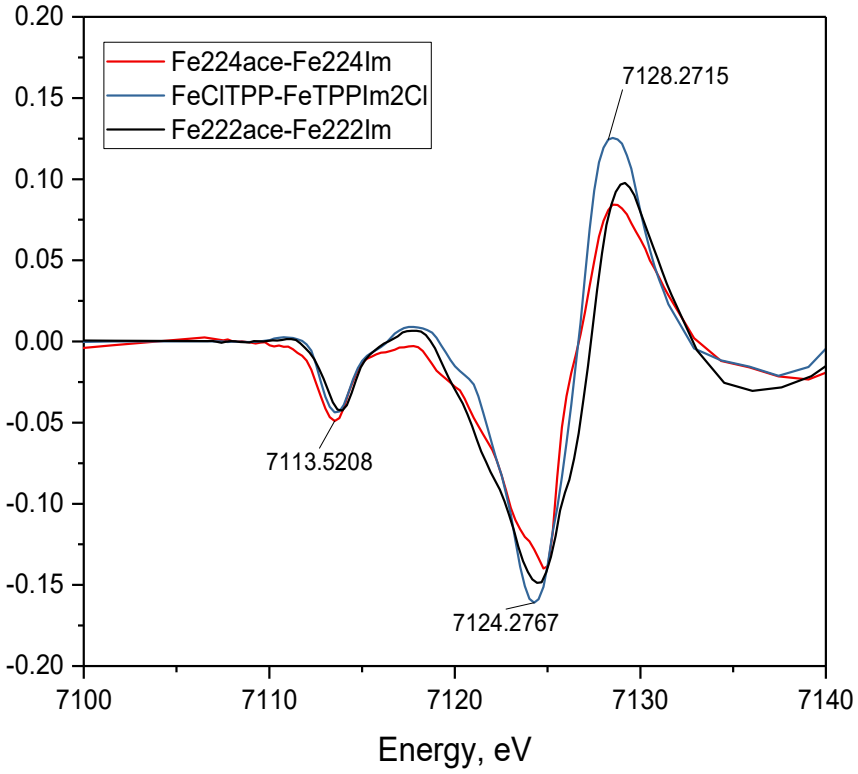

Figure 6.2 Difference spectrum of FeCl-PCN-224 and FeCl-PCN-224-Im, FeCl-PCN-222 and FeCl-PCN-222-Im, and corresponding reference complexes.

Figure 6.5 details the in-situ diffusion of imidazole into a FeCl-PCN-224 micron-sized MOF suspension. As shown in the spectra, the diffusion process as indicated by the spectral change associated with full imidazole-coordination to all iron(III) centers, was complete within the first few seconds upon injection. This surprisingly fast timescale proved to be beyond the limit of the beamline capabilities in terms of data collection speed. In an effort to work in a more easily measured timeframe, we also tracked the diffusion of 1-methylimidazole in these MOFs. We hypothesized that the bulkier structure of this derivative compound compared to that of the parent imidazole would

slow its diffusion through the porous frameworks. Figures 6.6-6.9 depict the difference spectrum of the in-situ XANES results of 1-methylimidazole diffusion into suspensions of FeCl-PCN-224 and FeCl-PCN-222 MOF particles of two different sized ranges: nanosized particles with average diameter ~65nm and micron sized particle with average diameter~3μm (representative SEM images are shown in Figures 6.3-6.4). The spectral changes at the rising edge and white line region that indicate reaction completion occur on a faster timescale for the nano-sized particles than for the micron-sized particles of each framework, revealing the influence of the porous structure on the diffusion of this substrate into these MOF particles.

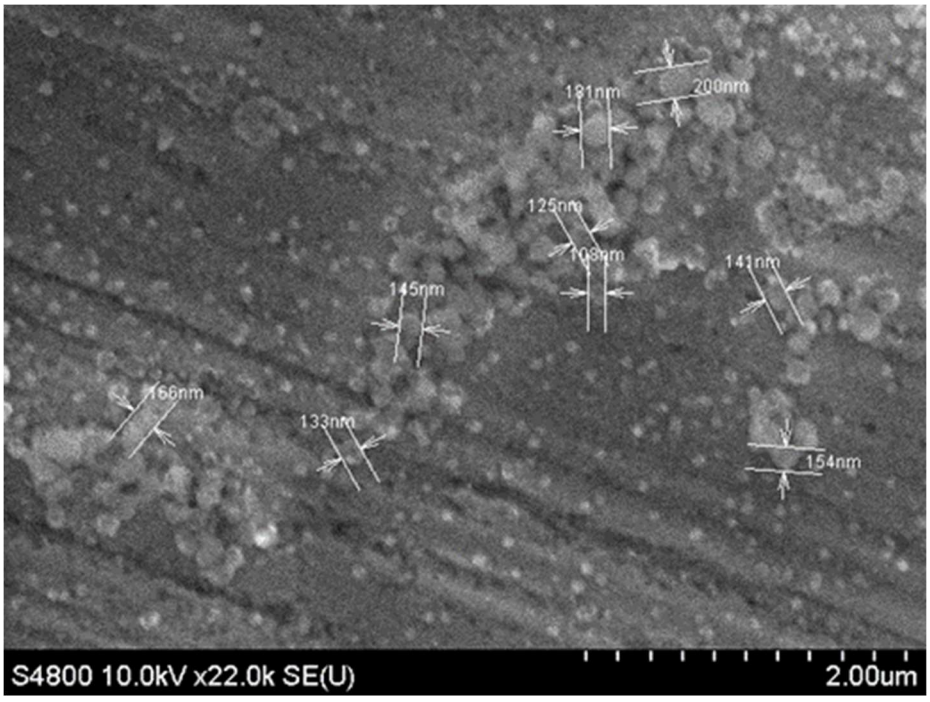

Figure 6.3 SEM image of nanoparticle FeCl-PCN-224 taken by Nicole-Irene Lahanas.

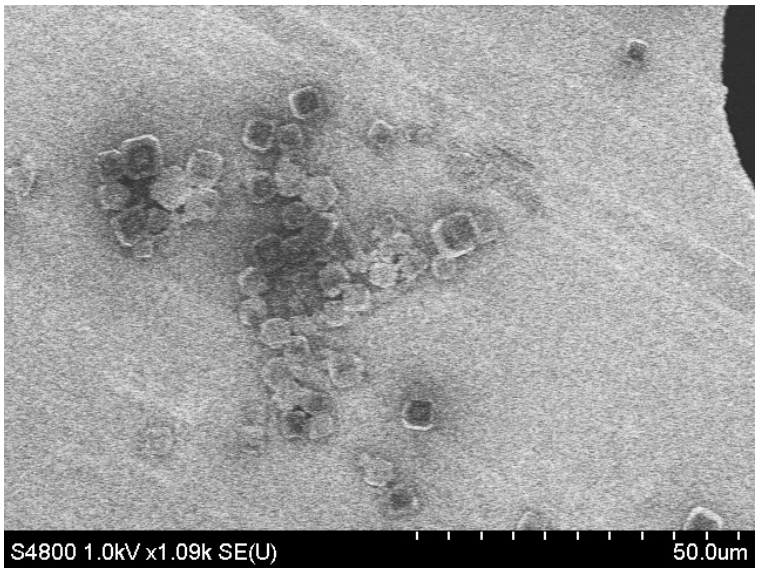

Figure 6.4 SEM image micron-sized particle FeCl-PCN-224 taken by Nicole-Irene Lahanas

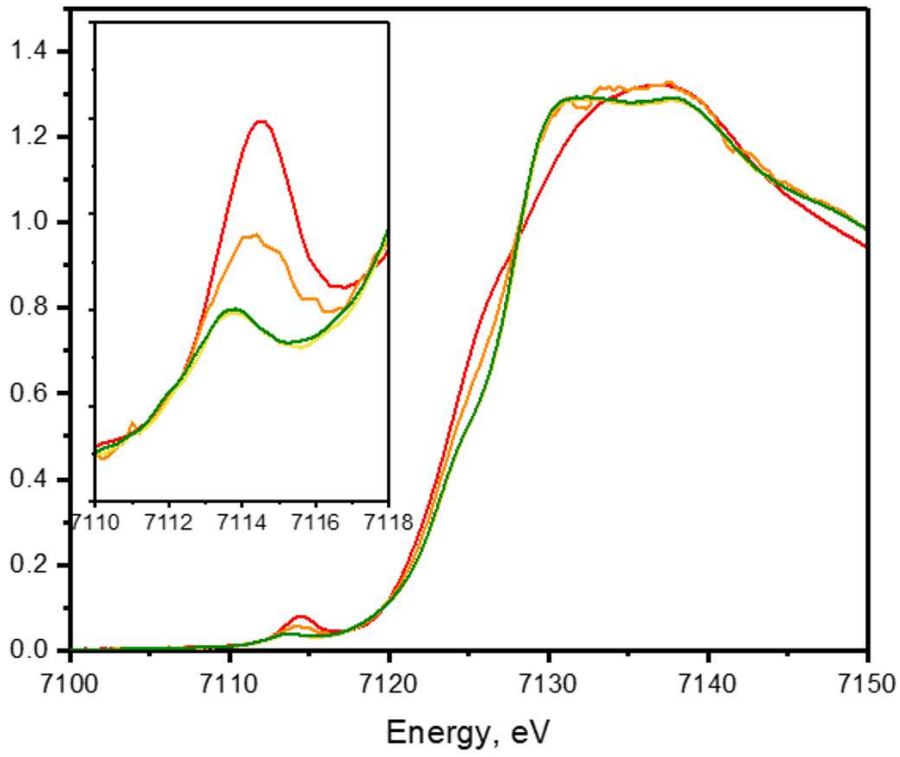

Figure 6.5 Imidazole diffusion into a suspension of FeCl-PCN-224 MOF of micron-sized particles. Red:FeCl-PCN-224 at T=0 (pre-injection of imidazole); orange: T=5s after imidazole injection; yellow: T=6-600s after imidazole injection; green: FeCl-PCN-224-Im control (T=final). T=time (seconds).

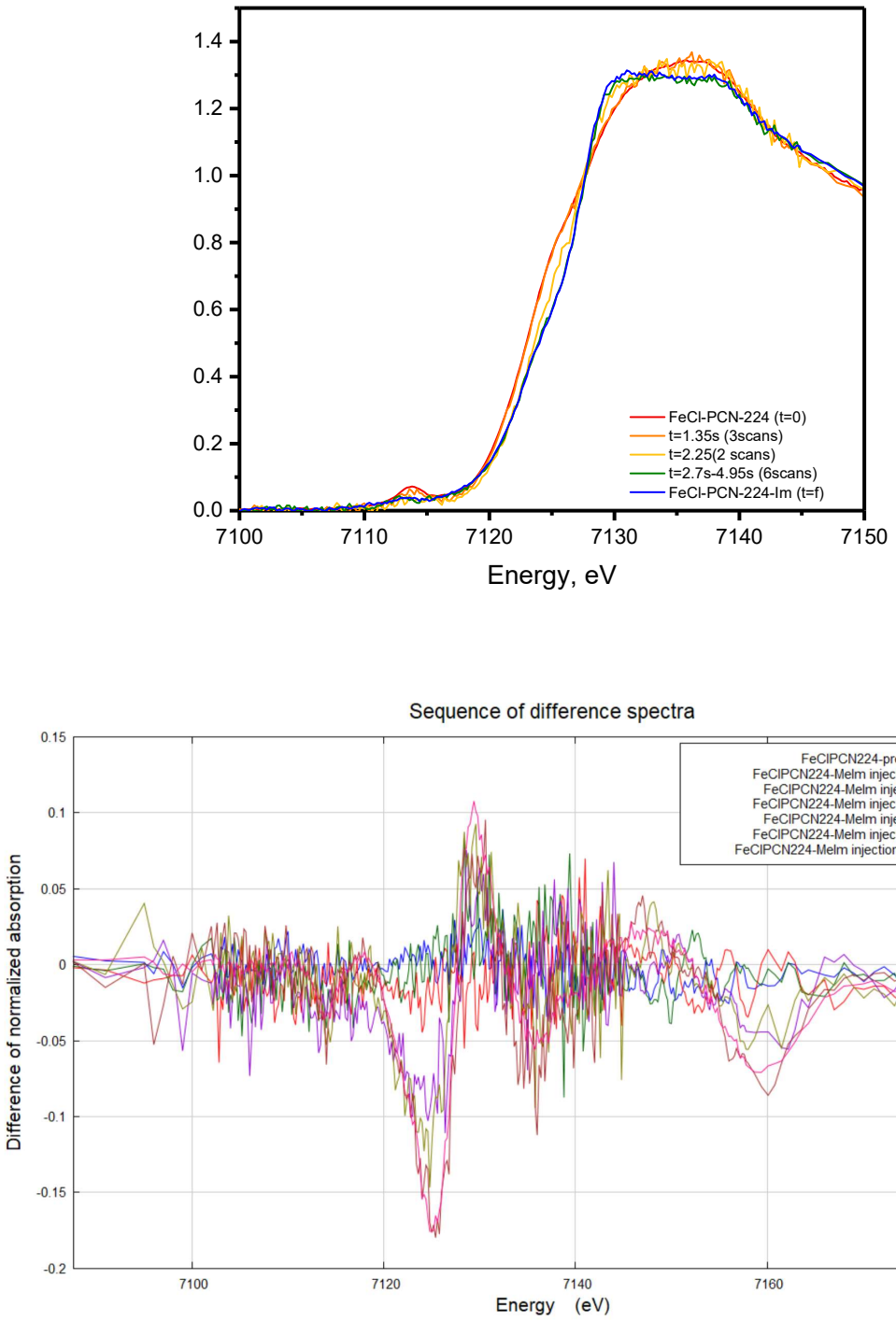

Figure 6.6 In-situ XANES (top) and difference spectrum (bottom) of FeClPCN-224-Im-FeCl-PCN-224 detailing the progression of 1-methylimidazole diffusion into a suspension of FeCl-PCN-224 MOF of nano-sized particles (~150nm).

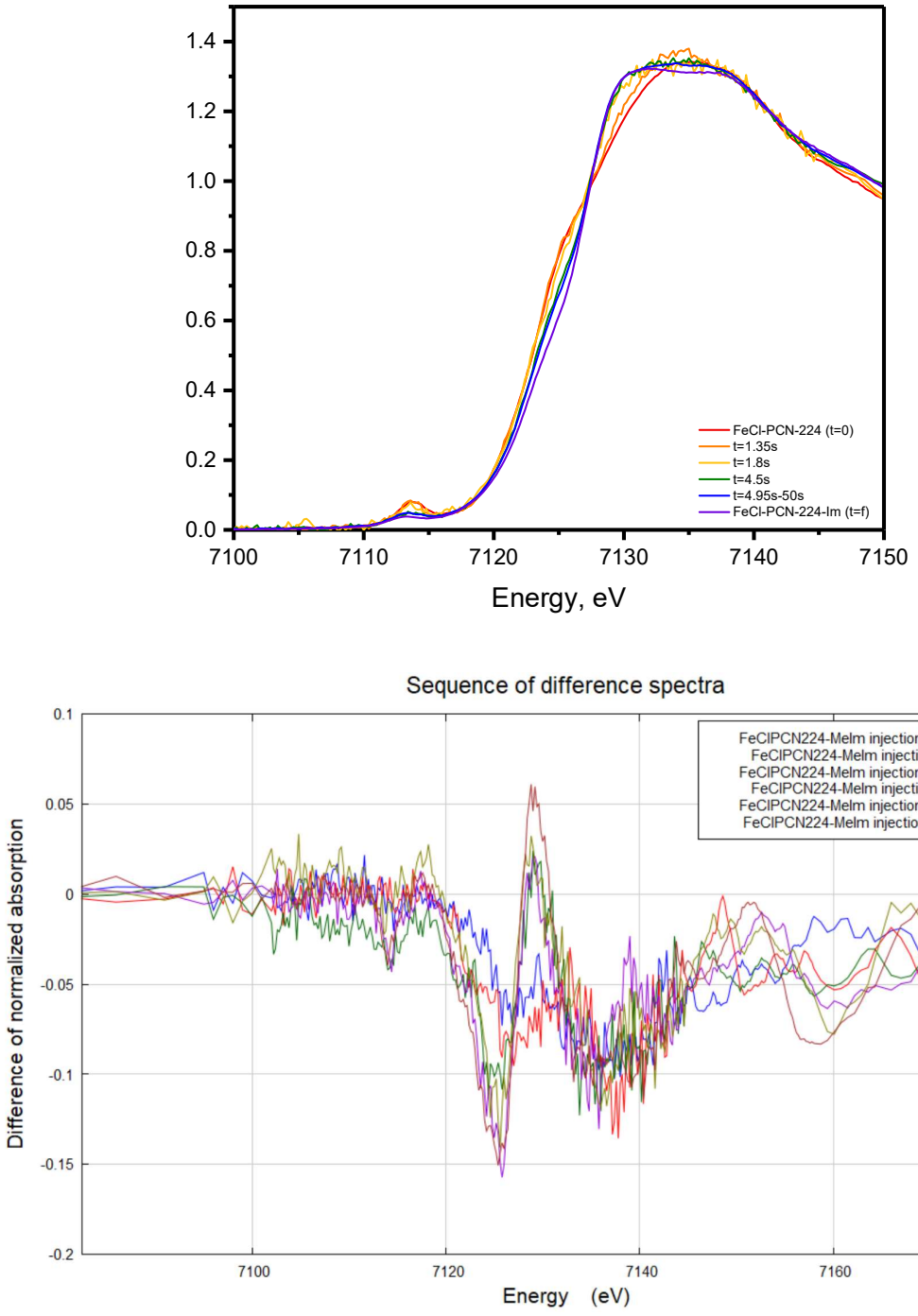

Figure 6.7 In-situ XANES (top) and difference spectrum (bottom) of FeClPCN-224-Im-FeCl-PCN-224 detailing the progression of 1-methylimidazole diffusion into a suspension of FeCl-PCN-224 MOF of micron-sized particles (~1-2μm).

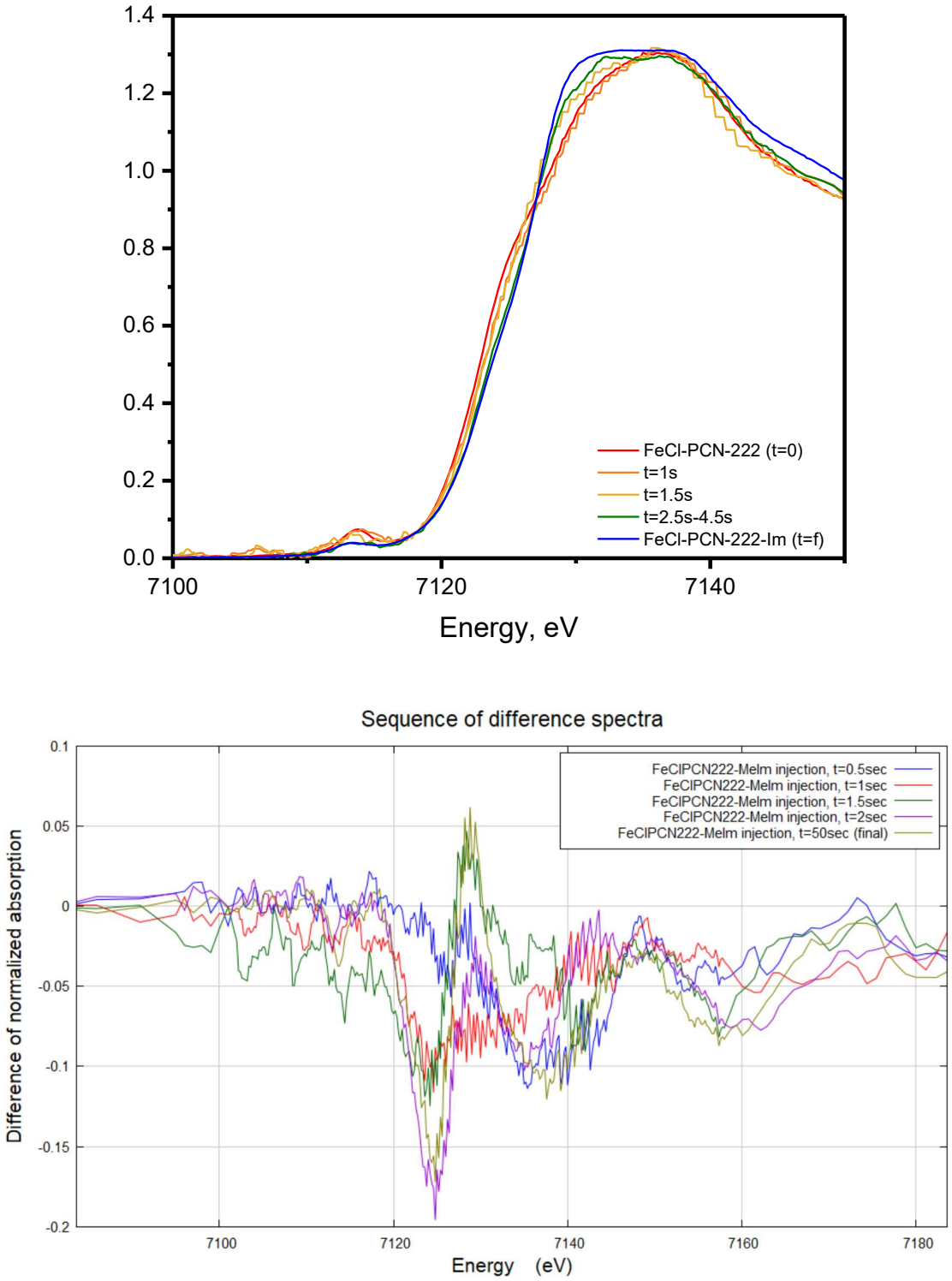

Figure 6.8 In-situ XANES (top) and difference spectrum (bottom) of FeClPCN-222-Im-FeCl-PCN-222 detailing the progression of 1-methylimidazole diffusion into a suspension of FeCl-PCN-222 MOF of nano-sized particles (~75nm).

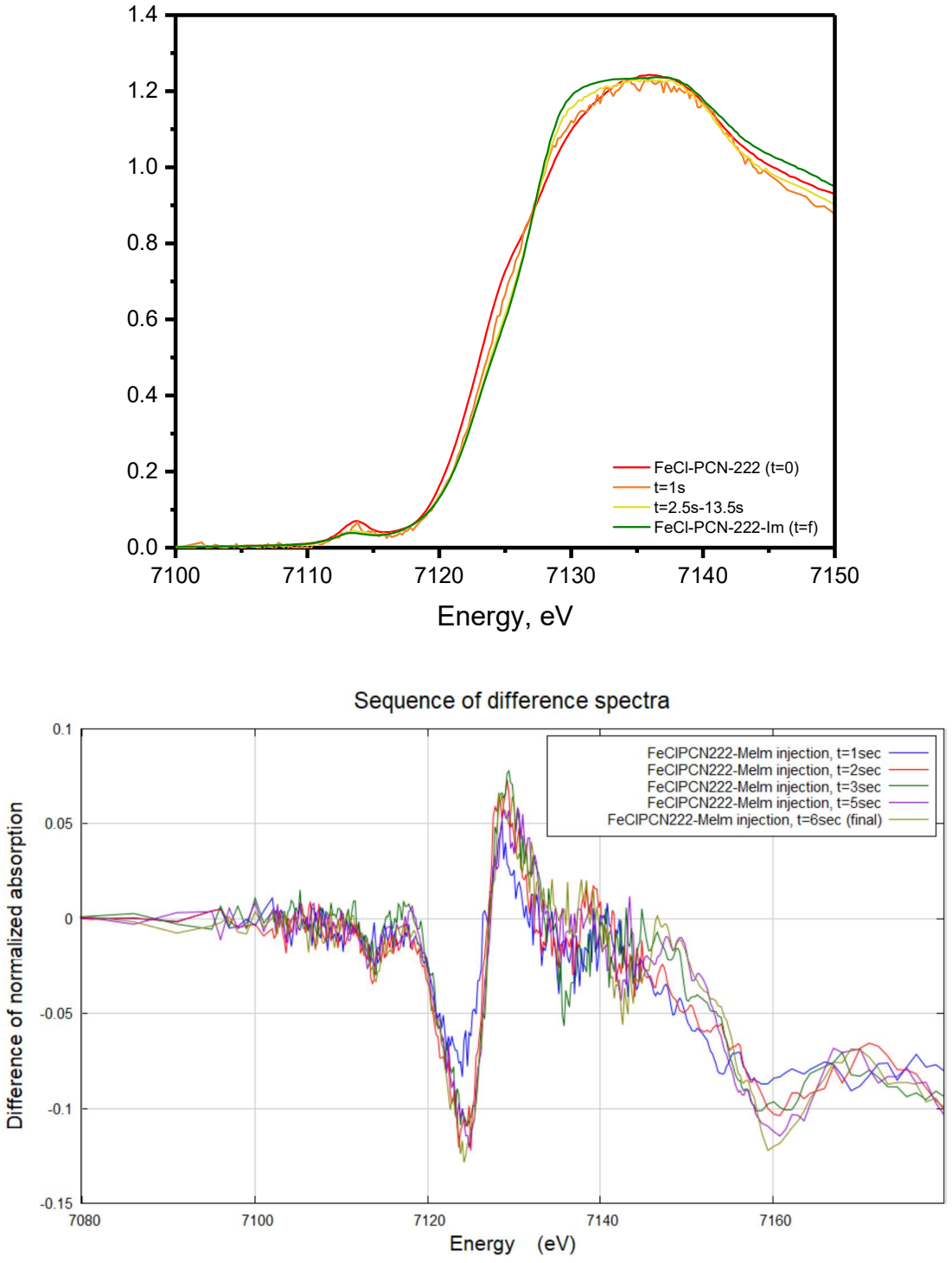

Figure 6.9 In-situ XANES (top) and difference spectrum of FeClPCN-222-Im-FeCl-PCN-222 detailing the progression of 1-methylimidazole diffusion into a suspension of FeCl-PCN-222 MOF of micron-sized particles (~1-2μm).

Single energy point time scans were also collected at 7125 eV (i.e. the energy at which the largest spectral change is expected) in an effort to gain more accurate kinetic information for these diffusion processes. However, without background subtraction and intensity normalization of the data, which require the collection of full spectra, the resulting kinetic traces could not be properly analyzed to yield meaningful rate information. Furthermore, while the largest observable change in the spectrum occurs at the expected edge position, other changes in the whiteline region were observed on a longer timescale, suggesting that the reaction kinetics are more complicated than we first thought. This white line spectral region is often difficult to evaluate, owing to the dual influences of both electronic effects and multiple scattering processes that are related to the local structure around the absorbing atom. Other changes in the pre-edge region where the intensity is already quite low, are within the experimental noise and therefore difficult to decipher.

The implications of this study at the stage of the project are two-fold. For one, given the current set up and beamline capacities, we were unable to extract out quantitative rate information on the diffusion processes in these MOF systems. Even with the bulkier substrate, diffusion into these two frameworks occurs with a surprisingly fast component that dominated the spectral response. A relatively slower reaction component, that appears to be associated with the larger particle size MOFs, yields additional spectral change that is nearly at the signal-to-noise limit of the detection scheme. Given the low iron-concentration in these MOF suspension samples, the signal is quite weak even in fluorescence mode, making the fast data collection needed for this experiment even more difficult. Improvements of the sample format that will allow better

time resolution and more efficient data collection will likely include designing a new sample cell with stop-flow capacities using microfluidics technology.

The other implication of this study is that given the fast diffusion kinetics observed qualitatively through these in situ XAS studies, catalytic reactions occurring at the subsurface metal sites within MOF materials like these may not be as hindered by diffusion as once thought. In other words, more than just the surface reaction sites of these frameworks are likely accessible for participation in a catalytic reaction.

6.3 Materials and Methods

6.3.1 Materials

Reference complexes, FeClTPP and FeTPPIm$_2$Cl (TPP = tetraphenylporphyrin, Im = imidazole), were prepared according to literature procedures,[14-17] as were the FeCl-PCN222[8] and FeCl-PCN224[13] MOFs, with some modifications. Solvent-exchange from DMF to Acetone to finally ethyl acetate was done over a period of a few weeks without isolation of the framework in between. Crystallinity of the MOF samples before and after treatment with imidazole and before and after X-ray exposure was confirmed by powder XRD.

6.3.2 Methods

Fe K-edge XAS were collected at the 8-ID ISS beamline of the NSLS-II using a Si(111) monochromator and fast-scanning damping wiggler . The XANES spectra were collected in fluorescence mode using a Passivated Implanted Planar Silicon (PIPS) detector. MOF

suspensions were made by suspending 50mg of MOF into 1.5mL of ethyl acetate. A liquid sample holder was designed and 3D-printed and held a total of 0.35mL of sample solution at a given time. A home-built computer-controlled syringe pump was utilized for controlled substrate injection from outside of the X-ray hutch. This was done by 3D printing the syringe pump base and components and feeding through a driving screw that was controlled through a stepper motor. XANES spectra were collected before and after injection of 0.15mL of substrate (saturated imidazole solution in ethyl acetate or 1-methylimidazole, neat).

6.4 References

[1] Li, J.-R.; Kuppler, R. J.; Zhou, H.-C., Selective gas adsorption and separation in metal-organic frameworks. *Chem. Soc. Rev.* **2009,** *38* (5), 1477-1504.

[2] Kreno, L. E.; Leong, K.; Farha, O. K.; Allendorf, M.; Van Duyne, R. P.; Hupp, J. T., *Chem. Rev. (Washington, DC, U. S.)* **2012,** *112* (2), 1105-1125.

[3] Dhakshinamoorthy, A.; Alvaro, M.; Hwang, Y. K.; Seo, Y.-K.; Corma, A.; Garcia, H., *Dalton Trans.* **2011,** *40* (40), 10719-10724.

[4] Han, S.; Hermans, T. M.; Fuller, P. E.; Wei, Y.; Grzybowski, B. A., *Angew. Chem., Int. Ed.* **2012,** *51* (11), 2662-2666, S2662/1-S2662/10.

[5] Krishna, R., *J. Phys. Chem. C* **2009,** *113* (46), 19756-19781.

[6] Krishna, R., *Chem. Soc. Rev.* **2012,** *41* (8), 3099-3118.

[7] An, H.; Li, M.; Gao, J.; Zhang, Z.; Ma, S.; Chen, Y., *Coord. Chem. Rev.* **2019,** *384*, 90-106.

[8] Feng, D.; Gu, Z.-Y.; Li, J.-R.; Jiang, H.-L.; Wei, Z.; Zhou, H.-C., *Angew. Chem. Int. Ed.* **2012,** *51*, 10307-10310.

[9] Heinke, L.; Gu, Z.; Woll, C., *Nature Comm.* **2014.** *5*, 4562.

[10] Westre, T. E.; Kennepohl, P.; DeWitt, J. G.; Hedman, B.; Hodgson, K. O.; Solomon, E. I. *J. Am. Chem. Soc*. **1997,** *119*, 6297−6314.

[11] Sheidt, W. R. *In The Porphyrin Handbook;* Kadish, K., Smith, K., Guilard, R., Eds.; Academic Press: New York, **2000**; *Vol. 3,* 49−112.

[12] Wilson, S. A.; Green, E.; Mathews, I. I.; Benfatto, M.; Hodgson, K. O.; Hedman, B.; Sarangi, R., *Proc. Natl. Acad. Sci. U. S. A.* **2013**, *110*, 16333−16338.

[13] Feng, D.; Gu, Z.-Y.; Chen, Y.-P.; Park, J.; Wei, Z.; Sun, Y.; Bosch, M.; Yuan, S.; Zhou, H.-C., *J. Am. Chem. Soc*. **2014**, *136*, 17714−17717.

[14] Radonovich, L. J.; Bloom, A.; Hoard, J. L. Stereochemistry of Low-Spin Iron Porphyrins. II. Bis(piperidine)-α,β,γ,δ-tetraphenylporphinatoiron(II). J. Am. Chem. Soc. 1972, 94, 2073−2078.

[15] Scheidt, W. R.; Osvath, S. R.; Lee, Y. J., *J. Am. Chem. Soc.* **1987**, *109*, 1958−1963.

[16] Li, N.; Petricek, V.; Coppens, P.; Landrum, J., *Acta Crystallogr., Sect. C: Cryst. Struct. Commun*. **1985**, *41,* 902−905.

[17] Collman, J. P.; Hoard, J. L.; Kim, N.; Lang, G.; Reed, C. A., *J. Am. Chem. Soc.* **1975,** *97*, 2676−2681.